Extraction of Alumina from South African calcined clays

MSc (50/50) RESEARCH REPORT

Prepared by

Matome Batsalelwang

536290

Submitted to

School of Chemical and Metallurgical Engineering, Faculty of Engineering and the Built Environment, University of the Witwatersrand, Johannesburg, South Africa

November 2024

Declaration

I declare that this dissertation is an original work of mine unless explicitly stated and cited otherwise. It is being submitted for a Master of Science in Engineering (Metallurgy and Material Sciences) degree in the School of Chemical and Metallurgical Engineering at the University of the Witwatersrand, Johannesburg. This dissertation has not been previously submitted for any degree or examination to any other academic institution.

Signature of candidate: ……BMatome……**Date: November 2024.**

ABSTRACT

The growing need for high-purity alumina (HPA) is driven by its critical importance in sophisticated batteries and electronic applications. Typically produced from high-purity aluminum (Al) metal using the alkoxide method, HPA production is closely linked to the Bayer process, which relies on Al metal derived from alumina (Al_2O_3) extracted from bauxite ores. However, the scarcity of alumina-rich bauxite reserves has prompted interest in alternative local sources of alumina including kaolinitic clays, which are abundant and widespread. Although the Bayer process is not appropriate for treating kaolinitic clays owing to their high silica content, efforts have been made to explore alkaline and acidic processing methods for alumina extraction. In particular, the HCl acid leaching process has been extensively studied as a viable acidic processing route.

South Africa possesses abundant kaolinitic clays despite the lack of bauxite reserves, making it necessary to investigate the potential for alumina extraction via HCl processing. This study investigated the dissolution of aluminum and iron species from thermally activated clay in a hydrochloric acid solution, emphasizing the selectivity of aluminum extraction over iron impurities. Furthermore, the effect of different calcination and acid leaching conditions on the dissolution of aluminum and impurity species in a hydrochloric acid solution was investigated. Three different kaolinitic clays sourced from South Africa, namely ball (BL), flint (FL), and fire (F) clays, were analyzed to ascertain their chemical and mineralogical properties. It was observed that the raw BL and FL clays utilized in this study shared similar mineralogical compositions, whereas the F clay contained additional clay minerals such as carbonates and smectite. However, mineralogical analysis revealed that BL and FL clays were predominantly rich in kaolinite (82.4% and 91.1%, respectively), whereas raw F clay exhibited a lower kaolinite content (16.5%) and a higher amount of quartz (44.7%).

The calcination of kaolinitic clay was performed at temperature range of 600 to 800 °C (interval of 50 °C) for a period of 8 hours. Infrared spectroscopy and X-ray diffraction were employed to confirm the structural and mineralogical changes,

revealing the transformation of kaolinite into amorphous metakaolinite. The research revealed that calcination temperature significantly influenced alumina extraction, with varying effects on iron content. The calcination temperatures necessary for the complete dehydroxylation of kaolinite into amorphous metakaolinite were uniform across all samples of raw BL, FL, and F clays at 600°C. At this temperature, BL clay demonstrated an Al extraction 79.4%, FL clay showed a recovery of 78.4%, and F clay exhibited an Al extraction of 36.7%. However, although the Al extraction from F clay increased with an increase in calcination temperature, it did not exceed 50 %. Conversely, an increase in the thermal decomposition temperature was accompanied by a decline in the amount of Al extracted from calcined BL clay. The incorporation of iron oxide species in calcined BL clay resulted in the formation of insoluble aluminum spinels at higher temperatures, particularly starting from 700°C until 800 °C. This process led to a decrease in the acid solubilities of both aluminum and iron.

Interestingly, the extraction of aluminum from calcined FL clay exhibited a fluctuating pattern: it decreased at 650°C and 750°C but increased at 700°C (69.5%) and 800°C (71.8%). Both calcined BL and FL clays at 600°C demonstrated high aluminum extraction, although accompanied by high iron content (67.8% and 66%, respectively), whereas calcined FL clay at 800°C offered high aluminum extraction with moderate iron content (40.2%). In comparison with BL clay, the lower amount of iron oxides in FL clay did not present a clear trend for the formation of spinels. Statistical analysis showed that leaching time had a significant impact on aluminum extraction of BL clay. Meanwhile, the acid concentration (pertaining only to FL clay), leaching temperature, solid/liquid ratio, and leaching time and solid/liquid ratio interaction significantly affected aluminum extraction for FL and F clays.

A higher iron content has ramifications in HPA production for subsequent processing of the leachate solution. However, the reduced energy requirement for achieving complete dehydroxylation, which is essential for aluminum dissolution, presents a significant advantage for aluminum recovery from both BL and FL clays. The choice between BL and FL clays would depend on either a lower energy requirement in the pre-treatment stage with the associated higher cost of processing leachate containing elevated iron content, or a higher energy demand in the

pretreatment phase with a lower cost linked to processing leachate with moderate iron content. Notably, for FL clay, there was flexibility in assessing the three calcination temperatures that yielded high aluminum dissolution. The findings of this study hold considerable importance for utilizing South African kaolinitic clays as a cost-effective, locally sourced alumina resource for HPA production.

ACKNOWLEDGEMENTS

I would like to express my gratitude to Prof. Sehliselo Ndlovu, the members of the Hydrometallurgy Research Group at the School of Chemical and Metallurgical Engineering, University of Witwatersrand, my colleagues at the Council for Scientific and Industrial Research (CSIR), and my family for their indispensable guidance and encouragement throughout this research project. Furthermore, I extend my sincere appreciation to CSIR for providing financial support to facilitate the realization of this study.

CONTENTS

LIST OF FIGURES

LIST OF TABLES

NOMENCLATURE

List of abbreviations and acronyms

Abbreviations and Acronyms	Full meaning
Al	Aluminum
Al^{3+}	Aluminum ion
Al_2O_3	Alumina
$AlCl_3$	Aluminum chloride
$AlCl_3.H_2O$	Aluminum chloride hydrate
$Al_2O_3.6H_2O$	Aluminum salt
$Al_2O_3.2SiO_2$	metakaolinite
$3Al_2O_3.2SiO_2$	Mullite
Al-OH	Aluminum-hydroxyl
Al $(OH)_3$	Aluminum hydroxide/ gibbsite
ɣ-AlO (OH)	boehmite
α-AlO (OH)	diaspore
Al-O	Aluminum – Oxygen
Al-O-Si	Aluminum – Oxygen – Silicon
ANOVA	Analysis of varience
AR	Analytical reagent
BL	Ball
C_2S	Calcium Silicate

Ca^{2+}	Calcium ion
$CaCO_3$	Calcite
CFA	Coal fly ash
CaO	Lime
$2CaO.SiO_2$	Dicalcium aluminate
$12CaO.7Al_2O_3$	Calcium aluminate compound
$CaO.Al_2O_3$	Calcium aluminate compound
$CaSO_4$	Calcium sulfate
Cl2	Chlorine gas
CSIR	Council for Scientific and Industrial Research
CV	Coefficient of variation
DTA	Differential thermal analysis
F	Fire
$Fe^{2+/}Fe^{3+}$	Iron ion
Fe_2O_3	Hematite/ iron oxide
$Fe(OH)_3$	Ferric oxide
FeOOH	Limonite
FL	Flint
FTIR	Fourier transformed infrared spectroscopy
H_2O	water
H^+	Hydrogen ion
H_2SO_4	Sulfuric acid

HCl	Hydrochloric acid
HPA	High Purity Alumina
HNO_3	Nitric acid
ICP-OES	Inductively coupled plasma atomic optical emission spectrometry
ICP-MS	Inductively coupled plasma atomic mass spectrometry
IV	Four / tetra
K^+	Potassium ion
K_2O	Potassium oxide
KOH	Potassium hydroxide
LED	Light-emitting diode
LiOH	Lithium hydroxide
LOI	Loss of ignition
Mg^{2+}	Magnesium ion
MgCO3	Magnesium carbonate
$MgCl_2$	Magnesium chloride
MgO	Magnesium oxide /Periclase
Na^+	Sodium ion
$Na_2O.Al_2O_3$	Sodium aluminate
Na_2SiO_3	Sodium silicate
Na_2CO_3	Sodium carbonate
NaOH	Sodium hydroxide
O_2	Oxygen

OH^-	Hydroxyl ion
R^2	Coefficient of determination
Si^{4+}	Silicon ion
SiO_2	Silica
Si-O	Silicon – Oxygen
Si-O-Al	Silicon – Oxygen - aluminum
Si-O-Si	Silicon – Oxygen – Silicon
Si-OH	Silicon-hydroxyl
$Si(OH)_4$ or H_4SiO_4	Orthosilicic acid groups
S/L	Solid/Liquid
Std.Dev	Standard deviation
Ti^{4+}	Titanium ion
TiO_2	Anatase / Titanium oxide
TGA	Thermal gravimetric analysis
V	Five / Penta
VI	Eight /Octa
Wt	Weight
XRD	X-ray diffraction
XRF	X-ray fluorescence

Units of measurement

Symbols	Meaning
Å	Ångstrom

°C	degree Celsius
°C min^{-1}	degree Celsius per minute
%	percentage
cm^{-1}	per centimetre
g	grams
g/ml	grams per millilitre
h	hour
M	Molarity
mg/l	milligrams per litre
ml	millilitre
rpm	revolutions per minute

Chapter 1 Introduction

1.1. Background

Alumina (Al_2O_3) has good chemical and physical properties and is widely used in abrasive, ceramic, refractory, cement, and chemical industries. Moreover, it is the only source of Al metal. There has been an increasing trend in the production of high-purity alumina (HPA), an alumina with a purity of 99.99% or higher (Pepper *et al.*, 2021). The high amount of alumina in HPA makes it a highly desirable product for various industries. HPA is an exceptional electrical insulator that is widely used as an insulating substrate for the deposition of printed circuits in lithium-ion battery appliances (Aly *et al.*, 2019). It is also a crucial component in the production of transparent light-emitting diode (LED) lenses and light appliances (Aly *et al.*, 2019). The Bayer process is the most widely utilized alkaline method for producing metallurgical-grade alumina from bauxite ore. This process recovers aluminum from bauxite through caustic digestion and subsequently crystallizes aluminum hydroxide from a solution of sodium aluminate (Pepper *et al.*, 2021). However, this process generates large quantities of solid waste desilication products called red mud.

Refining bauxite ores containing more than 7% active silica (SiO_2) is challenging (Donaldson and Raahauge, 2008). High temperatures and pressures are necessary for the Bayer process; however, high temperatures increase the reactivity of the silica (Pehlivan *et al.*, 2012). The sodium hydroxide (NaOH) reaction with dissolved aluminum results in immediate precipitation of dissolved silica, which is unstable and causes a significant loss of aluminum to the red mud (Kaußen and Friedrich, 2016). The production of aluminum depends on the availability of inexpensive, smelter-grade alumina with high purity, and the mineralogy of bauxite plays a vital role in ensuring successful operation of the Bayer process for alumina production (Authier-Martin *et al.*, 2001). The Bayer process involves producing

smelter-grade alumina with 99.5% purity from bauxite that contains between 30% and 60% Al_2O_3 (Authier-Martin *et al.*, 2001). The alkoxide method, which employs high-purity aluminum metal to produce alumina, is a commonly used commercial process for producing HPA. This method is inherently connected to the Bayer process because it requires aluminium (Al) as the starting material. Consequently, the high-quality bauxite reserves that are depleting and the expenses connected to processing lower-quality ores may impact the expenses associated with conventional HPA production (Pepper *et al.*, 2021).

Alumina-rich bauxites are limited to certain countries, which has led to the need to identify alternative materials as sources of alumina. Clays, encompassing diverse mineral compositions and geological formations, offer a promising avenue for sustainable alumina production, potentially diversifying the alumina supply chain and reducing reliance on traditional bauxite reserves. Owing to the high alumina content of certain kaolinitic clays and their abundance in many locations, kaolinitic clays are increasingly considered as alternative sources of alumina. The main mineral phase in kaolinitic clays is kaolinite.

Kaolinite is characterized by its 1:1 dioctahedral structure, featuring octahedral coordination of Al^{3+} and Si^{4+} tetrahedral coordination (Nnanwube and Onukwuli, 2023) . The sheets of the mineral are interconnected by feeble van der Waals forces between the hydroxyl groups of the octahedral sheets and the basal oxygens of the tetrahedral sheets (Barton and Karanthanasis, 2005). The layers of the mineral are firmly bound by hydrogen bonding, constraining expansion and confining the reactive area to the external surfaces (Barton and Karanthanasis, 2005). The theoretical composition of kaolinite in its pure form includes13.96% structural water (H_2O), 39.50% Al_2O_3, and 46.54% SiO_2 (Udochukwu *et al.*, 2019). Processing it through the Bayer process is not an option because of the high silica content of kaolinitic clays. South Africa, known for its abundant mineral wealth and diverse geological formations, hosts a clay repository that presents compelling prospects for exploring novel extraction techniques within the region. Therefore, there is a need to investigate alternative approaches for extracting aluminum from these clays.

Kaolinitic clays often contain impurities such as free quartz, mica, anatase, and iron oxides (hematite and magnetite) (Chang, 2016). Moreover, the structure of silicate minerals affects their stability and ease of decomposition (Perkins, 1964). In the dissolution process, the covalent bonds between silicon and oxygen, as well as between aluminum and oxygen, are broken (Crundwell, 2014). Alumina readily dissolves above ambient temperature in strong acids such as hydrochloric acid (HCl), sulfuric acid (H_2SO_4), and nitric acid (HNO_3), as well as in strong bases such as potassium hydroxide (KOH) and sodium hydroxide (NaOH) (Aly *et al.*, 2019). In acidic solutions, H^+ ions react with the silicate groups on the surface, while iron is also dissolved (Crundwell, 2014). In contrast, in alkaline solutions, metal atoms react with OH^- ions on the surface (Crundwell, 2014).

To obtain aluminum, a pretreatment method is necessary because kaolinite is acid-insoluble (Johnston *et al.*, 2022a). Calcination is used as a pretreatment method for the dehydroxylation of kaolinite. This process entails the removal of hydroxyl ions present in kaolinite and transformation into an amorphous aluminosilicate phase ($Al_2O_3.2SiO_2$) with active Si-O and Al-O bonds, called metakaolinite, thereby destroying its crystalline structure. The transformation into the amorphous metakaolinite phase is crucial because it improves the reactivity of the clay and makes the aluminum in the clay accessible in acidic environments. The temperature at which dehydroxylation occurs during calcination depends on factors such as crystallinity, impurity content, particle size, heating rate, heating duration, and temperature (Udochukwu *et al.*, 2019). Furthermore, the solubility of clay in an acid depends on factors such as acid nature, the acid-to-clay ratio, leaching duration, and leaching temperature (Okon *et al.*, 2019).

The most noteworthy method for producing alumina is HCl leaching (Donaldson and Raahauge, 2008). The advantages of HCl acid leaching technology include low silica solubility in HCl acid solutions (Tantawy and Alomari, 2019) and the use of the HCl acid sparging crystallization process of aluminum salt ($AlCl_3.6H_2O$), which separates the aluminum salt from iron impurities, resulting in good purification and

recovery of the leaching reagents (Donaldson and Raahauge, 2008). HCl leaching technology is feasible but lacks comprehensive commercial application. Simultaneous dissolution of metals such as iron (Fe), magnesium (Mg), potassium (K), sodium (Na), and titanium (Ti) is one of the primary disadvantages of the leaching (Sibanda *et al.*, 2016).

The differences in the chemical composition, crystallinity, mineralogy, and purity of clays at various locations indicate the need to investigate the structural phase changes of kaolinitic clay and the dissolution of calcined kaolinitic clay during the leaching of alumina using hydrochloric acid solutions. This research project focuses on the feasibility of alumina extraction from South African clays via the hydrochloric acid route. The influence of calcination temperature and time, on obtaining amorphous metakaolinite, its dissolution in HCl leaching, and the effect of HCl leaching conditions on the dissolution of aluminum from kaolinitic clay were investigated.

1.2. Problem statement

The global demand for alumina across various applications is steadily increasing. Despite this, alternative processes developed to produce Al_2O_3 from non-bauxite materials have not achieved the commercial success of the Bayer process (Habashi, 2017). Hydrometallurgical processes such as leaching for extracting Al_2O_3 from non-bauxite sources are often preferred because of their lower costs, driven by reagent regeneration, reduced energy consumption, eco-friendly process requirements, and the ability to process low-grade ores (Barry *et al.*, 2019). Hydrochloric acid leaching, though requiring expensive corrosion-resistant equipment, is efficient, faster, and offers reagent regeneration, which can offset costs. Since the mineral composition of non-bauxite materials such as clays varies by location, it is essential to assess the feasibility of using hydrochloric acid processing to extract Al_2O_3 from South African calcined clays as a step towards localizing the technology. Additionally, the dissolution of aluminum and impurities including iron, magnesium, calcium, potassium, titanium, and silicon species must be examined, as these impurities will affect the purity of the final product.

1.3. Aim and objectives of the study

The aim of the research study is to investigate the dissolution of aluminum and impurity species from thermally activated clay in hydrochloric acid solutions, with a specific focus on assessing the selectivity of aluminum extraction relative to iron impurities. Furthermore, the effects of different calcination and acid leaching conditions on the dissolution of aluminum and impurity species in a hydrochloric acid solution will be investigated.

The aim of this research will be met through the following research objectives:

a) Determination of calcination temperatures and times required to produce amorphous metakaolinite phase from ball (BL) clay, flint (FL) clay, and fire (F) clay.
b) Investigating the effect of calcination temperature on the extraction of aluminium, and impurities such as iron, titanium, and silicon dissolution in hydrochloric acid solutions.
c) Investigating the effect of leaching parameters such as acid concentration, solid/ liquid ratio, leaching temperature and time on aluminium dissolution in hydrochloric acid solutions.

1.4. Research questions

The following research questions were explored in this study:

a) What are the changes in the chemical structure of the clay that occur with changes in calcination temperature?
b) How do changes in the chemical structure of clay, induced by changes in calcination temperature, influence the metal extraction process?
c) How selectivity is the acid-leaching process for Al over Fe extraction?

1.5. Hypothesis

Calcination temperatures between 600-800°C enhance alumina extraction efficiency by promoting mineral decomposition and transformation, leading to increased alumina availability through the conversion of kaolinite into amorphous metakaolinite phases. However, higher iron concentrations may hinder alumina recovery because of the formation of insoluble metakaolinite compounds at elevated calcination temperatures.

1.6. Dissertation layout

This dissertation comprises six chapters. In the opening chapter, the research background is detailed, and the research problem, questions, aims, objectives, and hypotheses are presented. The second chapter offers an extensive review of alumina, covering its sources, production processes, and challenges associated with both. The third chapter details the experimental methodology, characterization techniques, and apparatus employed in the acid leaching and calcination experiments as well as the experimental design for optimizing the leaching parameters. Chapter four and five focus on clay characterization and mineralogy and present the experimental and optimized results of the leaching parameters, as well as the impact of calcination conditions on Al recovery. Finally, the sixth chapter summarizes the overall study findings and provides future research recommendations.

Chapter 2 Literature Review

2.1. Introduction

Aluminum oxide, known as alumina, has a range of thermodynamically stable phases including alpha, delta, gamma, kappa, and theta phases (Kaunisto *et al.*, 2023). These transitional phases are influenced by the type of precursor used and the processing methods employed to produce alumina. Alumina is economically viable across all phases because of its versatile technological applications in a diverse array of fields including high-quality insulators, semiconductors, and microelectronics for electrical, electronic, and computer engineering (Salahudeen *et al.*, 2015). Alumina is also used to produce high-strength materials in the construction industry, and different ceramics, alloys, and refractories in the materials and metallurgy industries (Salahudeen *et al.*, 2015). In addition, alumina remains a crucial support for zeolite catalysts used in the processing of natural gas, petrochemicals, and petroleum (Takbiri *et al.*, 2013). Other industrial applications of alumina include its use as a fire retardant in the manufacturing of plastics, high-grade polishes, and sapphire crystal growth (Salahudeen *et al.*, 2015).

The traditional Bayer process has been used for over a century to produce alumina from bauxite ore. This process entails the digestion of bauxite, which contains alumina, in a caustic medium under high pressure and temperature. Once the process is complete, the filtered liquor is cooled, resulting aluminum hydroxide ($Al(OH)_3$) precipitation (Lee *et al.*, 2009). The precipitated aluminum hydroxide is then calcined to produce alumina. Subsequently, the Hall-Heroult process is employed to transform alumina into aluminum. However, the conventional Bayer process generates hazardous red mud waste that pollutes the environment (Sellaeg *et al.*, 2017). In addition, the bauxite reserves are limited and contain low amounts of alumina (Barry *et al.*, 2019). Consequently, countries with limited bauxite resources have sought to decrease their reliance on imports by finding alternative

local sources of alumina and aluminum (Barry *et al.*, 2019). An alternative approach involves extraction of alumina from raw non-bauxite materials. Clay has been considered a potential alternative to bauxite, and alkaline and acidic processing routes have been investigated to determine the feasibility of extracting alumina from these resources (Barry *et al.*, 2019).

South Africa neither mines bauxite nor refines it to produce alumina. The country's smelter uses alumina imported from Australia to produce primary aluminum (Department of Science and Technology and Council for Scientific and Industrial Research, 2017). Nonetheless, according to the study by Ekosse (2010), South Africa has 20 deposits of kaolin spread across South Africa. The deposits are found in areas such as Hammanskral in Gauteng Province, Zebediela in Limpopo Province, Makana in Eastern Cape, Bronkhorstspruit in Mpumalanga, Ndwendwe in Kwazulu Natal, Northern Cape, and Western Cape (Diko, 2015; Heckroodt, 1991). The applicability of kaolinitic clays for alumina extraction depends on their chemical, physical, structural, and surface properties (Makó *et al.*, 2001).

This literature review intends to provide an in-depth review of the various sources and processing methods for alumina, highlighting the importance of the pretreatment of kaolinitic clays and the benefits of the hydrochloric acid leaching route for these clays based on their chemical characteristics.

2.1.1 Aluminum oxide

Aluminum oxide is a compound composed of aluminum and oxygen. It is a white odorless crystalline powder. It occurs naturally in its crystalline polymorphic α–Al_2O_3 phase, known as corundum (Al-Zahrani and Abdul-Majid, 2009; Orugba *et al.*, 2020). Different types of corundum form precious gemstones, rubies, and sapphire, which are crystalline oxide variants (Al-Zahrani and Abdul-Majid, 2009). Bauxite is considered the principal aluminum ore. Aluminum oxide is a material that stands out due to its exceptional chemical, mechanical, and thermal properties, making it a preferred choice over many comparable materials (Matmatch, 2019). This provides improved solutions for cost-effective production. The Al_2O_3 is used as an electrical insulator, and it displays comparably high thermal conductivity

among ceramic materials (Gopinath, 2016). In addition, it is insoluble in water and exhibits a high level of hardness. As a result, it is often employed in the production of cutting tools and as an abrasive (Gopinath, 2016). Aluminum oxide is an amphoteric compound that shows reactivity with both acids and bases. It behaves as an acid when reacting with a base, neutralizing the acid and producing a salt. Similarly, it behaves as a base when reacting with an acid, neutralizing the base and producing a salt.

The properties of aluminium oxide include a boiling point of 2977°C, a melting point of 2072 °C, a hardness of 15-19 GPa, an electrical resistivity of 10^{12}-10^{13} Ωm, a mechanical strength of 300 – 630 MPa, a compressive strength of 2000 – 4000 MPa, a thermal conductivity of 20 – 30 W/mK, a density of 3.95 g/cm^3, a molecular mass of 101.96 g/mol, and a solid appearance (Abyzov, 2019; Matmatch, 2019; Haekal and Mubarok, 2021). Aluminum oxide is primarily utilized as a feedstock in the production of aluminum, and it also possesses a multitude of industrial applications in fields such as medicine, military, protective equipment, electrical and electronics, and gem industries (Wundermold, 2014).

2.2. Alumina sources and mineralogy

Understanding the sources of alumina and its mineralogy is crucial for alumina extraction, processing, and application. This section provides an overview of the different sources of alumina and their mineralogy, highlighting the properties and characteristics that influence its usefulness and value.

2.2.1 Bauxite

Bauxite is the main source of aluminum in the manufacturing process using the Bayer method. Typically, bauxite contains 56-59% alumina, 20-28% iron oxide, 3-8% silica, 0.5-3% titanium dioxide and 10-15% water (Donaldson and Raahauge, 2008). Bauxites are residual rocks that consist mainly of alumina hydrate minerals including alumina trihydrate, boehmite (ɣ-AlO(OH)), diaspore (α-AlO(OH)), which exist in the majority, and gibbsite ($Al(OH)_3$) (Kaußen and Friedrich, 2016 ;

Liu *et al.*, 2011). Other minerals such as quartz, halloysite, magnetite, geothite, anatase, kaolinite, hematite, and some phosphatic and manganiferous minerals may also be present in smaller amounts in bauxite (Donaldson and Raahauge, 2008). Traces of elements, such as carbon, molybdenum, tin, beryllium, cesium, tantalum, thorium, vanadium, cobalt, copper, lanthanum, zinc, strontium, boron, calcium, gold, nickel, lead, magnesium, gallium, hafnium, uranium, yttrium, zirconium, cerium, columbium, barium, sulfur, and chromium, have been detected in bauxite ores (Donaldson and Raahauge, 2008). The primary source of alumina hydrates and hydrous aluminum silicates in bauxites is the weathering of metamorphic, igneous, and volcanic rocks that contain felspars and felspathoids, as well as micas, aluminum silicates, and clay minerals found in sedimentary rocks (Donaldson and Raahauge, 2008).

Typically, two primary types of bauxites are found in tropical and subtropical regions: lateritic and karstic. These types of bauxites are characteristically found in areas with hot and humid climates (Donaldson and Raahauge, 2008; Van et al., 2012). The primary geological difference between karstic and lateritic bauxites lies in the type of rock with which they are associated. Karstic bauxites are found in association with limestone, whereas lateritic bauxites are found in other geological formations (Donaldson and Raahauge, 2008). The differences between these two include the iron content, porosity, structure of the ore, and particle size distribution (Donaldson and Raahauge, 2008). The color of bauxite ranges from white to black and includes various shades of brown, gray, green, pink, red, and yellow. This color variation is influenced by the quantity, hydration state, and the size of the iron mineral particles present in bauxite (Donaldson and Raahauge, 2008). Variations in iron content dictate the specifications for impurity separation circuits within the Bayer plant (Donaldson and Raahauge, 2008). The type and amount of minerals contained in aluminum ore, specifically boehmite, diaspore, and gibbsite, are key determinants of the necessary alumina/NaOH ratio, NaOH concentration, and digestion temperature (Donaldson and Raahauge, 2008).

The countries with the largest bauxite reserves include Guinea, Vietnam, Australia, Brazil, China, Jamaica, India, Indonesia, Russia, Kazakhstan, and Saudi Arabia (Statista, 2024). Guinea has the largest reserves of bauxite amounted to 7.4 billion

metric dry tons as of 2023. According to the latest available data, Australia is the leading bauxite producer globally in 2023, producing approximately 98 million metric tons (Statista, 2024).

2.2.2. Alternative sources

Although most of the alumina around the world is produced from bauxite ore through the Bayer process, alternative sources of alumina can be used to supplement or replace bauxite-derived alumina.

2.2.2.1. Anorthosite

Anorthosite is an igneous rock that is rich in aluminum and calcium. It has been discovered in substantial quantities in various regions across the world, such as Scandinavia, Canada, and Greenland (Donaldson and Raahauge, 2008). Anorthosite can be processed to produce high-purity alumina, suitable for a range of applications including electronic ceramics, catalysts, and abrasives (Fujiwara *et al.*, 2007).

2.2.2.2. Fly ash

Coal fly ash (CFA) is a by-product of coal combustion and is produced in significant amounts by coal-fired power plants (Ghazali *et al.*, 2019; Li *et al.*, 2020). Furthermore, CFA compositions with alumina and silica being the primary components, differ based on the type of coal burned and combustion conditions. The CFA can undergo processing to extract its alumina content, which can be employed in various applications, including the manufacture of construction materials and ceramics (Ghazali *et al.*, 2019).

2.2.2.3. Aluminum recycling

The scrap and waste aluminum can be recycled to produce high-purity alumina. The recycling process involves smelting scrap or waste to recover aluminum metal,

which is then converted into alumina by a series of chemical and thermal treatments.(Capuzzi and Timelli, 2018).

2.2.2.4. Kaolin

Clay minerals are mainly composed of aluminosilicate minerals, with only small amounts of iron and alkali metal oxides present.(ElDeeb *et al.*, 2019; Bagherzadeh *et al.*, 2023). Kaolin, with its high alumina content (20-26%), is an attractive candidate for alumina production (ElDeeb *et al.*, 2019). Kaolin is mainly composed of kaolinite, which is a type of aluminosilicate clay composed of tetrahedral alumina and octahedral silica molecules connected by an apical oxygen atom (Johnston *et al.*, 2022a). The aluminate and silicate layers are held together through strong ion-covalent bonds, which are connected by weak hydrogen bonds (Sperinck *et al.*, 2011).The main impurities in kaolin are mica (10 -45%), quartz, and iron oxide, account for 1-10% of the mixture (Olaremu, 2015; ElDeeb *et al.*, 2019). Kaolin is composed of 39.47% Al_2O_3 and 46.55% SiO_2 based on its molecular weight (Cao *et al.*, 2022).

The structure of kaolinite (Figure 2.1) is primarily composed of an Al(O.OH) octahedral sheet and a Si-O tetrahedral sheet, which makes it highly stable and resistant to acid and alkali reactions under normal conditions (Xue *et al.*, 2023). This demonstrates chemical inertness across a broad pH spectrum. The layer of alumina comprised four hydroxyl (OH) groups. Among these, three OH groups are referred to as inner surface OH groups and the remaining OH group is the inner OH group (Johnston *et al.*, 2022a). In addition, the inner surface OH groups are situated on the surface of the kaolinite crystal lattice, whereas the inner OH groups face the inside of the crystal lattice (Johnston *et al.*, 2022a). Furthermore, the inner surface OH groups are positioned within an external unshared plane and are symmetrically independent (Johnston *et al.*, 2022a).

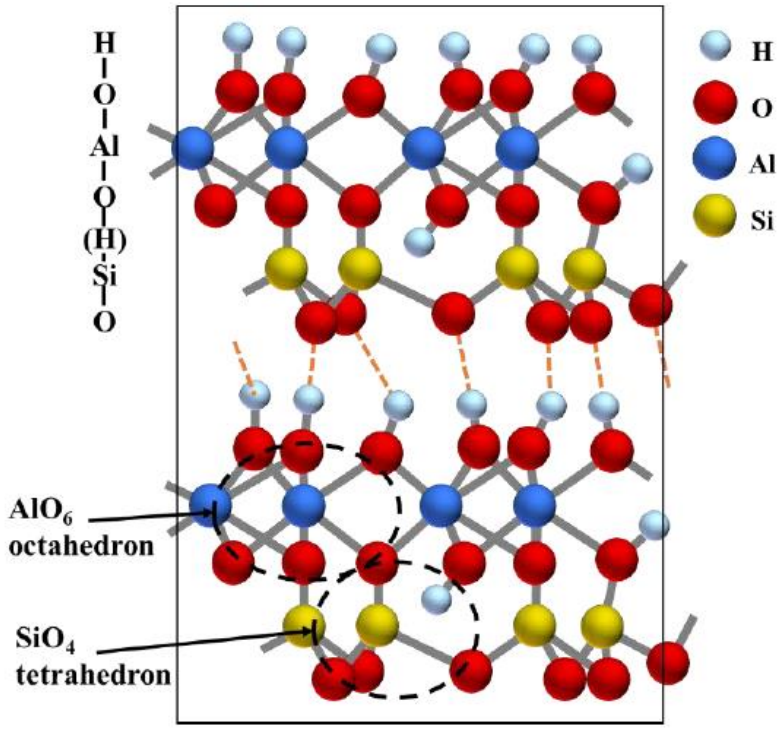

Figure 2.1: Structural layer of kaolinite (Xue et al., 2023)

2.3. Pretreatment Techniques

Pretreatment techniques perform a crucial role in alumina extraction processes using clays. According to Wagh and Pande (2014), the primary objective of pretreatment is to modify the properties of clays, such as their mineralogy, chemistry, and morphology, to enhance their extractability. Pretreatment techniques are specifically designed to enhance the efficiency of alumina extraction through increasing clay reactivity and minimizing impurities that could disrupt the extraction process (Li *et al.*, 2020).

The pretreatment of clays is necessary to improve their dissolution characteristics in acidic or basic solutions (Erdemoğlu *et al.*, 2018). These pretreatment steps typically involve a series of chemical reactions or physical processes to remove impurities and transform the raw material into a form suitable for further processing (Bagani *et al.*, 2021). The most commonly adopted pretreatment methods for kaolin include thermal activation, surface impregnation, mechanical activation, chemical activation, and thermochemical activation (Bagani *et al.*, 2021).

2.3.1. Mechanical activation

Different types of mills, such as planetary ball, vertical, and cryogenic mills, are used for mechanical activation. Intensive milling using high-energy mills achieves mechanical activation, which increases the reactivity of raw materials. This process also promotes the destruction of crystallinity (amorphization) and the formation of active surfaces. These active surfaces may be crucial in subsequent processes, including leaching (Erdemoğlu *et al.*, 2018). Leaching kinetics are enhanced for both sulfide and oxide minerals by increasing the strain, surface area, structural disorder, amorphization of crystals, microtopography, and the emergence of new phases that are more amenable to leaching and thermal reduction (Barry *et al.*, 2019; Alyosif *et al.*, 2023; Pourghahramani *et al.*, 2008).

A typical grinding process usually starts with a decrease in particle size, leading to the deformation of mineral crystal structures and disruption of the bonds between Al-OH, Si-OH, Si-O, and Al-O-Si (Novikova and Belchinskaya, 2016; Erdemoğlu *et al.*, 2018). The clay mineral properties (physical and colloidal) are influenced by the milling conditions. It has been observed that during the first grinding stage, there is a particle size reduction and clay surface area increase, as well as changes in porosity (Novikova and Belchinskaya, 2016). As the grinding process continues, the particles start to adhere together, which leads to the loss of crystalline structure, a decrease in the specific surface area, and changes in clay dispersion and plasticity characteristics (Khalifa *et al.*, 2020).

2.3.2. Mechanochemical activation

Mechanochemical treatment involves milling in specific chemical media such as acid, alkaline, and water solutions (Novikova and Belchinskaya, 2016). This can lead to severe structural changes and alterations in the mineral properties. This method is commonly used to improve catalytic properties and acid dissolution of minerals. By mechanically exposing mineral particles, new active sites are created at their boundaries, thereby increasing the cation exchange capacity of the mineral (Souri *et al.*, 2015).

2.3.2. Thermal activation (Calcination)

The common pretreatment method for producing alumina involves the calcination of non-bauxite ores, namely aluminosilicate clays, prior to the acid leaching step. During calcination, the structure of the non-bauxite minerals is altered, leading to the formation of disrupted metastable phases (Figure 2.2) (Barry *et al.*, 2019). The transformation of the crystal water within the structure occurs successively from liquid phase to vapor phase (Barry *et al.*, 2019). Different mechanisms can occur separately or concurrently, such as cation oxidation, water loss, resulting in dehydroxylation, cation migration to different sites, and structural disintegration (Birincia *et al.*, 2017). Consequently, the amorphous non-bauxite mineral structure exhibits a high reactive potential when exposed to a solution containing alkali or alkaline earth metals and mineral acid.

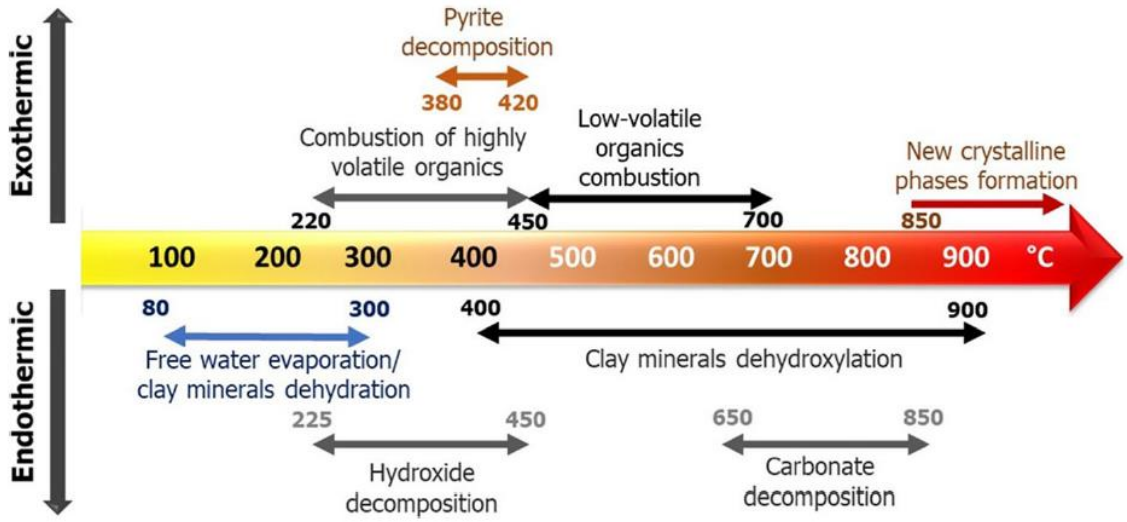

Figure 2.2: Reactions during calcination (Hanein *et al.*, 2022)

Calcination of clay minerals involves heating natural clay samples at an increased temperature, resulting in the release of water molecules and adsorbed gas and the emergence of a more open surface. Nevertheless, as the temperature increases and varies for each type of mineral, the crystal structure may suffer partial damage or even complete collapse, leading to a decline in surface activity. Thermal activation

converts the crystalline state of clay to an amorphous phase (metakaolinite), making the alumina in the clay acid soluble.

The thermal transformation of clay involves four crucial temperature ranges: free water dehydration (50 – 120 °C), clay stability (120–600 °C), anhydrous clay between 600 to 900 °C, and recrystallization above 900 °C (Udochukwu *et al.*, 2019a). Thermal activation typically occurs between dehydration (50-600 °C) and dehydroxylation (600-900 °C) (Udochukwu *et al.*, 2019c). Dehydration decreases the amount of adsorbed water, whereas dehydroxylation reduces structural water and changes the macroporosity and microporosity of clay minerals (Bergaya *et al.*, 2006; Stevenson and Gurnick, 2016). As crystalline phases develop, clay minerals undergo changes in their original crystallographic alignment (Barakan and Aghazadeh, 2021). The composition of clay materials includes three different types of water molecules: interlayer and physisorbed water, which is weakly attached to a surface and eliminated through heat treatment below 200 °C, and water molecules included within the primary interlayer ions coordination sphere (Ghafar *et al.*, 2020). These molecules are strongly bonded and must be removed through high-temperature treatments ranging from 300 °C to 500 °C (ElDeeb *et al.*, 2019). Within the temperature range 500–800 °C, structural hydroxyl groups have the potential to undergo condensation and dehydration (ElDeeb *et al.*, 2019).

Dehydroxylation of kaolinite during thermal activation is a topic of significant interest. As kaolinite is relatively acid-insoluble, it must undergo thermal dehydroxylation to produce metakaolinite(Johnston *et al.*, 2022a). The process of dehydroxylation transforms kaolinite into metakaolinite by eliminating hydroxyl ions that are chemically bound within kaolin. This leads to disintegration of the crystalline structure of kaolin, resulting in an amorphous aluminosilicate phase (metakaolinite) (ElDeeb *et al.*, 2019). The dehydroxylation process is influenced by heating factors, including duration and temperature, along with heating and cooling rates under atmospheric conditions (ElDeeb *et al.*, 2019).

Kaolinite to metakaolinite conversion via thermal dehydroxylation is a two-step process that requires breaking of two OH groups. The initial stage of the process entails the delocalization of a proton from the first OH group, followed by the

displacement of the delocalized proton to the second proton, as shown in Equation 2.1 (Johnston *et al.*, 2022a). Water is liberated, and chemically bound oxygen remains. The movement of aluminum to the empty positions inhabited by hydroxyls leads to a coordination number decrease of aluminum from VI to V and IV (Johnston *et al.*, 2022a). This results in the formation of metakaolinite in the kaolinite crystal structure caused by the distortion of the alumina layer, resulting in disorder. (Johnston *et al.*, 2022a).

$$OH^- \leftrightarrow H^+ + O^{2-} + H^+ + OH^- \leftrightarrow H_2O_{(g)} \qquad 2.1$$

The dehydroxylation process leads to a notable reduction in the basal distance and was accompanied by interlayer space collapse. The interlayer distance refers to the distance between two layers, while the basal distance is determined by the thickness of a single layer and the interlayer distance. The removal of hydroxyl groups from the inner layers results in disorder within the layers, causing them to expand and ultimately reduce the interlayer spacing (Sperinck *et al.*, 2011;Varadwaj and Parida, 2013).

Aluminum has a coordination number of VI to oxygen in the kaolinite composition. The influx of aluminum into these recently vacated sites results in silica-alumina layer destabilization and transforms the alumina geometry from coordination number VI to V or IV (Johnston *et al.*, 2022a). The increased proportion of V-coordinated aluminum and the altered geometry are the reasons for higher acid solubility of metakaolinite relative to kaolinite. The silicon layers have relatively few disorders, confirming that kaolinite to metakaolinite structural conversion is guided by the movement and reorganization of the layers of aluminum (Sperinck *et al.*, 2011).

The three primary stages of thermal calcination of kaolinite are characterized by endothermic dehydroxylation, include the formation of metastable metakaolin as seen in Equation 2.2, amorphous silica, and cubic spinel, as well as the thermodynamically stable mullite phase (Sperinck *et al.*, 2011). Endothermic

dehydroxylation to the metakaolinite phase typically occurs in the range 450–700 °C. At temperature range of 700–950 °C, cubic spinel and amorphous silica are produced (Sperinck *et al.*, 2011). Above 1100 °C, an exothermic reaction occurs, resulting in mullite phase formation, accompanied by cristobalite crystallization from the amorphous silica phase (Sperinck *et al.*, 2011).

$$Al_2O_3 \cdot 2SiO_2 \cdot 2H_2O \rightarrow Al_2O_3 \cdot 2SiO_2 + 2H_2O \qquad 2.2$$

In Equation 2.2, during dehydroxylation, water vapor accounts for approximately 13.96% of the kaolin stoichiometric mass (ElDeeb *et al.*, 2019). From approximately 950 °C, Metakaolin undergoes additional reactions that lead to the formation of crystalline compounds, resulting in the final product of free silica (cristobalite) and mullite ($3Al_2O_3.2SiO_2$) (Udochukwu *et al.*, 2019c), as shown in Equation 2.3 to 2.5, respectively.

$$2(Al_2O_3 \cdot 2SiO_2) \rightarrow 2Al_2O_3 \cdot 3SiO_2 + SiO_2 \qquad 2.3$$

$$2Al_2O_3 \cdot 2SiO_2 \rightarrow 2(Al_2O_3 \cdot SiO_2) + 2SiO_2 \qquad 2.4$$

$$3(Al_2O_3 \cdot SiO_2) \rightarrow 3Al_2O_3 \cdot 2SiO_2 + SiO_2 \qquad 2.5$$

The loss of water physically attached to the surface in kaolinite is a minor weight loss that does not change the crystal lattice of the clay (Udochukwu *et al.*, 2019). On the other hand, chemically bound water loss (endothermic process) results in loss of weight. The phase changes in kaolinite depend on the degree of crystallinity, impurity oxide content, particle size, heating rate, and heating duration at a specific temperature (Khalifa *et al.*, 2020). Therefore, because of the variation in the chemical composition, degree of crystallinity, mineralogy, and purity of clays from various locations, investigations on the thermal transformation of clays from various locations are necessary. (Udochukwu *et al.*, 2019).

2.3.3. Chemical activation or modification

Chemical activation or modification has a profound influence on material structure and properties, primarily because of the chemical interactions between the modifying agent and material surface (Libbohole and Kennedy, 2022). Acid and alkaline solutions are the most used solutions for industrial or laboratory processing of clays.

2.3.3.1. Acid activation

The interaction between aluminosilicate and an acidic solution triggers a sequence of reactions. Typically, clay minerals exhibit ion-exchange properties, which initiate ion-exchange processes. The interlayer space often contains exchangeable cations, which can include alkaline or alkaline earth elements such as sodium, potassium, or calcium, represented as Na^+, K^+, or Ca^{2+}. In this process, known as cation exchange, these cations replace protons generated by the dissociation of an acid (Novikova and Belchinskaya, 2016). Simultaneously, the layered structure undergoes acid attack. The interlayer space of the acid readily allows protons to enter and undergo a reaction with the cations in the octahedral sheet through a process called dealumination (Novikova and Belchinskaya, 2016). Dealumination involves the replacement of octahedral Fe^{3+}/Fe^{2+} or Al^{3+} ions with protons, which results in the formation of extra Si-OH groups within the tetrahedral sheet.

2.3.3.2. Alkaline activation

Alkaline activation is prevalent in industrial clay processing for applications such as mud drilling. Various activating agents, including alkalis (NaOH, LiOH and KOH), alkaline salts (Na_2CO_3 and Na_2SiO_3), alkaline earth metals ($CaSO_4$), and oxides (MgO), with mass percentages of approximately between 2 to 4%, are employed in this process (Novikova and Belchinskaya, 2016). The alkaline treatment chemically dissolving Al_2O_3 and SiO_2 in the alkali, forming sodium aluminate and sodium silicates, respectively. Furthermore, alkaline treatment selectively impacts tetrahedral sheets. In alkaline media, the Si-O-Si bond exhibits

lower stability compared to the Si-O-Al bond, making it easier for Si^{4+} to be transferred from the aluminosilicate structure to the solution than Al^{3+} (Novikova and Belchinskaya, 2016). Consequently, tetrahedral sheets undergo a chemical reaction with an alkaline solution, leading to the formation of either an amorphous or a crystalline aluminosilicate phase (Novikova and Belchinskaya, 2016).

2.4. Alumina production

Various processes have been established for alumina production. Different routes have been designed to improve alumina extraction efficiencies from mineral ores at low operational costs.

2.4.1. Bayer process

Alumina is produced from bauxite ore via the Bayer process. This method involves treating the ore with an alkali solution containing NaOH, as illustrated in Figure 2.3. High-quality bauxite is subjected to pressure leaching with a NaOH solution, resulting in sodium aluminate solution, which is then crystallized to form aluminum hydroxide through seeding (Donaldson and Raahauge, 2008). Bauxite is also a principal source of Ga, which is recovered from the Bayer process. Aluminum hydroxides from bauxite dissolve selectively during leaching at a high pH, elevated temperature, and pressure, whereas red mud, which is a solid waste desilication product, remains insoluble (Sellaeg *et al.*, 2017). Different types of bauxites were treated under different conditions. Trihydrates are treated at digestion temperatures of 130-150°C, whereas boehmite is treated at 205-245°C (Kaußen and Friedrich, 2016). Diaspores, however, require the highest temperatures above 250°C. (Kaußen and Friedrich, 2016).

Silica is generally insoluble in NaOH solutions and quartz is attacked by sodium hydroxide at high temperatures. When caustic soda reacts with dissolved aluminum in a solution containing silica, silica becomes unstable and precipitates immediately. The resulting products, such as sodalite and cancrinite, along with other insoluble compounds, are present in the final red mud, leading to a significant

loss of aluminum (Kaußen and Friedrich, 2016; Van *et al*., 2012). Thus, the Bayer process has been found to be inefficient in utilizing low grade, high silica bauxite ores. This process requires high-grade bauxite ore with a silica content of less than 7% (Ali and Al-taie, 2019). However, the sintering process is more suitable for low-grade materials because it produces silica-rich phases that can be easily transformed into non-leachable calcium silicate and calcium and sodium aluminate phases that are leachable (ElDeeb *et al.*, 2020).

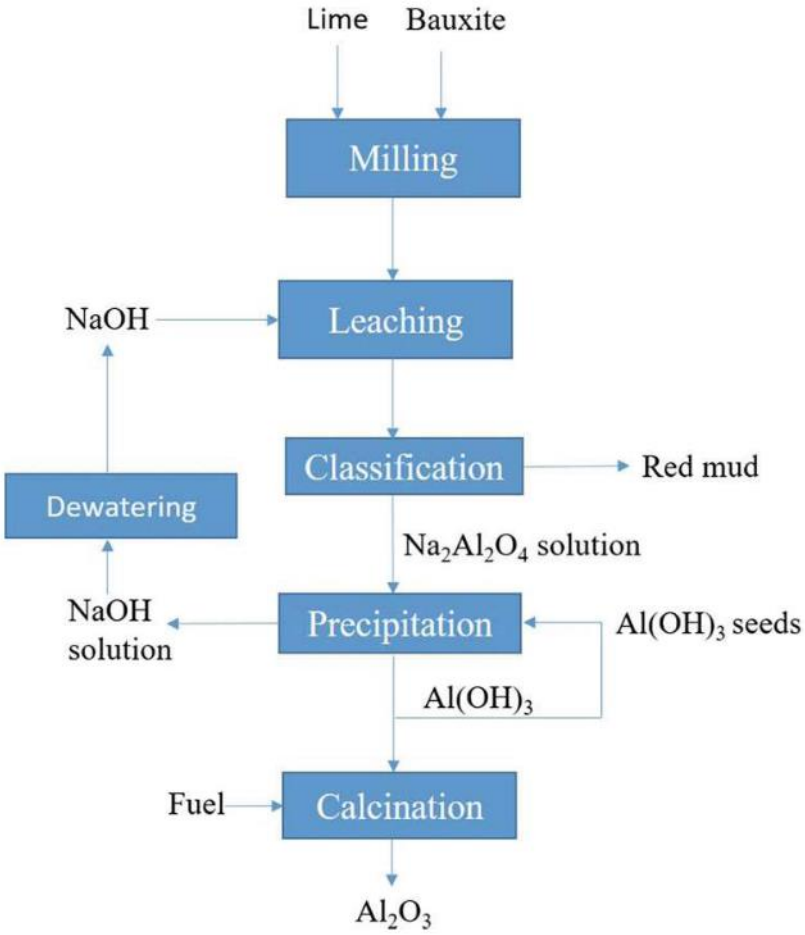

Figure 2.3: Production of alumina via the Bayer process (Sellaeg *et al.*, 2017).

2.4.2. Aluminosilicates sintering

Sintering involves a high-temperature reaction between a mineral source and a sintering agent to create soluble alumina compounds. Two primary sintering techniques exist: the lime sinter process and the soda-lime sintering method. In the

soda-lime sintering method, clay is initially sintered with lime, followed by leaching with a strong alkali solution (Wang *et al.*, 2023). The typical sequence of the sintering process typically commences with the pretreatment of the feedstock, followed by alkaline or acidic leaching process, separation of solid-liquid mixture, and concludes with the precipitation or crystallization processes, ultimately resulting in the final aluminum products (ElDeeb *et al.*, 2020).

In the lime sinter process, there are several sequential steps for clay processing. The clay ground is initially combined with ground calcium carbonate, resulting in a mixture that, upon sintering at an optimal temperature of approximately 1350 °C, produces a composition consisting primarily of calcium aluminate compounds, including $CaO{\cdot}Al_2O_3$ and $12CaO{\cdot}7Al_2O_3$ and dicalcium aluminate (2CaO·SiO2) (ElDeeb *et al.*, 2019). Secondly, calcium aluminate compounds are leached using dilute sodium carbonate solution to dissolve the alumina and from which sodium aluminate is formed. This process leaves most of the lime and silica in the sintered and undissolved material. Thirdly, the sodium aluminate solution undergoes treatment with carbon dioxide to induce precipitation of alumina trihydrate (gibbsite) and concurrently regenerating the sodium carbonate solution, permitting recycling (Al-ajeel *et al.*, 2014). Finally, the gibbsite is calcined at 1350 °C producing the αAl_2O_3 phase (ElDeeb *et al.*, 2019).

The temperature at which sintering occurs has a significant impact on the transformation of phases, and it performs an essential role in increasing the percentage of recovered alumina. During sintering, kaolinite undergoes a phase transformation into metakaolinite, whereas calcite is broken down into calcium oxide, which then combines with other elements to form calcium aluminate compounds (ElDeeb *et al.*, 2020). These phases play a vital role as the initial precursor phases in alumina extraction, highlighting the important role of the sintering temperature in their formation (Allegretta *et al.*, 2016). The sinter product is composed of aluminosilicate with a wide range of compositions, calcium silicate, and calcium aluminates. Lower sintering temperatures (800 – 1200°C) are insufficient for the formation of calcium silicates (C_2S) (Luo et al., 2022; Cao *et al.*, 2022). Upon cooling, C_2S is crystallographically transformed, which results in molar volume increase owing to the transformation of 2CaO. SiO_2 from β to ɣ form

(Al-ajeel *et al.*, 2014). In contrast, higher sintering temperatures (1300 – 1400 °C) are sufficient for the formation of C_2S, which leads to the transformation of the sintered briquettes into a fine powder (ElDeeb *et al.*, 2019). This transformation increased the solubility of alumina-containing compounds without any further grinding requirements (Luo et al., 2022; Cao *et al.*, 2022). High sintering temperatures allow the complete kaolinite dehydroxylation, decomposition of calcium carbonate, and melting of original constituents with the formation of calcium aluminates and calcium silicates in different forms. However, increasing the sintering temperature to over 1360 °C results in the development of a mullite phase ($3Al_2O_3.2SiO_2$) (ElDeeb *et al.*, 2019). This phase makes alumina extraction challenging.

The desirable and most easily extractable end products obtained by sintering the limestone-kaolin mixture are calcium aluminate phases, including$12CaO.7Al_2O_3$ and $CaO.Al_2O_3$, achieved through the lime sinter process, and soda-lime sintering process producing $Na_2O.Al_2O_3$ (ElDeeb *et al.*, 2020). The sintered product enriched with calcium aluminate phases is soluble in NaOH and sodium carbonate solutions, whereas the sintered product enriched with the sodium aluminate phase dissolves in hot water (ElDeeb *et al.*, 2020).

2.4.3. Alternative processes

The recovery of alumina from aluminosilicate clay minerals is mainly achieved through acid and alkaline leaching. However, these processes have not been deemed economically viable for competition with the Bayer process. Despite progress from laboratory plants to semi-industrial tests, they have not yet advanced to the plant demonstration stage because of the elevated silica to alumina ratio in non-bauxite ores, which increases the energy requirements (Donaldson and Raahauge, 2008). Comparatively, calcining precipitated aluminum hydroxide, which is attained through the Bayer process, is simpler than that of aluminum chloride ($AlCl_3$) salt, which is obtained through the HCl leaching of non-bauxite materials (Barry *et al.*, 2019). Additionally, eliminating silica because of its solubility prior to the carbonation of aluminate solutions via alkaline leaching poses challenges, whereas

removing dissolved iron before alumina precipitation through acid leaching also presents constraints (Barry *et al.*, 2019).

Typically, two methods are used for extracting alumina from clays: alkali leaching and acid leaching. Acid leaching involves the application of nitric acid, sulfuric acid, or hydrochloric acid in which alumina is preferentially dissolved after roasting or calcination of the clay, as depicted in Figure 2.4. Alkali leaching, on the other hand, employs diluted alkali in which alumina is preferentially dissolved from a sintered combination of clay, lime, and soda or lime and clay. (Al-ajeel *et al.*, 2014).

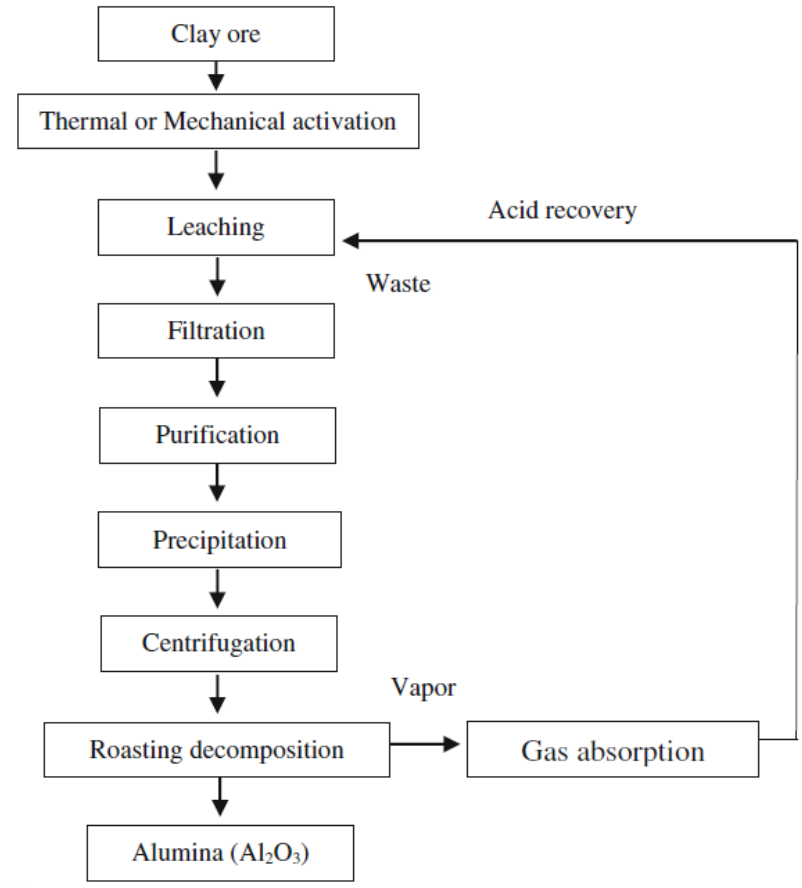

Figure 2.4: Basic processes of alumina production from clay minerals (Barry *et al.*, 2019)

The extraction of alumina from clay involves four main stages: thermal activation through calcination, acid leaching of the calcined clay, precipitation of aluminum salt from the leachate, and roasting to transform the aluminum salt into alumina (Lu et al., 2020; Erdemoğlu *et al.*, 2020a). The degree of dissolution is influenced by

the type of clay mineral and factors such as acid concentration, acid-to-clay ratio, reaction temperature, and time (Ajemba and Onukwuli, 2012a). The principle of alkaline processes is to transform the alumina in the ore to sodium aluminate. The extraction of alumina from ore involves treating it with an alkali solution to create soluble sodium aluminate, which is then hydrolyzed to produce aluminum hydroxide. This hydroxide is further processed by calcination to produce alumina (Aly *et al.*, 2019).

2.4.3.1. Acid leaching

Hydrochloric, nitric, and sulfuric acids are the most commonly used acids for leaching aluminous minerals. With low-alumina high-silica minerals, the separation of alumina from silica is more readily achieved with acid processes, in which silica is sparingly soluble, compared with alkaline processes, in which silica is significantly soluble (Daniels *et al.*, 2012).

2.4.3.1.1. Hydrochloric acid leaching

The HCl process comprises four main stages: thermal dehydroxylation, HCl leaching of aluminum-bearing materials, aluminum chloride hexahydrate precipitation, and thermal decomposition, resulting in the formation of alumina (Pepper *et al.*, 2021). Thermal dehydroxylation plays a vital role in enhancing the acid solubility of aluminum (Lu et al., 2020).

Calcined clay and other aluminous materials were leached using hydrochloric acid. Aluminum and iron pass into the solution as soluble chlorides, along with most alkaline metals and a minor quantity of silica (Daniels *et al.*, 2012). The methods used to remove iron from the solution and subsequent treatment to obtain anhydrous alumina may differ. For instance, the treated leach solution may undergo solvent extraction to eliminate iron. The purified leach solution is subsequently concentrated by evaporation to increase the concentration of $AlCl_3$, and $AlCl_3.H_2O$

is crystallized through the introduction of HCl gas, as $AlCl_3.H_2O$ exhibits near insolubility in concentrated HCl solutions (David, 2018). These crystals are then calcined to produce Al_2O_3, whereas HCl is recovered from the off gases. The residual solution is heated to recover some HCl gas and is then adjusted to the appropriate acidity before being reintroduced into the leaching process. The selective precipitation of aluminum chloride hexahydrate from leaching solutions offers the advantage of using hydrochloric acid as the leaching reagent (Pak *et al.*, 2019). In contrast to nitric and sulfuric acids, the hydrochloric acid method is the simplest method for acid regeneration (Pak *et al.*, 2019). The gaseous HCl is then collected through water after the thermohydrolysis of aluminum chloride and iron crystals, followed by its recycling for leaching.

2.4.3.1.2. Sulfuric acid leaching

This process involves several steps. First, clay is calcined and leached using H_2SO_3. Subsequently, the silica that did not dissolve is filtered out from the resulting solution. Next, monobasic aluminum sulfite is precipitated from the saturated solution. Following this, the precipitate is decomposed to produce unrefined alumina. Finally, the crude alumina is purified through caustic digestion or reprecipitation (Lima et al., 2014; Ibrahim et al., 2018). When calcined clay is treated with sulfurous acid, it yields aluminum sulfite and silica residue, as shown in Equation *2.6*. In this process, aluminum, iron, and alkaline metals are dissolved as sulfates.

$$3H_2SO_3 + Al_2O_3 \cdot 2SiO_2 \rightarrow Al_2(SO_3)_3 + 2SiO_2 + 3H_2O \qquad 2.6$$

2.4.3.1.3. Nitric acid leaching

There are two approaches to nitric acid leaching of aluminous materials: the first is to use an excess of acid that dissolves most of the aluminum and iron, and the second is to use a deficiency of nitric acid, that is, less than the stoichiometric

amount required to convert all aluminum to aluminum nitrate nonahydrate (Hamer, 1977; Barry *et al.*, 2019; Higbie, 1967). Under the latter condition, little iron is dissolved, and the dissolved iron is precipitated. The alumina extraction is lower because there is insufficient acid to react with alumina. Compared to other acids, nitric acid processes require longer leaching times and are often performed under pressure (Daniels *et al.*, 2012).

2.4.3.2. Sinter-leaching

During this process, the clay is transformed into a sinter, which is then heated with sodium carbonate and limestone to create sodium aluminate from alumina and dicalcium silicate from silica. Next, the sinter is treated with a sodium carbonate solution to dissolve the sodium aluminate. Following this, the solution is subjected to high pressure and heat in the presence of lime, leading to the removal of the bulk of the silica present in the sodium aluminate. The purified solution is precipitated as alumina trihydrate using carbonate, and the precipitate subsequently calcined to produce alumina (Barry *et al.*, 2019).

2.4.4. Selectivity of impurities in acid leaching

The presence of impurities in ore minerals can manifest in several ways: (1) minerals that are not chemically bonded to other minerals and exist as isolated particles, (2) fragments that attach to mineral surfaces through chemical and physical interactions, (3) mineral particles or aggregates that surround or are enclosed by other mineral particles, forming a composite structure, and (4) atoms or ions that replace other atoms within the mineral lattice or occupy the spaces between them. (Liu *et al.*, 2023). The ways in which various elements exist and are formed are summarized in Table 2.1. During the extraction of alumina using HCl leaching, impurities including Ca, Fe, K, Na, Ti, and Mg in the clays are dissolved in the acid leachate.

Table 2.1: The occurrence states and forms of alumina impurities (Liu et al., 2023)

Impurity elements	Occurrence	Forms
Fe	Independent minerals, isomorphism, inclusion	Micro inclusion, Fe^{3+} replacement lattice Al^{3+}
Ca	Independent mineral, inclusion	Ca^{2+} in inclusions, calcite
K	Inclusion, isomorphism, independent mineral,	Clay minerals, muscovite, K^{+} in inclusions, impurity charge compensation
Na	independent mineral, inclusion, Isomorphism	Impurity charge compensation, mica, Na^{+} in inclusions
Ti	Independent mineral, Isomorphism	Rutile, Ti^{4+} replacement lattice Al^{3+}
Mg	Inclusion, independent mineral	Muscovite, Mg^{2+} in inclusion, mica

Impurity elements within ore minerals can manifest in various forms, including minerals, lattice impurities, and fluid inclusions. Quartz, with its tetrahedral structure and resilient Si-O bonds, only allows a limited number of trace impurity elements to be incorporated into its crystal lattice through isomorphism. Substitutions such as Fe^{3+}, Ti^{4+}, and P^{5+} have been identified (Liu *et al.*, 2023), and various ions can substitute Si^{4+} within the three-dimensional lattice of SiO_2. Iron can be found in both the octahedral and tetrahedral sheets of 1:1 and 2:1 clay minerals, as well as in the gibbsite/brucite sheet of 2:1:1 minerals (Bergaya *et al.*, 2006). Additionally, Iron can function as a compensating ion in the clay exchange complex or it can be situated in the pillars that exist between the 2:1 layers (Bergaya *et al.*, 2006). Iron impurities often exist in finely-grained states within kaolinized feldspar or clay: an iron oxide layer adheres to the surface of quartz, while Fe-containing minerals are inherent within quartz particles in a diffuse state and are

present in quartz as a solid solution (Liu *et al.*, 2023). The iron impurities adhering to the mineral particle surfaces are dissolved; subsequently, the iron enclosed within the aggregates becomes exposed to the acidic solution and dissolves. This process involves the mechanical breakdown of the aggregates and their exposure to mechanical stirring (Liu *et al.*, 2023). The factors influencing the dissolution behavior of iron oxides include surface area and crystal morphology (Lee, 2005). In heterogeneous reactions that occur at the solid/liquid interface, the rate is influenced by the surface area. In addition to the surface area considerations, oxides exhibit varying crystal structures, leading to different behaviors among samples of the same oxide. The strong attraction between protons and structural O^{2-} aids in the release of iron, particularly under acidic conditions (Lee, 2005).

Minerals, such as dolomite and calcite, are commonly linked with impurities, which may influence the calcination process. These impurities typically include iron or manganese, which can be present either through Fe direct substitution within the mineral lattice or as separate minerals such as dolomite and calcite (Abdullah *et al.*, 2021). Evaluating the reactivity of impurities in the thermal treatment (calcination) and their reactivity in the extraction process is important to mitigate the challenges associated with impurities in the downstream process.

2.5. Process challenges

The production of alumina presents several challenges that must be overcome to ensure its efficient and reliable processing. From mineral decomposition to chemical reactions, addressing these complexities is crucial for optimizing alumina production processes.

2.5.1. Bayer process

The increasing demand for alumina and aluminum is unquestionable; however, the reserves of bauxite ores have limitations as they contain diminishing amounts of alumina (Pepper *et al.*, 2021; Barry *et al.*, 2019). In response to this issue, countries without bauxite reserves or where the expense of extracting bauxite ore through the

Bayer process is not economically viable have investigated alternative sources of alumina. Moreover, nations with restricted bauxite reserves aim to reduce their reliance on external sources by exploring alternative avenues for obtaining alumina.

The aluminum industry faces numerous challenges, including the limitation of the Bayer process to handle bauxite ore with high silica content of greater than 7%, extensive consumption of caustic soda, low alumina-to-silicate ratio, elevated silica formation, substantial volumes of process waste, and storage complications for red mud. (Barry *et al.*, 2019). Additionally, the Bayer process introduces contaminants, such as sodium and gallium, which restrict the overall purity of the produced alumina (Pepper *et al.*, 2021; Evans, 2016). Typically, a purity level of 99.6 to 99.9% is required (Pepper *et al.*, 2021).

Higher temperatures are essential for the efficient extraction of alumina from bauxite during the Bayer process, which is contingent on the mineral composition of the processed bauxite. Primary aluminum phases found in bauxite include trihydrates (gibbsite) or monohydrates (boehmite, and diaspore). Trihydrates exhibit greater solubility at temperatures varying from approximately 135 °C to 150 °C, whereas boehmite requires treatment within a temperature range of 205 °C to 245 °C, and diaspores require the peak digestion temperature to surpass 250 °C (Kaußen and Friedrich, 2016). Nevertheless, elevated leaching temperatures increase the reactivity of impurities such as silica, which stands out as the most detrimental impurity owing to its abundance and influence. (Pehlivan *et al.*, 2012). The formation of sodium aluminum silicates reduces the recovery of aluminum (Kauben and Friedrich, 2016), and the use of silica in the precipitation process leads to a reduction in the levels of beneficial caustic and alumina, causing a gradual liberation of soda from the red mud residues that accumulate during storage (Pehlivan *et al.*, 2012). Bauxite typically contains 30-60% Al_2O_3, and the deposited red mud contains residual amounts of aluminum ranging from 10-25% Al_2O_3 (Kauben and Friedrich, 2016). However, this process generates a substantial amount of red mud as waste, which presents storage challenges.

2.5.2. Sintering

The sintering process for alumina production requires high temperatures of 1300 – 1400 °C, which makes it economically unfeasible because of its high energy requirements (Luo et al., 2022; Cao *et al.*, 2022). The byproduct sodium titanate causes soda losses, but does not affect the subsequent leaching step in the soda sintering process (Kaußen and Friedrich, 2016). Sodium silicate (Na_2SiO_3) is water-soluble and can contaminate leachate (Kaußen and Friedrich, 2016). Despite the possibility of leaching alumina from the sintered product by using a diluted alkali solution, a substantial amount of residual $2CaO.SiO_2$ produced during leaching necessitates additional treatment for efficient utilization (Cao *et al.*, 2022).

2.5.3. Acid and alkaline processes

The challenges involved with acid techniques include iron removal, in which iron is generally soluble in acids; removing the small but still significant amount of silica, which is soluble in some solutions; acid recovery and regeneration; handling and calcining aluminum salts, most of which contain considerable amounts of water for hydration; and the need for acid-resistant equipment (Daniels *et al.*, 2012).

When processing kaolin using the acid method, the presence of silica does not disturb alumina leaching, but iron oxides are the most impediment. The challenge involves the removal of iron solubilized during acid leaching, which has been overcome by the development of HCl acid sparging crystallization of $AlCl_3.6H_2O$, which achieves good purification with respect to iron and recovery of the leaching reagents (Donaldson and Raahauge, 2008). When HCl gas is sparged through the leached solution, aluminum chloride hexahydrate is crystallized, while Fe^{3+} forms strong chloride complexes and persists in solution.

In contrast, alkaline processes introduce silica into the solution, which presents a challenge for the subsequent alumina separation (Kaußen and Friedrich, 2016; Crundwell, 2014; Barry *et al.*, 2019). However, alkaline reagents do not dissolve iron. The challenge is to eliminate the majority of the soluble silica from the

solution to decrease the silica content in the precipitated alumina to a level below a tolerable threshold.

2.6. Previous investigations

The studies that investigated the recovery of Al from clays using hydrochloric acid has been reviewed in this subsection, highlighting alumina extraction efficiency results and the impact of calcination temperature on the reactivity of clay to acid leaching.

In Table 2.2, Al extraction efficiencies are compared between different types of activation methods. For thermal activation, kaolin calcined at 600°C for 1 hour yielded Al extraction efficiencies of 89.34 wt% and 83.37 wt% for low-grade and high-grade kaolin, respectively (Si *et al.*, 2012). A higher calcination temperature (750°C for 3 hours) applied to kaolinite and kaolinitic sand gave lower Al extraction efficiencies (35.33% for MT and 44.67% for LT) (San Cristóbal *et al.*, 2009). Kaolin calcined at 700°C for 2 hours achieved 83.20% Al extraction efficiency (Aly *et al.*, 2019), while pyrophyllite clay ore calcined at 900°C for 30 minutes reached 90.57% (Lu et al., 2020). Mechanical milling showed variation in Al extraction. Kaolin ground for 5 hours yielded 86.46% for low-grade and 74.08% for high-grade material, and extended milling to 10 hours further improved efficiency to 98.75% and 92.11%, respectively (Si *et al.*, 2012). Mechanical activation on kaolinitic sand produced 33.90% (MO) and 71.60% (LO) Al extraction efficiency (San Cristóbal *et al.*, 2009). Milling pyrophyllite for 50 minutes yielded 73.09% (Erdemoğlu *et al.*, 2018). Temperatures ranging from 600°C to 900°C in thermal activation and extended milling times in mechanical activation correlated with higher Al extraction efficiencies. However, the efficiency depended on the specific material and its properties.

Table 2.2: Comparison between activation techniques and Al extraction efficiencies

Source	Activation method	Activation conditions	Leaching conditions	Al extraction efficiency	Reference
Kaolin	Thermal (calcination)	600°C, 1 h	20wt% HCl, 98°C, 30 min, mass ratio of solid to acid of 5	Low-grade kaolin: 89.34 wt%, High-grade kaolin: 83.37 wt%	(Si *et al.*, 2012)
Kaolin	Mechanical (milling)	5,10, and 20 hours, 350 r/min, mass of grinding medium with diameters of 20, 10 and 5 mm was 120, 180 and 120 g, respectively	20wt% HCl, 98°C, 30 min, mass ratio of solid to acid of 5	After 5 hours of milling:Low-grade kaolin: 86.46 wt%,High-grade kaolin: 74.08 wt% After 10 hours of milling:Low-grade kaolin: 98.75 wt%,High-grade kaolin: 92.11 wt% After 20 hours of milling:Low-grade kaolin: 98.34 wt%, High-grade kaolin: 94.78 wt%	(Si *et al.*, 2012)
Kaolinite and kaoliniferous sand	Thermal (calcination)	750 °C, 3 h	6 M HCl, 90°C, 3 h	MT:35.33%, LT:44.67%	(San Cristóbal *et al.*, 2009)
Kaolinite and kaoliniferous sand	Mechanical (milling)	50 Hz, 1.1 Kw and 1420 rpm for 30 min (MO) or 60 min (LO)	6 M HCl, 90°C, 3 h	MO:33.90%, LO:71.60%	(San Cristóbal *et al.*, 2009)
Kaolin	Thermal (calcination)	700°C, 2h	104°C, 3 h, 1:5 S/L ratio, 260 rpm	83,20%	(Aly *et al.*, 2019)
Clay ore: mainly pyrophyllite	Mechanical (milling)	50 min	4 mol/l HCl, 108°C, 24 h, 20 l/kg S/L ratio	73.09%	(Erdemoğlu *et al.*, 2018)
Clay ore: pyrophyllite, kaolinite, muscovite, quartz and kyanite	Thermal (calcination)	900°C,30 min	4 M HCl, 10g of sample in 200 ml HCl solution, 600 rpm	90.57%	(Lu et al., 2020)

Table 2.3: Summary of previous investigations on Al extraction from kaolinitic clays

Source	Calcination		Leaching						Ref.
	T(°C)	Time (h)	HCl Conc (M)	T(°C)	Time (h)	S/L ratio	Stirring speed (rpm)	Al recovery (%)	
Kaolin (Iraq Alduikhla astrologer)	700	2	Ph=0.45	30	2	20 g calcined kaolin: 60 ml HCl		70	(Ali and Al-taie, 2019)
Nawan kaolin (13 km to the southeast of Nawan city, Al Baha, KSA within coordinates (19o29'10.27" N and 41o15'20.27" E))	850	2	6	90	3	0.1 g/ml	500	75	(Tantawy and Alomari, 2019)
Ibere clay (southeastern Nigeria)	600	1	1	100	1			50.27	(Udochukwu *et al.*, 2019)
Aku clay ("Aku" in Enugu State Eastern Province of Nigeria)	820		2.2 mol/dm^3	67	1 h, 1 min	12.9 ml/g		78.40%	(Ogbonnaya *et al.*, 2018)
Kaolin (Harad Formation, about 75 Km to southeast of Ma'an city within coordinates (29◦39'3.94" N and 35◦57'20.17" E))	700	3	40 wt% H_2SO_4 and 120 ml HCl	140	3h 45 min			79.28	(Ibrahim *et al.*, 2018)
Kaolin (Shanxi (K-SX) and Jiangsu (K-JS))	600		20 wt% HCl	98	30 min	Mass ratio of solid to acid of 5		K-JS: 89.34, K-SX:83.37	(Si *et al.*, 2012)
kaolin ore (Kalabsha region, Aswan, Egypt)	700	2		104	3	01:05	260	83.2	(Aly *et al.*, 2019)
Edda clay (southeastern Nigeria)	700	1	1	100	1	0.02 g/ml	100	49.96	(Udochukwu *et al.*, 2019a)
Ethiopian kaolinite (Shakiso, which is located 5° 45′N, 38° 55′E, Southern Ethiopia)	700	3	3	80	2	12 ml/g liquid-to - solid ratio	700	71.28	(Kassa *et al.*, 2022)

Source	Calcination		Leaching						Ref.
	T(°C)	Time (h)	HCl Conc (M)	T(°C)	Time (h)	S/L ratio	Stirring speed (rpm)	Al recovery (%)	
Pyrophyllite ore (Pütürge clay deposits in Malatya (Turkey))	900		4	~108		10 g sample:200 ml acid solution	600	90.57	(Erdemoğlu *et al.*, 2020)
Kaolinitic clay (Saudi Arabia)	600	1	3	Boiling conditions	1	10 ml acid/gm clay		63	(Al-Zahrani and Abdul-Majid, 2009)
Kaolin (northeastern deposits of Iran was)	850	3	6	90	3	0.25 g/ml	500	98	(Bagherzadeh *et al.*, 2023)
Natural Spanish kaolin (Navalacruz deposit, Zamora province)	600-900	10	6	90	6 and 24	6.0 g:180 ml acid solutions		90 and 95	(Belver *et al.*, 2002)
kaolin clay (Chovdardagh deposit)	750	2	20% HCl	95	2			96.7	(Efendiyeva *et al.*, 2023)
Clay sample (Ogbunike (N: 6° 11' 5"; E:6° 50' 39"; A: 113 m) in Anambra State, Southeast region of Nigeria	700	1	3	90		0.2 g/ml		84.72	(Okwuzu *et al.*, 2022)
kaolin (Milos Island, Greece)	850	2	1N HCl	80	6	3 g/300 ml	500	82	(Kyriakogona *et al.*, 2017)
Ihiala (A) clay (Ihiala Local Government Area, Anambra State),Nsu (B) clay (Mbano Local government Area Imo State), Umuhu(C) clay (Orsu Local Government Area, Imo State)	700	1	5	100	76 min			81% for A, 79% for B, 79% for C	(Al-Zahrani and Abdul-Majid, 2009)

Johnston *et al.* (2022a) investigated the feasibility of aluminum extraction from low-grade and high-grade kaolin. The research findings revealed that for low-grade kaolin, achieving complete thermal dehydroxylation, necessary for rendering aluminum soluble, took place at a lower temperature (450°C) relative to high-grade kaolin, which required 650°C for full dehydroxylation. This temperature variance was attributed to the different crystallinity and purity levels of the kaolin samples. The occurrence of iron oxide phases in low-grade kaolin led to formation of insoluble aluminum spinels at temperatures exceeding 750°C, thereby reducing the acid solubility of both aluminum and iron. Nevertheless, the lower temperature requirement for full dehydroxylation of low-grade kaolin suggested a lower energy demand for aluminum extraction, despite the diminished acid solubility due to spinel formation. Conversely, in high-grade kaolin, the absence of significant iron oxide phases prevented spinel formation, enabling a higher dissolution of aluminum. The fractional conversion to soluble aluminum notably increased at temperatures exceeding 500°C, peaked at 600°C, and remained consistent thereafter. This observation indicated that the calcination temperature directly influenced the reactivity of kaolin towards acid, with higher temperatures facilitating the transformation of kaolinite to metakaolin, which exhibits enhanced reactivity to acid leaching.

Johnston *et al.* (2022b) explored aluminum extraction from kaolinite, focusing on the influence of iron impurities on the process. The study found that the calcination temperature, specifically thermal dehydroxylation conducted at 600°C for 1 hour, played a crucial role in preparing the clay for the dissolution process by removing hydroxyl groups and potentially making the aluminum within the clay more accessible to the leaching acid. It was further stated that this pretreatment step was essential for enhancing the reactivity of the clay to the acid, thereby potentially increasing the efficiency of alumina extraction. The effectiveness of obtaining alumina from clay was affected by the presence of impurities and the calcination temperature, as these factors affect the responsiveness of clay to acid.

Ali and Al-taie, (2019) reported that the alumina extraction efficiency from kaolin was significantly influenced by the calcination temperature, with the optimal temperature for maximizing alumina extraction being 700°C for 2 h. At this temperature, the activation of the alumina layer within the kaolin structure increased, leading to an Al extraction rate of 70% at leaching conditions of pH of 0.45, temperature of 30 °C and time of 2 h. However, as the calcination temperature surpassed 700°C, a reduction in alumina extraction was observed. This decrease was attributed to the reduced interaction between kaolin and hydrochloric acid owing to factors such as evaporation and bubbling in the hydrochloric acid solution. The alumina obtained at the conclusion of the process had a purity level of over 95%, with alumina having a cubic crystal structure (γ-alumina).

Tantawy and Ali Alomari, (2019) investigated acid leaching methods for alumina extraction from Nawan kaolin deposits. The research documented 75 wt% aluminum recovery from kaolin subjected to thermal activation at 850°C for 2 h and leaching conditions of 6 M HCl, 90°C, 3 h, 0.05 g/ml solid/liquid ratio, and 500 rpm. The kaolin sample predominantly comprised quartz, kaolinite, and minor amounts of anatase. Calcination of kaolinite was observed to induce dehydroxylation of the mineral, leading to the formation of amorphous dehydroxylated aluminosilicate phases with no impact on quartz.

Udochukwu et al. (2019) observed that the leaching of clay, referred to as Ibere clay, calcined at 600°C for 60 min, exhibited the most significant leaching response, reaching 50.27% after 1 hour at 100°C and using 1 M HCl. The X-ray diffraction pattern of the optimal clay calcine showed that the distinct peaks of kaolinite were no longer present, suggesting the emergence of an amorphous phase because of the complete dehydroxylation of the clay.

Ogbonnaya et al. (2018) optimized the alumina extraction efficiency of Aku clay and achieved a yield of 78.4% after undergoing calcination at 820°C. The optimal leaching conditions were 67°C, 61 min, 2.2 mol/dm^3 HCl, and 12.9 ml/g liquid to solid ratio. The alumina yield increased with elevated calcination temperature and contact time up to 850°C and 65 min, respectively. However, beyond these optimal conditions, the yield declined. This decrease beyond the optimal calcination

temperature of 850°C and contact time of 65 min is attributed to the complete extraction of alumina and sintering effect at high temperatures.

Ibrahim et al. (2018) achieved optimal extraction efficiency of alumina from kaolin ash, reaching a purity of 79.28%. The calcination temperature significantly influenced the reactivity of kaolin during acid leaching, which is a vital stage in alumina extraction. The proposed combined process for utilizing local kaolin to generate alumina particles included heat treatment at 700°C for 3 h in the presence of sodium chloride, followed by leaching with 40 wt% sulfuric acid and subsequently 120 ml hydrochloric acid. Additionally, other leaching conditions included 140°C, and 3 h 45 min. This initial calcination stage is crucial because it modifies the chemical and physical characteristics of kaolin, rendering it more responsive to acid leaching. The calcination temperature is carefully chosen to ensure the optimal conversion of kaolin into a form that allowed for the maximum extraction of alumina.

Si, Qiao and Yu (2012) highlighted the differences in alumina extraction efficiency between the two types of kaolin and the impact of calcination temperature on their reactivity to acid. The discussion on the extraction of alumina from thermally processed clays was grounded in the observation that the optimal calcination temperatures for both K-JS and K-SX were 600°C, resulting in an alumina extraction of 89.34 wt% from K-JS and 83.37 wt% from K-SX. The leaching conditions were 20wt% HCl, 98°C, 30 min, and mass ratio of solid to acid of 5. It was observed that as the calcination temperature increased, the chemical reactivity of calcined K-JS and K-SX towards the acid diminished. This suggested that thermal treatment at 600°C is the most effective in activating kaolin for alumina extraction through acid leaching.

Al-Zahrani and Abdul-Majid (2009) investigated the alumina extraction from clay using the hydrochloric acid leaching process. The study emphasized the important role of calcination temperature in alumina extraction. Extraction was minimal below 450°C, whereas an active extraction zone existed between 500 and 600°C. At temperatures above 650°C, the appearance of an inert zone was attributed to the complete dehydration of the clay samples at 600°C and the solid-phase

transformation of alumina at higher temperatures. The alumina extraction yields increased from 17.02% to 62.94% between 400 and 600°C with a calcination duration of 60 minutes. The leaching conditions were 3M HCl, boiling conditions, and 10:1 liquid-to-solid weight ratio. However, the extraction yield declined above a calcination temperature of 600°C. This indicates that clay reactivity to acid leaching significantly improves within the optimal temperature range of 500–600°C, beyond which reactivity diminishes due to changes in the chemical and physical properties of the clay.

Various studies have highlighted the critical role of the calcination temperature in altering the chemical and physical properties of kaolin, thereby affecting its reactivity to acid leaching and subsequent alumina extraction. Lower calcination temperatures are associated with incomplete dehydroxylation, which affects the solubility of aluminum. On the other hand, higher calcination temperatures facilitate the conversion of kaolinite to metakaolin, enhancing its reactivity to acid leaching and alumina extraction. While some studies have suggested an optimal calcination temperature of approximately 600-700°C, others indicate variations, with some reporting optimal temperatures at 450°C or even as high as 800°C. These discrepancies suggested a lack of consensus on the precise temperature range that maximizes alumina extraction efficiency. This may be due to differences in mineralogical composition and crystallinity. The optimal calcination temperature range typically falls between 500 and 700°C; beyond this range, the extraction efficiency may decrease due to factors such as complete dehydration of clay samples or changes in the alumina phase, such as the formation of insoluble phases (spinels) and reducing acid solubility. Furthermore, the presence of impurities such as iron oxide phases can significantly influence the calcination behavior and subsequent alumina extraction efficiency. The efficiency of alumina extraction is not only influenced by the calcination temperature, but also by factors such as impurities, contact time, and specific pre-treatment steps. Understanding how different impurities interact with kaolin under varying calcination conditions and the interplay between calcination temperature and clay reactivity is crucial for maximizing alumina extraction efficiency and optimizing the process.

2.7. Summary

This chapter focuses on alumina production, covering various resources, recovery processes, and associated challenges. It reviews research on the impact of calcination temperature on clay responsiveness to acid, highlighting successful alumina recovery using hydrometallurgical techniques. Pretreatment methods such as calcination are typically applied before leaching. While the leaching process is well-researched, this study is distinct in investigating the leaching of South African kaolinitic clays. This focus allows for evaluating local mineral compositions and their effect on process efficiency and selectivity, which has not been thoroughly explored. The goal is to assess the feasibility of applying this established process to region-specific material.

Chapter 3 Materials and Methods

3.1 Introduction

The laboratory work consisted of three parts which are (1) Chemical and physical characterization of raw clays, (2) calcination of ball, fire, and flint clays, and (3) hydrochloric acid leaching of aluminum and impurities such as calcium, iron, potassium, magnesium, titanium, and silicon species.

3.2. Materials

a) A sample of Ball clay from Musina, Limpopo province
b) A sample of Fire clay from Thohoyandou, Limpopo province
c) A sample of Flint clay from Hammanskraal Pretoria
d) AR 32% hydrochloric acid from Minema Chemical (Pty) Ltd
e) Distilled water from CSIR Pretoria campus

Table 3.1 shows the characteristics of the three types of clays used in the study.

Table 3.1: Characteristics of kaolinitic clays (Bergaya et al., 2006)

	Origin	Main clay mineral constituents	Remarks
Ball (BL) clay	Sedimentary	Kaolinite	Highly plastic, white burning
Flint (FL) clay	Sedimentary with subsequent diagenesis	Kaolinite	Not, plastic, non-slaking, used for refractories
Fire (F) clay	Sedimentary	Kaolinite	Plastic, high refractoriness

3.3. Characterization

The clays were crushed and milled by Suntech Geomet Laboratories. X-ray fluorescence (XRF) and inductively coupled plasma atomic optical emission spectrometry (ICP-OES) were used to analyze the chemical composition of the raw clay, calcined clay, and leached solids (residue). X-ray diffraction (XRD) was used to identify the mineral phases in the raw clay, calcined clay, and leached solids. Particle size analysis of the raw clay samples was performed using laser diffraction spectroscopy. Differential thermal analysis (DTA)–thermal gravimetric analysis (TGA) (DTA-TGA) was used to analyze the thermal decomposition of the raw clays. Fourier transform infrared spectroscopy (FTIR) was used to analyze the functional molecular groups present in the clay minerals. Inductively coupled plasma atomic optical emission spectrometry (ICP-OES) was used to analyze the elements present in the leachates and some elements present in the wash water (water that was used to wash the leached solids to neutral pH). Inductively coupled plasma atomic mass spectrometry (ICP-MS) was used to analyze most of the elements in the wash water.

3.3.1. Analytical techniques

3.3.1.1. X-ray diffraction analysis

The mineralogical compositions of the raw and calcined clays and the leached residue were determined by XRD analysis and Consulting cc. Raw clay samples were prepared for XRD analysis using a backloading preparation method. Diffractograms were obtained using a Malvern Panalytical Aeris diffractometer with a PIXcel detector and fixed slits with Fe-filtered Co-Kα radiation (40.0 kV, 7.5 mA, λ= 1.789 Å). The phases were identified using the X'Pert Highscore Plus software. The relative phase amounts (wt%) were estimated using the Rietveld method. For the calcined clay and leached residue, the material was scanned after

the addition of 20% Si to quantitatively determine the amorphous content and micronization using a McCrone micronizing mill.

3.3.1.2. X-ray fluorescence

The XRF chemical compositions of the raw, calcined, and leached residues were determined by an accredited laboratory UIS Analytical Services (Pty) Ltd.

3.3.1.3. Fourier transform infrared spectroscopy

The functional molecular groups in FTIR spectroscopy were determined at CSIR Centre for Nanostructures and Advanced Materials, Material characterisation, testing and Analytical Facility. Fourier transform infrared (FTIR) spectroscopy was used to analyze the samples in the transmission mode. A Perkin Elmer Spectrum 100 spectrometer was used to characterize the spectra of each sample. In all the cases, the spectral resolution was maintained at 16 cm^{-1}. The FTIR Spectra of samples were obtained in the range of 550 – 4000 cm^{-1}.

3.3.1.4. Differential thermal - thermal gravimetric spectroscopy

The thermal behavior of the raw clays was determined using TGA/DTA at the CSIR Centre for Nanostructures and Advanced Materials, Material characterisation, testing, and Analytical Facility. The TGA/DTA was conducted in air (nitrogen) testing environment with a temperature profile from room temperature to 1000 °C and at a heating rate of 10°C/min.

3.3.1.5. Inductively coupled plasma atomic (ICP) optical emission spectrometry (OES) and mass spectrometry (MS)

The ICP-OES and ICP-MS element concentrations of raw and calcined clays, leachates, wash water and leached residue were determined by an accredited laboratory, UIS Analytical Services (Pty) Ltd.

3.4 Methodology

3.4.1. Calcination of raw clays

Raw clay samples were weighed to approximately 120 g in porcelain crucibles. The clay samples were calcined at 600, 650, 700, 750, and 800 °C in a furnace. The samples were calcined at various temperatures between 600 and 800°C with constant calcination time of 8 hours and 10°C min^{-1} heating rate. Subsequently, the samples were allowed to cool to room temperature in a furnace and stored for use in acid leaching experiments and analytical studies. Calcination temperature ranges were selected from the literature to produce anhydrous and amorphous clay structures (Udochukwu, *et al.*, 2019b; Kassa, Shibeshi and Tizazu, 2022; Xue *et al.*, 2023).

3.4.2. Acid leaching of calcined clays

Part 1 leaching experiments involved investigating the effect of Calcination temperature on the Al recovery of the calcined clays. Duplicate leaching experiments were performed. A calcined clay sample of approximately 10 g was weighed and a 3 M HCl acid solution of approximately 100 ml was prepared using 32% AR hydrochloric acid and distilled water. A 3 M HCl concentration has been widely used in similar research (Al-Zahrani and Abdul-Majid, 2009; Ajemba and Onukwuli, 2012b; Aly *et al.*, 2019; Orugba *et al.*, 2020), making it a well-established choice for comparison and optimization. The HCl solution was then poured slowly into a 500 ml 3-neck bottomed flask. The reaction flask was fitted with a reflux condenser, thermometer, and stopper, and placed inside an oil bath, as shown in Figure 3.1. The leaching conditions were selected based on combination of previous literature (Daniels *et al.*, 2012; Ogbonnaya *et al.*, 2018; Tantawy and Alomari, 2019; Aly *et al.*, 2019; Okwuzu *et al.*, 2022). The acid solution was heated to a fixed temperature of 70 °C, and then calcined clay was added. The reaction mixture was stirred at 250 rpm for 4 h, and the temperature was maintained at 70 °C.

The main reaction desired to achieve Al extraction is shown in Equation 3.1. After the reaction time elapsed, the mixture was cooled to room temperature. The reaction mixture was centrifuged and decanted to separate the liquid from the solids. The element concentrations in the leachate were determined using ICP-OES. The leached solids were washed with distilled water to a pH of approximately 7 and then dried overnight in an oven. The element concentrations in the wash water were determined using ICP-MS.

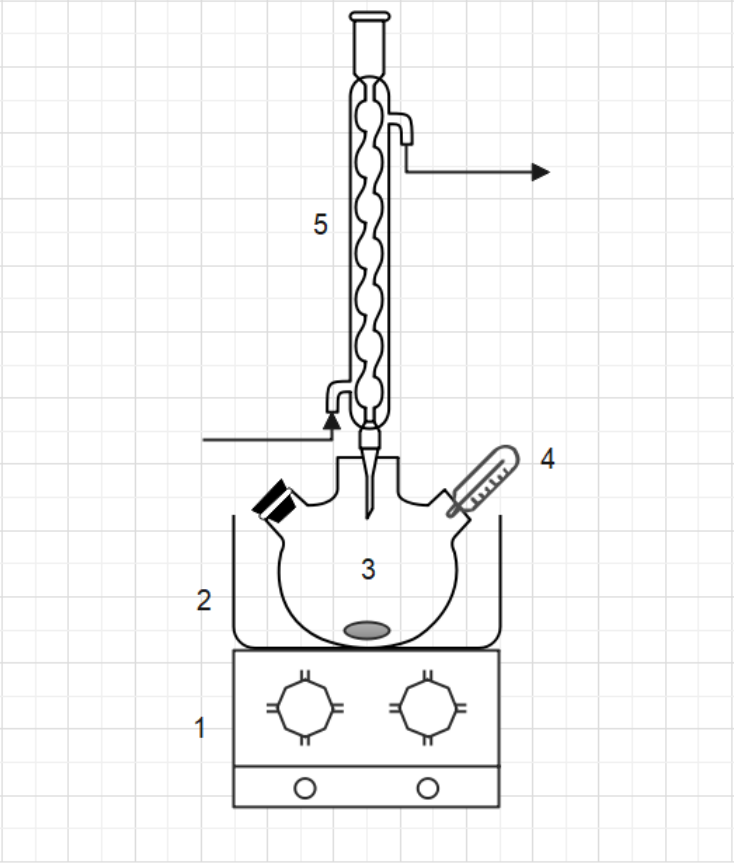

Figure 3.1 Leaching experiment setup: (1) Magnetic hotplate stirrer; (2) Oil bath; (3) 3-neck glass flask; (4) thermometer; (5) glass condenser.

$$Al_2O_{3(s)} + 6HCl_{(soln)} \rightarrow 2AlCl_{3(soln)} + 3H_2O_{(l)} \qquad 3.1$$

Part 2 leaching experiments followed the methodology in part 1 leaching experiments, however, leaching variables were varied to perform statistical studies.

Statistical studies were performed to investigate the leaching variables, such as acid concentration, temperature, time, and solid–liquid ratio, employing the 2^4 full factorial design of experiment and Design Expect software (version 13). The actual and coded levels of each factor are shown in Table 3.2.

Table 3.2: Design matrix of 2^4 level full factorial design

Independent variables	Symbols	Range and levels	
		-1	+1
Acid concentration (M)	A	3	5
Leaching temperature (°C)	B	50	90
Leaching time (min)	C	2	4
Solid-liquid ratio (g/ml)	D	0.05	0.15

Chapter 4 Material Characterization

4.1. Introduction

Leaching experiments were performed to determine the impact of calcination conditions, particularly calcination temperature, on the conversion of clays to the amorphous metakaolinite phase, as described in Chapter 3. Through these experiments, it was noted that a change in calcination temperature resulted in the formation of an amorphous metakaolinite phase and other new phases. The thermal dehydroxylation of kaolinite has been studied in previous years (Johnston *et al.*, 2022a; Kassa et al., 2022; Ptáček *et al.*, 2014; Ortega, MacÍas and Gotor, 2010; Gasparini *et al.*, 2013; Ortega et al, 2010; Lu et al, 2020; Ramadji *et al.*, 2022; Stevenson and Gurnick, 2016; Sperinck *et al.*, 2011; Mark *et al.*, 2019b; Hanein *et al.*, 2022); however, there is no general agreement on the structural arrangement of the dehydroxylated form of metakaolinite. Although considerable attention has been paid to high-temperature phases, metastasis is frequently neglected owing to its non-crystalline characteristics, resulting in limited conclusive structural data.

The focus of this section is to evaluate the relationship between the calcination temperature and the amorphous content detected in the semi-quantitative XRD analysis after calcination of the clays, and to observe the phase transformation in the clays. The chemical composition of the calcined clays, thermal behavior (TGA/DSC), and FTIR spectra were also examined.

4.2. Characterization of raw clays

Raw clay samples were prepared and analyzed using XRD, XRF, FTIR, and TGA/DTA techniques.

4.2.1. Qualitative XRD characterization of raw clay samples

The XRD pattern of the raw BL clay obtained after crushing and milling is shown in **Error! Reference source not found.**. The crystalline structure of raw BL clay was evident from the distinct peaks, which were predominantly composed of kaolinite and quartz. The prominent peaks observed at 14.3°2θ and 29°2θ correspond to kaolinite. Moreover, these peaks indicate basal spacing between the layers of the mineral (Barton and Karanthanasis, 2005). The presence of kaolinite was further confirmed by the observation of additional strong peaks at 23°2θ, 24.5°2θ, 26°2θ, and 27°2θ, which are consistent with the layered nature of the kaolinite structure. Furthermore, the peaks in the range of 40°2θ–50°2θ also indicated the presence of kaolinite.

Another sharp peak was observed at 23.9°2θ and 31°2θ corresponding to the presence of crystalline quartz within the BL clay. The ill-defined peak at 29.9 °2θ was observed to correspond to anatase. The presence of muscovite within the clay was confirmed by the poorly defined peaks at 10°2θ, 22.9°2θ and 28.5°2θ. It was not possible to observe fingerprints of the Fe-containing phases in the diffraction pattern of the raw BL clay. A broad hump in the lower angle range (< 10°2θ) may represent poorly crystalline clay components (Smith and Horgan 2018). Kaolinite with a definite and structured arrangement displays sharp and narrow peaks, whereas kaolinite with a disordered structure exhibits less defined, broader, and asymmetrical peaks in XRD patterns (Vaculíková *et al.*, 2011). The sharp XRD patterns indicate that the samples had more crystalline structures (Pepper *et al.*, 2021).

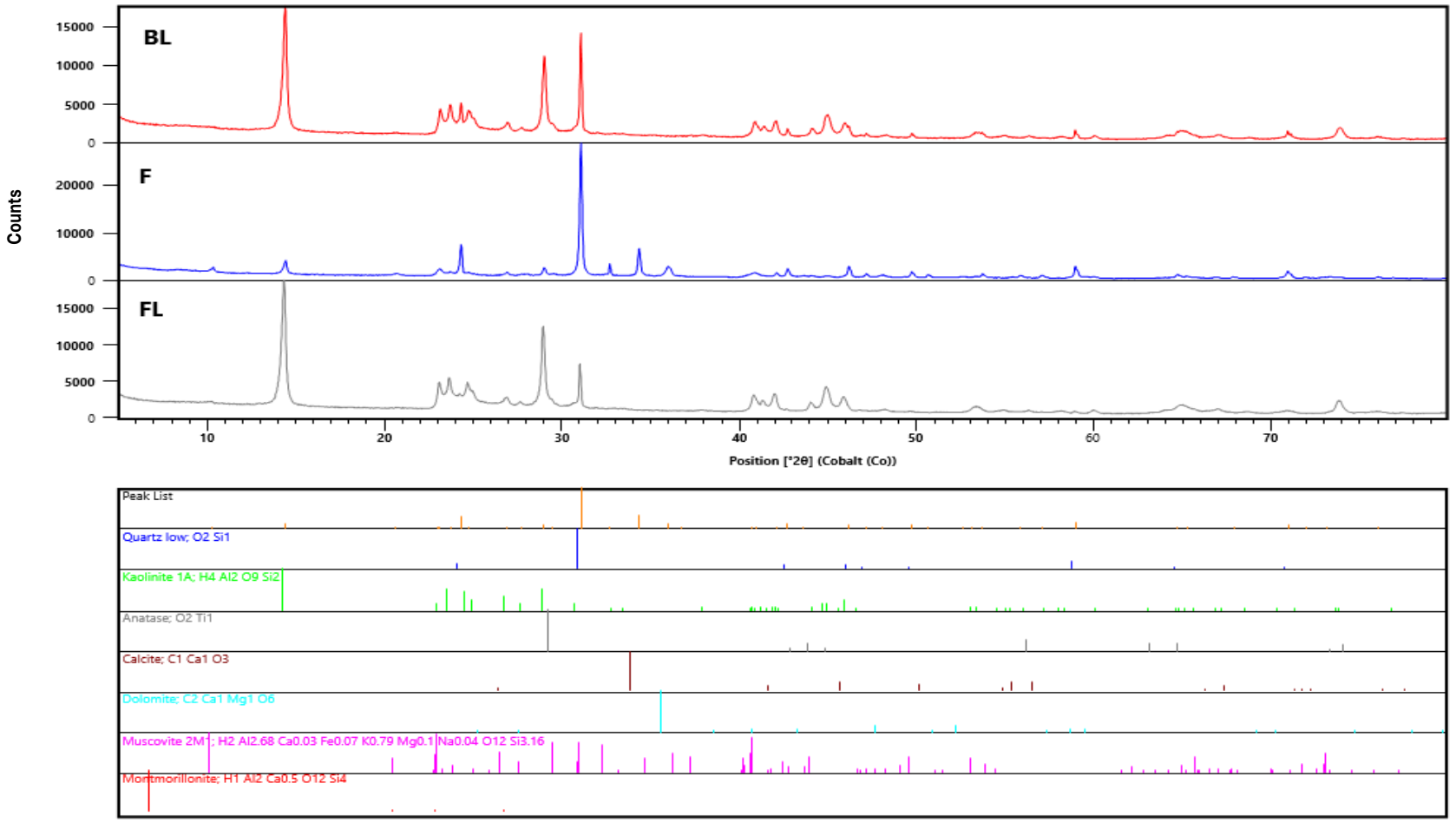

Figure 4.1: X-ray diffraction pattern for raw BL, F, and FL clays

The XRD analysis of the FL clay sample (Figure 4.1) showed that the clay had a diverse mineralogical composition, encompassing kaolinite, quartz, muscovite, anatase, and dolomite. The distinctive peaks at 14.3°2θ, 23°2θ, 23.7°2θ, 25°2θ and 29°2θ emphasized the presence of kaolinite layers within the clay. Additionally, the peaks in the range 40°2θ - 50 °2θ indicated the presence of kaolinite. The sharp peaks at 23.7 °2θ and 31°2θ indicate the crystalline nature of quartz in the clay. The ill-defined peaks at 10.3°2θ and 22.9°2θ confirmed the presence of muscovite in the sample. An unclear peak was observed at 29.5°2θ corresponding to anatase in the clay, and the peak at 35.5°2θ corresponded to dolomite, indicating the presence of this carbonate mineral as a minor component in the clay. Variations in the peak intensity provided insight into the relative abundance of each mineral phase; the intensity of kaolinite was dominant, followed by quartz, muscovite, and trace phases of anatase and dolomite. Additionally, a broad hump in the lower-angle range (<10°2θ) was observed, indicating poorly crystalline components.

The F clay sample exhibited a diverse mineralogical composition comprising several mineral phases, as shown in **Error! Reference source not found.**. The sharp peak at 31.8°2θ indicated the presence of crystalline quartz in the clay. The prominent peaks at 15°2θ, 23.9°2θ and 24.9°2θ represented kaolinite in the clay. The peak intensities of kaolinite in F clay were extremely low, suggesting low kaolinite content. The peaks at 33.3°2θ, 41.5°2θ,45.5°2θ,50°2θ and in the range of 54°2θ to 57°2θ corresponded to the calcite present in the clay. Additional peaks around 35°2θ, 46.9°2θ and 51.3°2θ represented dolomite. The coexistence of dolomite and calcite was observed in the sample. Carbonate minerals, such as calcite and dolomite, have cationic sites in their crystal structure that can accommodate various foreign cations, such as Fe, Mn, Sr, Ba, and Zn, through isomorphic substitution (Debure *et al.*, 2021). This process involves substituting one structural cation with another that shares a similar structure (Barton and Karanthanasis, 2005). The efficiency of the extraction process can be affected by these minerals because they may react with acids during leaching and consume acid, which affects the overall process efficiency.

Well-defined peaks at 10.9°2θ and 23.5°2θ indicated the presence of muscovite. A weak peak at 29.9°2θ suggested the presence of anatase, which contributes to the overall mineral diversity in clay. The broad peaks at lower angles (<8°2θ) suggested the presence of smectite. The elevated background around 6.5 °2θ in the F clay confirms the presence of montmorillonite/smectite (Hollanders, 2017). The location of the montmorillonite peak could be associated with prevalent exchangeable cations. The wide diffraction peak at 6.5°2θ is characteristic of Ca-rich montmorillonite, whereas Na-rich montmorillonite typically appears at a higher 2θ angle (Hollanders, 2017).

Overall, the point of difference between the BL, F, and FL clays was the peak intensity. The XRD patterns of the raw clays in **Error! Reference source not found.** revealed that the BL and FL clays exhibited two prominent reflection peaks of kaolinite, which suggests that they are rich in kaolinite. In contrast, the peak intensity of kaolinite in the F clay was extremely low, indicating a relatively low kaolinite content compared to the BL and FL clays.

4.2.2. Mineralogical composition of raw clay samples

The findings of the semi-quantitative XRD analysis of the relative mineral content in the raw clays are presented in Table 4.1. According to the results, kaolinite was the most prevalent mineral phase in both raw BL and FL clays, accounting for 82.4 wt% and 91.1 wt% of the total mineral content, respectively. These findings were consistent with the XRD patterns of the raw clays. The kaolinite levels were found to have a noticeable impact on clay dehydroxylation, which allowed for a useful comparison between low and high kaolinite contents. Furthermore, this study examined whether kaolinite content has a significant influence on the reactivity of clays.

Another distinction between F clay and other clays lies in its elevated mineral impurity content, as demostrated by the XRD data presented in Table 4.1. The F clay contained 44.7 wt% quartz, 7.5 wt% calcite, 17.4 wt% dolomite, 8.1 wt%

muscovite, 5.5 wt% smectite and 0.3 wt% anatase. In comparison, the BL clay contained 14.3 wt% quartz, 2.6 wt% muscovite and 0.6 wt% anatase and FL clay contained 6.6 wt% quartz, 1.7 wt% muscovite and trace minerals of 0.6 wt% anatase and 0.1 wt% dolomite.

Table 4.1: Mineralogical composition of raw BL, F and FL clays

(wt%)	Quartz	Kaolinite	Anatase	Calcite	Dolomite	Muscovite	Smectite
BL clay	14.3	82.4	0.6	0	0	2.6	0
F clay	44.7	16.5	0.3	7.5	17.4	8.1	5.5
FL clay	6.6	91.1	0.6	0	0.1	1.7	0

The order of muscovite content from highest to lowest was F >BL > FL. Barton and Karanthanasis (2005) described muscovite as a type of dioctahedral mica that contains Al^{3+} in the octahedral sheet and K^{+} in the interlayer. The clay fraction frequently contains mica with diminished crystallinity, fewer K^{+} ions, elevated water content, and the possibility of substitutions involving Fe^{2+} and Fe^{3+} in the octahedral sheets, along with Ca^{2+} in the interlayer (Barton and Karanthanasis, 2005).

4.2.3. Chemical composition of raw clay samples

Error! Reference source not found. depicts the chemical composition of the raw BL clay sample. The data revealed the predominance of Al_2O_3 (33.8 wt%) and SiO_2 (50.4 wt%) in the sample. The Al_2O_3 may be primarily associated with kaolinite and muscovite clay minerals, as seen in the XRD patterns (**Error! Reference source not found.**). Silica was present in kaolinite and muscovite, and is associated with the quartz phase (Ibrahim *et al.*, 2018). The small amount of K_2O in the chemical analysis suggested the presence of muscovite clay mineral. The presence of iron can be observed in a phase that is separate from kaolinite, or it can be found adsorbed on its surface as colloidal iron in the form of limonite (FeOOH), hematite

(Fe_2O_3), or ferric hydroxide ($Fe(OH)_3$) (Orosco *et al.*, 2014; Ibrahim *et al.*, 2018). However, clay minerals associated with Fe were not detected in XRD analysis.

Table 4.2: Chemical composition of raw BL, F, and FL clays

	Chemical composition (%)								
	Fe_2O_3	SiO_2	Al_2O_3	K_2O	CaO	MgO	TiO_2	Other	LOI
BL	0.706	50.4	33.8	0.417	0.5	0.212	1.44	0.6	12.6
F	2.24	54.6	12.8	1.88	10.0	2.96	0.575	0.4	14.2
FL	0.524	46.8	36.9	0.473	0.064	0.118	1.23	0.306	13.5

Raw FL clay is distinguished by a high kaolinite content and a low level of impurities, such as quartz and muscovite, with only traces of anatase and dolomite (Table 4.1). The chemical composition of raw FL clay (Table 4.2) shows 46.8 wt% SiO_2 and 36.9 wt% Al_2O_3, along with minor amounts of Fe_2O_3, K_2O, CaO, MgO, TiO_2, and traces of P_2O_5, Mn_3O_4, Na_2O, V_2O_5, BaO, Cr_2O_3, SrO, ZrO_2, MnO, and SO_3 (other). The presence of dolomite in the sample was indicated by the small amounts of CaO and MgO.

Raw F clay had a relatively low amount of kaolinite, with significant quantities of quartz, dolomite, calcite, muscovite, smectite, and traces of anatase (Table 4.1). Consequently, the chemical composition of the raw F clay (Table 4.2) exhibited a high silica content (SiO_2 at 54.6% wt), low alumina content (Al_2O_3 at 12.8% wt), and low lime content (CaO at 10.0% wt). Other minor oxides detected included Fe_2O_3, K_2O, MgO, and TiO_2, while trace amounts of P_2O_5, Mn_3O_4, Na_2O, V_2O_5, BaO, Cr_2O_3, SrO, ZrO_2, MnO, and SO_3 (other) were also present. The significant K_2O content suggested the presence of illite (Khalifa *et al.*, 2019), whereas the high CaO and MgO contents are linked to the abundance of carbonates (calcite and dolomite), which explains the high loss of ignition observed (Trindade *et al.*, 2009).

The Al_2O_3/SiO_2 ratio indicates kaolinite purity; the higher the ratio, the more kaolinite exists within clay (Chin *et al.*, 2017). The Al_2O_3/SiO_2 ratio of raw BL and FL clay were 0.67 and 0.79, respectively, confirming the high amount of kaolinite seen in the semi-quantitative XRD analysis results (Table 4.1). Meanwhile, the Al_2O_3/SiO_2 ratio of the raw F clay was 0.23, indicating a lower amount of kaolinite.

The SiO_2/Al_2O_3 ratio indicate the level of quartz content in the clays (Chin *et al.*, 2017). The SiO_2/Al_2O_3 ratio of raw BL and FL clay were 1.47 and 1.27, respectively, indicating a low amount of quartz compared to raw F clay with the SiO_2/Al_2O_3 ratio of 4.27. The SiO_2/Al_2O_3 ratio of the F clay was higher than the theoretical molar ratio of kaolinite (2.00), suggesting the presence of quartz and other silicates in the sample (Schackow *et al.*, 2020). This observation confirmed the amount of quartz in the semi-quantitative XRD results presented in Table 4.1. Compared to kaolinite-rich clays, the alumina content of smectic clays is generally low (Hollanders, 2017).

The comparatively low concentration of Na_2O relative to CaO in the F clay suggests that calcium is the predominant exchangeable cation in the smectite (Hollanders, 2017). The BL, F, and FL clays contained 0.706%, 2.239%, and 0.524% iron oxide minerals, respectively. Meanwhile, the BL, F, and FL clays contained 1.440%, 0.575%, and 1.234% titanium oxide minerals, respectively. Notably, the clays with high alumina content had lower content of iron oxide and higher titanium oxide content than the F clay, which had higher content of iron oxide and lower titanium oxide content. Correspondingly, F clay had a higher impurity content than the BL and FL clays. Loss of ignition can be used to indicate kaolinite purity (Chin *et al.*, 2017). The loss of ignition for the BL, F, and FL clays were 12.6%, 14.2%, and 13.5%, respectively. Ideal kaolinite consists of 13.96% of LOI (Schackow *et al.*, 2020), thereby indicating that FL clay is highly kaolinitic with LOI of 13.5%. This further supported the mineralogical composition presented in Table 4.1.

The chemical compositions of the raw clays revealed varying levels of other oxides, suggesting the presence of impurities. The process of incorporating iron and potassium into clays typically involves the isomorphous substitution of Fe^{3+} and K^+ cations within the octahedral layers of the clay mineral structures, as suggested by Escalera et al. (2012). This process typically takes place in mica structures, leading to an increased interlayer spacing in mica relative to kaolinite structures (Escalera *et al.*, 2012). The relatively high amount of Fe_2O_3 could be due to illite or muscovite and montmorillonite or smectite in the F clay, as identified in XRD (Figure *4.1*).

4.2.4. Thermal analysis of the clay samples

Thermal analysis is an effective method for comprehending the various phase transitions that occur in clay structures due to temperature changes (Ramadji *et al.*, 2022). The DTA curves obtained from a kaolinite sample during heating demonstrate both endothermic and exothermic reactions, including surface water desorption, structural OH^- groups dehydroxylation, and mullite and cristobalite transformation (Vaculíková *et al.*, 2011; Diko *et al.*, 2015). To select the appropriate calcination temperature range for the raw clays, thermal analysis and information from the literature were considered. The range of 600-800°C was chosen for the experiments, which encompasses the observed tail within the mass loss seen in the TGA and is ascribed to metakaolinite forming, as well as an enhancement in heat transmission to the furnace-heated sample during steady heating (Pepper *et al.*, 2021).

The TGA curve in Figure *4.2* shows three well-defined regions of weight loss for BL clay. The first region emerged below 200°C, whereas the second region appeared above 300°C, and third region emerged above 800 °C. The first endothermic peak observed in the DTA curve occurs at 119.81°C, which is indicative of the initial water desorption enthalpy associated with the elimination of water adsorbed on the surface of kaolinite (Kassa, Shibeshi, Tizazu, *et al.*, 2022). The second endothermic peak in the DTA curve appears at 500.73°C, corresponding to the second TGA region with a weight loss of 11.40%. This peak is thought to represent kaolinite dehydroxylation enthalpy, which is attributed to the loss of kaolinite structural water (Kassa, Shibeshi, Tizazu, *et al.*, 2022). The dehydroxylation process transforms kaolinite into an amorphous metakaolinite phase that is more reactive. The transformation of kaolinite occurred at 330 °C to 700°C. The third endothermic peak was observed in the DTA curve at 874.77 °C assigned to the formation of aluminum spinels in the clay due to the initial Fe ions migration into the metakaolinite structure (Johnston *et al.*, 2022a).

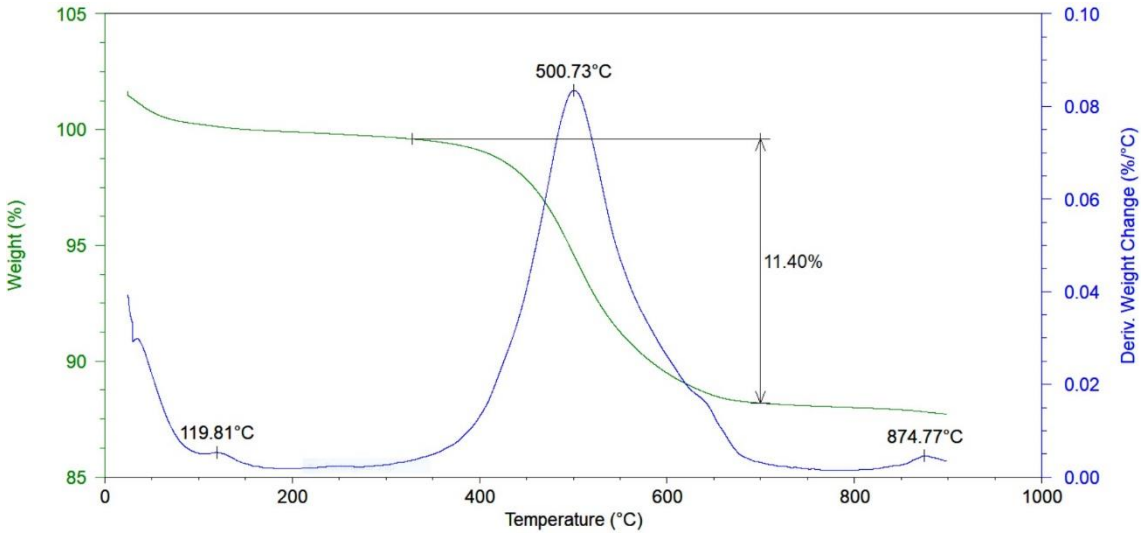

Figure 4.2: Thermograms of raw BL clay

The TGA curve for the FL clay (Figure *4.3*) shows a well-defined weight loss between 330 °C and 700°C. The DTA curve revealed an endothermic peak at 506.43°C, which corresponded to a weight loss of 12.67%, suggesting the dehydroxylation enthalpy of kaolinite (Obada *et al.*, 2017).

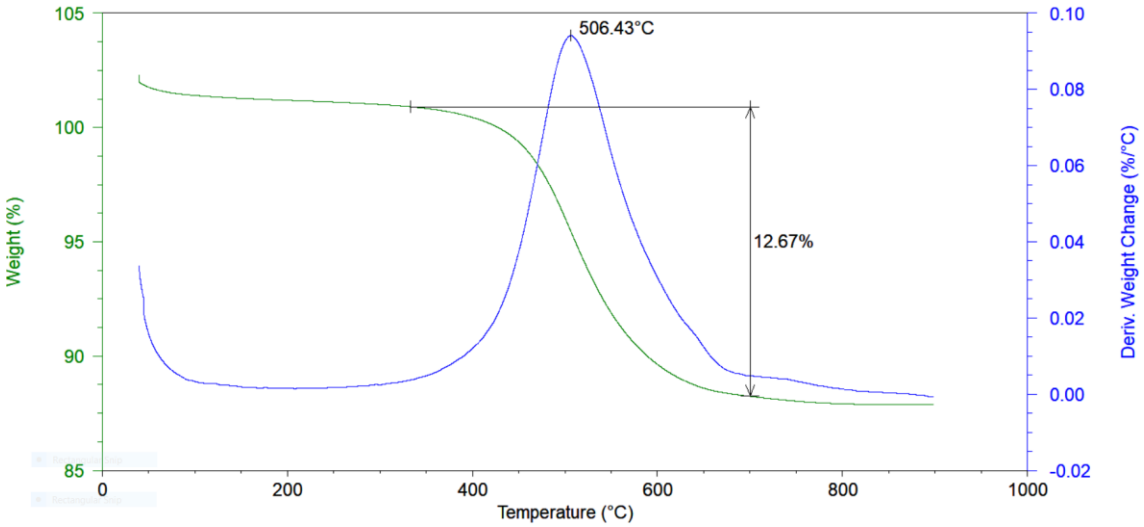

Figure 4.3: Thermograms of raw FL clay

Figure *4.4* displays three distinct regions of weight loss for the F clay. The first region was visible below 300°C, the second region appeared above 390°C, and the

third region was located between 540 and 740 °C. The first endothermic peak in the DTA curve was observed at 270.29°C, which corresponded to the first TGA region and indicated the enthalpy associated with the initial desorption of surface water (Kassa, Shibeshi, Tizazu, *et al.*, 2022). The second endothermic peak in the DTA curve occurs at 504.02°C and corresponds to a weight loss of 2.17%, indicating the enthalpy associated with the dehydroxylation of kaolinite (Kassa, Shibeshi, Tizazu, *et al.*, 2022). The transformation of kaolinite occurred at 390°C to 540°C. The third endothermic peak in the DTA curve was observed at 699.05°C and corresponded to the third TGA region, with a weight loss of 10.67%, indicating the enthalpy associated with the decomposition of calcite (Zunino *et al.*, 2020).

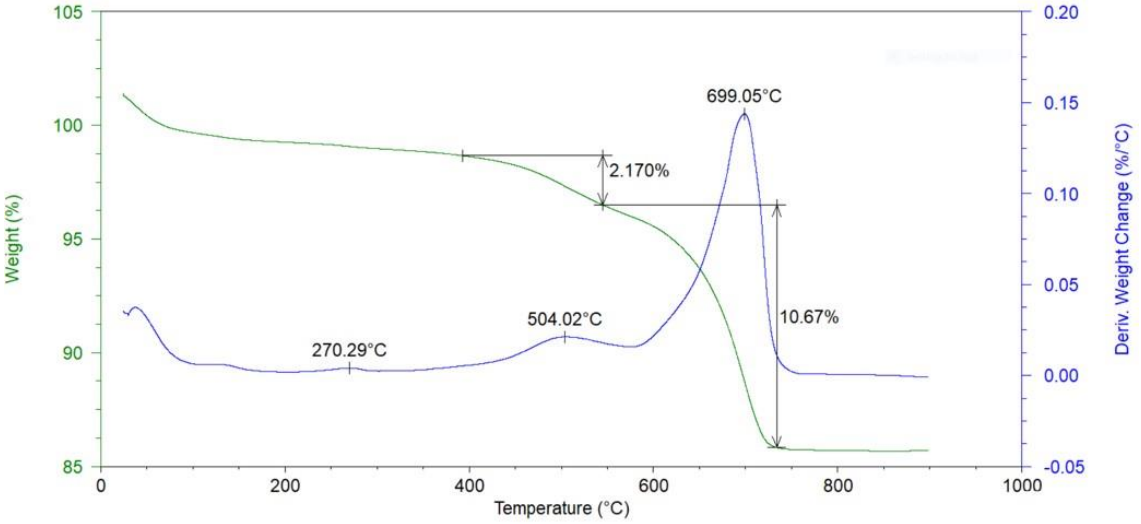

Figure 4.4: Thermograms for raw F clay

Dehydroxylation temperatures below 570 °C are typically associated with disordered kaolinite (Ortega *et al.*, 2010). Disordered kaolinite undergoes dehydroxylation at lower temperatures than well-ordered kaolinite, as demonstrated by the thermal behavior of BL, FL, and F clay, which indicated that dehydroxylation occurred below 570°C (Izadifar *et al.*, 2020). The metakaolinite formed is not a straightforward mixture of amorphous silica and alumina; rather, it is a complex amorphous structure that exhibits some degree of order because of its the hexagonal stacking layers (Schackow *et al.*, 2020).

4.3. Mineral and structural transformation of clays

The raw clay samples underwent thermal treatment via calcination at 600 °C, 650 °C, 700 °C, 750 °C, and 800 °C. Prior research (Si, Qiao and Yu, 2012; Johnston *et al.*, 2022;Kassa et al, 2022; Nnanwube and Onukwuli, 2023; Al-ajeel and Al-sindy, 2006; ElDeeb *et al.*, 2019) has illustrated that the recovery of aluminum from metakaolinite is significantly higher than that from natural kaolinitic clay. Pepper *et al.* (2021) proposed that this difference in reactivity is attributed to the modifications to the structure during the formation of metakaolinite, which results in the transformation of the alumina geometry within metakaolinite. Furthermore, Barry *et al.* (2019) reported that when thermally activated above 550°C, clays undergo a transformation into an amorphous metakaolinite phase, which is accompanied by the loss of OH structural groups. During this process, the arrangement of silicon and aluminum atoms is rearranged, and the number of octahedral sheets of aluminum decreases. Additionally, tetra-, and penta-coordinated aluminum appears. This new geometry is proposed to predominantly involve Al coordinated in tetrahedral formations, a factor contributing to the enhanced reactivity of metakaolinite in acidic conditions, as noted by Pepper *et al.* (2021). Therefore, to explore the potential for mineral transformation and structural changes that occur during calcination, the outcomes of XRD and FTIR analyses were carefully studied.

4.3.1. XRD characterization of calcined clays

Figure 4.5 shows the XRD peak patterns of the calcined BL clays obtained between 600 and 800 °C. The peak patterns in this temperature range were very similar. The dominant sharp and well-defined peaks observed at 31°2θ, 33.2°2θ, 55.5 °2θ, and 66.5°2θ corresponded to quartz. The kaolinite characteristics observed in the raw BL clay in **Error! Reference source not found.** were notably absent. This includes the peaks at 14.3°2θ, 29°2θ, 23°2θ, 24.5°2θ, 26 °2θ, 27°2θ and the peak range 40°2θ-50°2θ. Moreover, the disappearance of these peaks implied that kaolinite was transformed into an amorphous metakaolinite phase during calcination (Poo-arporn

et al., 2020). The thermal behavior (Figure *4.2*) of the BL clay indicated that the dehydroxylation of kaolinite occurred between 330 °C and 700 °C, as evidenced by the disappearance of kaolinite peaks at all calcination temperatures. The muscovite peaks decreased slightly as the calcination temperature increased, indicating a gradual dehydroxylation process.

Clay minerals with lower crystallinity undergo dehydroxylation at temperatures that are lower and cover a broader range than those with higher crystallinity. This difference is linked to the distribution of bond energies associated with the hydroxyl groups. Hanein *et al.* (2022) reported that as the temperature for calcination increases from 600°C, which results in 95% dehydroxylation, to 800°C, which leads to complete dehydroxylation, notable changes can be observed in the coordination of Al and Si within the crystal lattice of the calcined clay. The implication is that even though most of the dehydroxylation has been completed, structural irregularities may continue to exist. Nevertheless, there is no complete loss of crystalline order in the structure. Instead, there is a structural disorder that is linked to the disturbance of the lattice pattern that runs perpendicular to the layers of the structure (Hanein *et al.*, 2022).

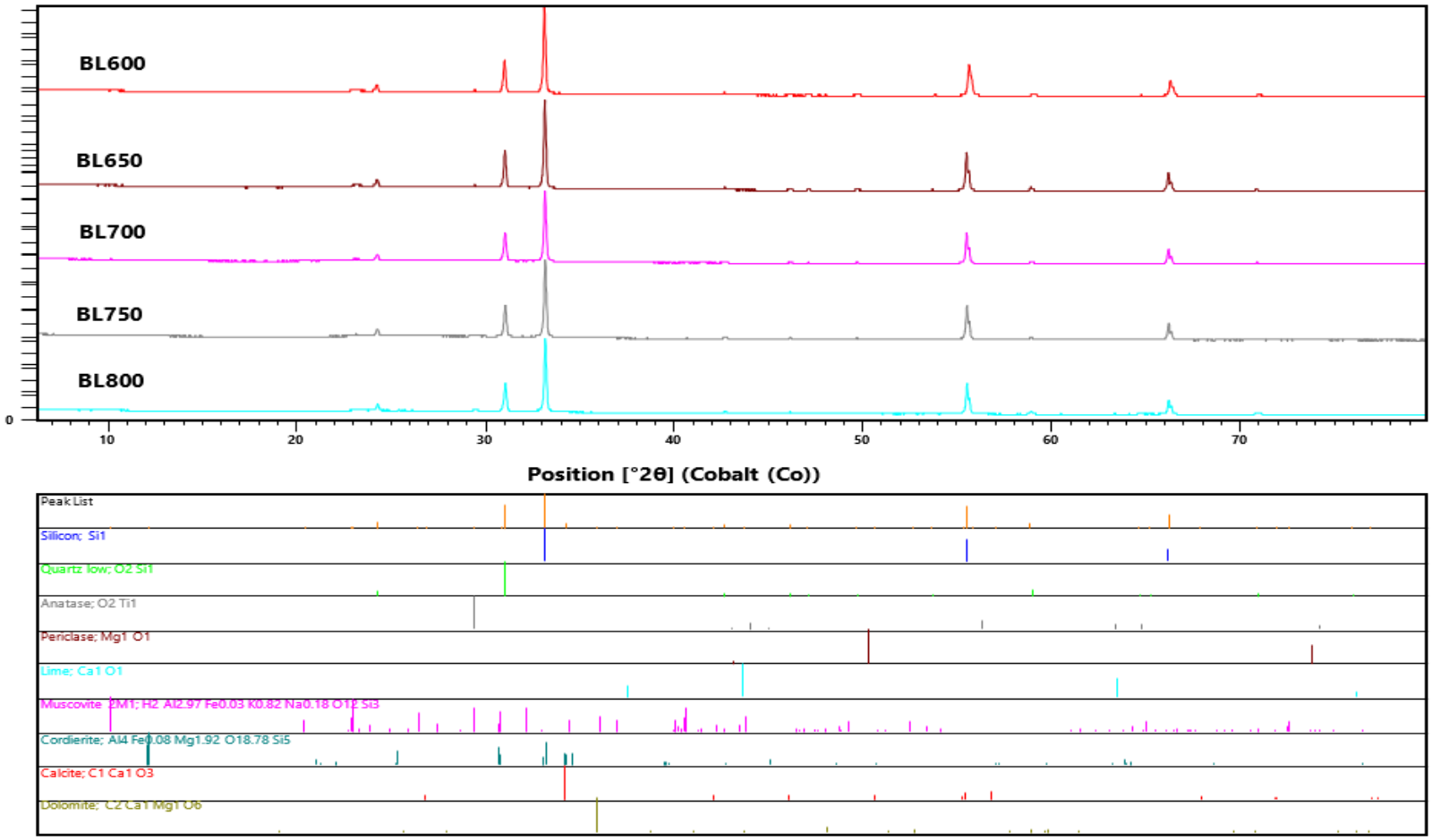

Figure 4.5: X-ray diffraction patterns of calcined BL clay

Similar peak patterns between 600 and 800 °C were observed in the XRD peak patterns of the calcined FL clay (Figure 4.6). The sharp peaks at 31°2θ, 33.2 °2θ, 55.5°2θ and 66.5°2θ indicated the dominant presence of quartz after calcination. Meanwhile, the peaks corresponding to kaolinite at 14.3°2θ, 23°2θ,23.7°2θ, 25°2θ, 29°2θ and the range of 40°2θ-50°2θ in the raw FL clay (Figure *4.1*) disappeared, indicating that kaolinite was completely transformed. This result confirmed the thermal behavior analysis of the FL clay (Figure *4.3*), which demonstrated that the disappearance of kaolinite peaks with dehydroxylation was expected to occur between 330 and 700 °C.

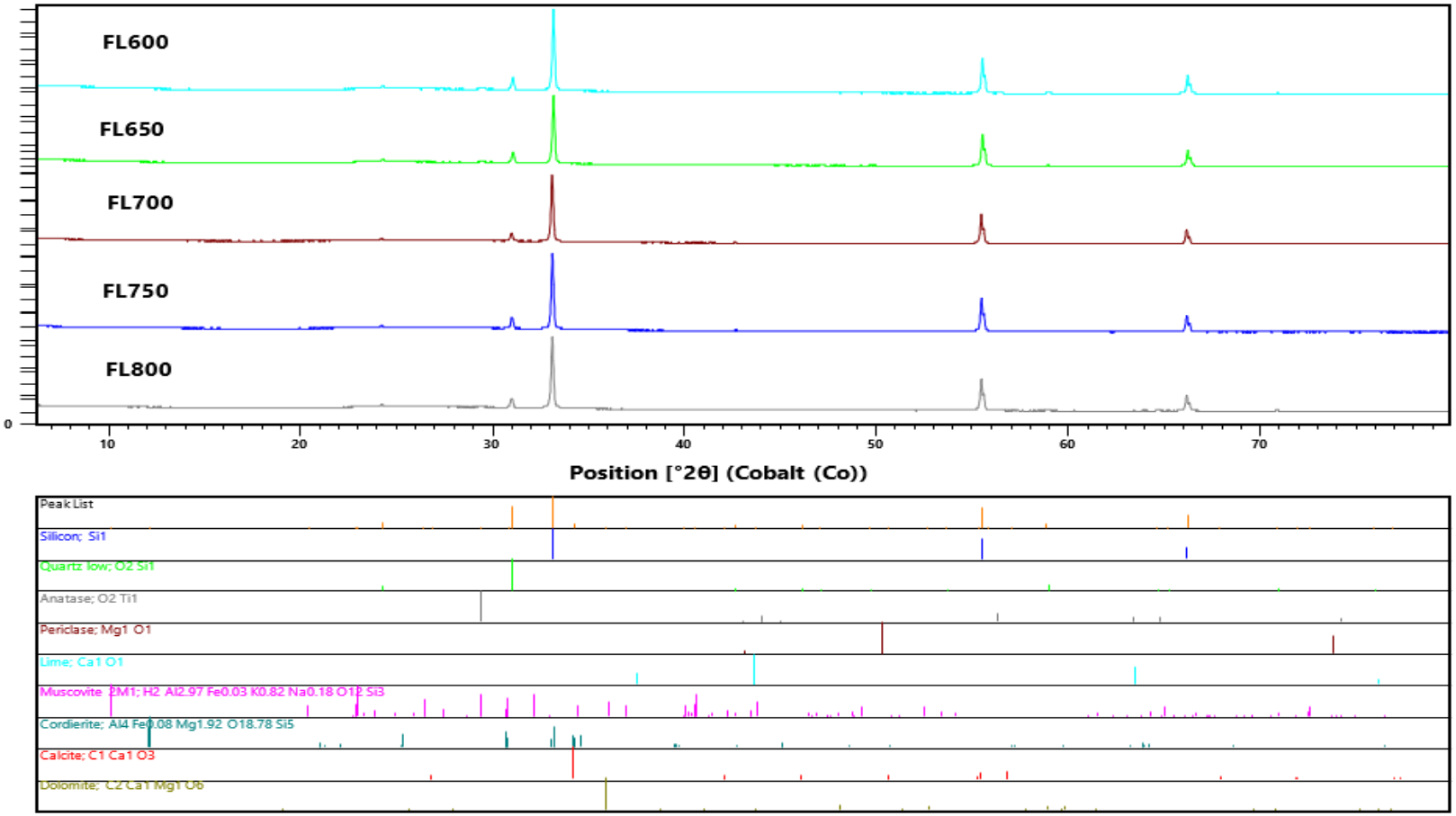

Figure 4.6: X-ray diffraction patterns of calcined FL clays

Figure *4.7* shows the differences in the XRD peak patterns of the calcined F clays between 600 and 800 °C. The sharp peaks and some small broad peaks at 24.3°2θ, 31°2θ, 33.2°2θ, 46.2°2θ, 55.5°2θ, 59°2θ, 66.5°2θ and 71°2θ indicated the presence of quartz in the calcined samples. Kaolinite peaks at 15°2θ, 23.9°2θ and 24.9°2θ in the raw F clay (Figure *4.1*) were not visible in X-ray diffraction patterns of the calcined clays. The disappearance of kaolinite peaks was supported by the thermal behavior of F clay (Figure *4.4*), where the dehydroxylation of kaolinite was expected to occur between 390 °C and 540 °C and beyond the dehydroxylation temperature range.

However, small and broad peaks of muscovite at 10.3°2θ and 23°2θ were present in all samples, indicating incomplete transformation of muscovite. Meanwhile, the broad 6.5 °2θ elevation disappeared after calcination, indicating that the smectite became completely amorphous at all calcination temperatures. The decomposition of calcite at 600 °C, 650 °C, and 700 °C was not fully completed because the reflection peaks were still visible, but the intensity weakened significantly. Hanein et al, (2022) stated that clay minerals possess the inherent ability to bind divalent exchangeable cations (Ca^{2+}) more tightly and with more water than monovalent exchangeable cations (Na^{+}). Researchers have further proposed that this results in a higher dehydration temperature being required to eliminate excess water for the divalent interlayer cations, which demands more energy (Hanein *et al.*, 2022).

At 750 °C and 800 °C, the decomposition of calcite was complete, with no visible reflection peaks. This confirmed the thermal behavior of F clay (Figure *4.4*), which demonstrated that decarbonation occurred between 540 and 740 °C. A broad small peak for dolomite was visible at 600°C, indicating partial decomposition of dolomite, which disappeared in the other F clay samples as the calcination temperature increased. The lime (42.8°2θ) and periclase (49.8°2θ) phases, which are the products of the thermal decomposition of calcite and dolomite, appeared in very small peaks, indicating that most of these phases are probably amorphous (Orosco *et al.*, 2014).

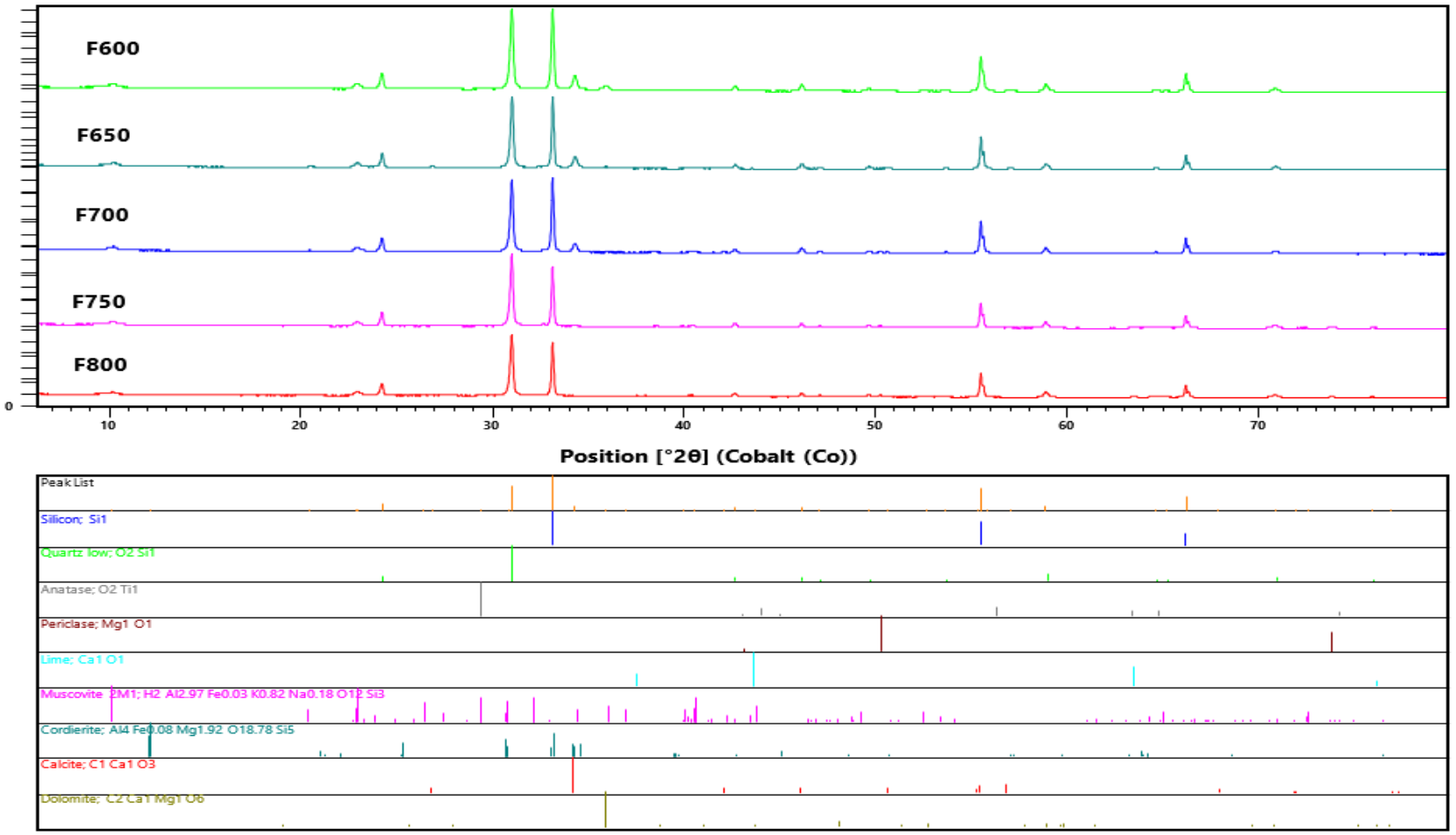

Figure 4.7: X-ray diffraction patterns of calcined F clays

Impurities such as quartz and feldspar, which are commonly found in clay, tend to remain unconverted during calcination and do not hinder the process. Despite their refractory properties, these impurities consume thermal energy, along with the rest of the clay minerals, to achieve a homogenous target temperature during heating (Hanein *et al.*, 2022). This observation usually occurs below the melting point of quartz and feldspar. In contrast, the mineralogy of calcined clay can be influenced by certain minerals, such as gibbsite and calcite, which undergo calcination or decomposition at the same temperatures as kaolinitic clay (Hanein *et al.*, 2022). The presence of calcite in raw clay can have a detrimental impact on the reactivity of calcined kaolinitic clay. According to Zunino *et al.* (2020), calcite breaks down into free lime and carbon dioxide gas between 600 and 800 °C. Furthermore, calcite impurities decrease the specific surface area of calcined kaolinitic clays, thereby reducing their reactivity (Zunino *et al.*, 2020).

The raw BL and FL clay are clays with kaolinite/muscovite/quartz mixtures, whereas F clay has a kaolinite/muscovite/quartz/smectite/carbonate mixture. The complete transformation of kaolinite was demonstrated by the disappearance of the kaolinite peaks at 600°C within the investigated calcination temperature range. This observation was maintained up to 800 °C. Similar work by Escalera et al. (2014), reported complete transformation of kaolinite to amorphous metakaolinite at 650 °C for both IC (kaolinite/illite) and EC (kaolinite/illite/smectite/quartz) clay samples. Furthermore, the illite peaks were less intense while still identified in both samples and disappeared at 1050°C, suggesting the collapse of the illite structure. Another study by Si et al, (2012) obtained optimum calcination of 600 °C for complete transformation of kaolinite in K-JS (Kaolinite) and K-SX(kaolinite/quartz/muscovite). Furthermore, kaolinitic clays were completely transformed to amorphous structure at 700 °C, smectitic clay (Ca-rich) optimal calcination at 800°C where the structure collapsed and optimal temperature for illite was 800 and 900 °C. These results were obtained in a study reported by Adriaens et al, (2016). Tironi et al, (2014) reported the transformation of kaolinite to amorphous metakaolinite through complete dehydroxylation for K1(kaolinite/quartz/anatase) and K2 (kaolinite/quartz/anatase/illite) clays at 700 and 750 °C, respectively. Additionally, metakaolinite recrystallized to the spinel

phase between the calcination temperature of 700 and 750°C. A study reported by Nawel *et al.* (2020) indicated complete dehydroxylation of kaolinite by disappearance of kaolinite peaks at 600°C for Clay 1 (kaolinite/illite/smectite) and clay 2 (kaolinite/illite/smectite/calcite/goethite/quartz). In addition, Nawel *et al.* (2020) stated that kaolinite became amorphous metakaolinite which indicated a very significant loss of crystallinity. However, illite and muscovite were not completely decomposed at this temperature. Al-ajeel and Al-sindy (2006) reported that raw Iraqi kaolinitic clay exhibited reduced crystallinity and became amorphous at 720 °C. Further calcination at 750 °C resulted in the formation of a minor recrystallized phase of aluminum silicate. Finally, (Udochukwu et al. (2019a) observed the disappearance of the kaolinite peaks at 500-800°C. The various clay minerals in the clay sample matrix influenced the thermal behavior of the clays during calcination, resulting in different optimal temperatures for the complete dehydroxylation of kaolinite. According to Pepper et al. (2021), the key factor contributing to the lower conversion temperature of kaolinite to amorphous metakaolinite is the disorder of kaolin. Ramadji et al. (2022) clarified further that the factors affecting the reactivity of clays include not only the kaolinite content, but also variables such as calcination temperature, time, and mode, as well as the crystalline structure of the clays, whether they are ordered or disordered, and their particle size.

4.3.2. Mineralogical composition of calcined clays

The Rietveld method was employed to determine the phase compositions of the calcined BL clays, and the results are presented in Table *4.3*. The disappearance of kaolinite suggested the formation of an amorphous phase known as metakaolinite, which results from the thermal transformation or complete dehydration of clay. (Udochukwu *et al.*, 2019b). Moreover, metakaolinite appeared amorphous in the XRD analysis and was a homogeneous mixture of noncrystalline alumina and silica at the molecular level (Udochukwu *et al.*, 2019b).

The raw BL clay sample, composed of quartz, kaolinite, muscovite, and traces of anatase (Table 4.1), transformed at various calcination temperatures. As shown in Table *4.3*, kaolinite was completely dehydroxylated and transformed into amorphous metakaolinite between 600 °C and 800°C. This transformation suggested that the crystal structure of kaolinite was disrupted and broken down into a less ordered form. The amorphous phase consisted of disordered aluminosilicate compounds or other noncrystalline materials.

Muscovite, on the other hand, maintained its crystalline structure at all calcination temperatures from 600 to 800°C and was only dehydroxylated. Lu et al. (2020) suggested that due to the dehydroxylation process of muscovite not taking place uniformly, as some OH groups are lost while others remain and as the Al cations became more firmly associated with the fivefold-coordinated framework, they resisted further dehydroxylation. Furthermore, Gridi-bennadji et al. (2008) stated that as the calcination temperature is increased to higher temperatures, the muscovite structure changes progressively and continuously, and the structure becomes increasingly disorganized.

In addition, quartz, and traces of anatase (except at 600°C) retained their crystalline structures at all calcination temperatures. Anatase was detected in the raw BL clay, however, it was not present at a temperature of 600°C and reappeared at temperatures from 650°C to 800°C. According to Fabbri et al. (2013), anatase was likely present in the raw clay of nanometric crystals associated with kaolinite surfaces. However, it was not detected by XRD because it may have been encapsulated within the formed disordered amorphous metakaolinite phase. The reappearance of anatase at 650 to 800 °C suggested that the anatase phase was stable, as there was no indication from the XRD diffractions that it transformed into the rutile phase with increasing temperature (Poo-Arporn *et al.*, 2020). Additionally, titanium may also be derived from muscovite in the clay, which underwent earlier replacement of octahedral Al^{3+} with Ti^{4+} (Erdemoğlu et al., 2020).

Table 4.3: Mineralogical composition of calcined BL clay

°C	Quartz	Anatase	Periclase	Lime	Muscovite	Cordierite	Calcite	Dolomite	Amorphous
600	12	0	0	0	1.8	0.2	0	0.6	85.3
650	13	0.3	0	0	2.1	0.4	0	0.1	84.1
700	12.6	0.3	0	0	1.9	0.5	0.3	0.2	84.1
750	12.6	0.4	0	0	1.6	0.4	0	0	84.9
800	12.3	0.5	0	0	1.5	0.4	0	0	85.4

Traces of cordierite were formed at all calcination temperatures. It is possible that the raw BL clay contained chlorite because the peaks for kaolinite and chlorite overlapped in the XRD analysis. This aligns with the results of Orosco et al. (2014), who suggested that the formation of cordierite was due to the reaction between $MgCl_2$ and O_2, which are produced through the chlorination of periclase and lime with metakaolinite. This reaction then yields mullite and enstatite, which further reacts with Cl_2 to form cordierite, liquid $MgCl_2$, and O_2. Orosco et al. (2014) also observed the presence of cordierite at 700 °C following the thermal treatment of a kaolinitic clay and dolomite mixture in a chlorine atmosphere. However, mullite and enstatite were not observed in the calcined BL clay. Another way to explain the presence of cordierite in calcined BL clays is to observe its location in the MgO-Al_2O_3-SiO_2 phase diagram in Appendix A (Figure A 1), which indicated that it falls within the range of the primary mullite phase. Cordierite is formed through a solid-state reaction involving MgO, Al_2O_3, and SiO_2, or from materials containing these oxides, at temperatures ranging from 1100 to 1400°C (Zirczy, 1972). Although the theoretical composition of cordierite lies within the primary field of mullite, the absence of mullite in the body is typically due to incomplete reactions or overfiring (Zirczy, 1972). However, in this study, the calcination temperature ranged from 600 to 800 °C. Cordierite was detected in the calcined clays, whereas mullite was not detected in the XRD analysis. It was speculated that some of the clay minerals and oxides influenced the shift of cordierite from higher calcination temperatures to reduced calcination temperatures, or this observation might have been due to the prolonged calcination time of 8 hours. Consequently, the clay was overheated.

Traces of dolomite appeared as a new phase between calcination temperatures of 600 and 700 °C. The appearance of dolomite was attributed to the fact that as water was released from the clay matrix, clay minerals were exposed and could be detected by XRD, whereas in raw clay, they might have not been detected because they were closed within other clay minerals. During the weathering of muscovite, K^+ migrates from the intermediate layer and is partly substituted by other cations, such as Ca^{2+} and Na^+, whereas in the tetrahedral layer, Si^{4+} is partially substituted by Al^{3+}. In octahedral layers, Al^{3+} is substituted by Fe^{3+}, Mg^{2+}, and Fe^{2+} (Overmann et al., 2024). The possibility of dolomite formation during the dehydroxylation of muscovite, as the atoms are rearranged, is apparent. Additionally, dolomite partially decomposed to calcite at 700 °C. Dolomite and calcite fully decomposed at 750 °C. Moreover, no dolomite or calcite was present at 800 °C. However, the semi-quantitative XRD analysis did not indicate any amount of periclase. The transitional calcite formed at 700°C was fully decomposed at temperatures above 750°C; however, no free lime was observed in the XRD pattern. Trindade *et al.* (2009) reported that the calcite formed was a transitional phase, where it was observed that it disappeared at 750 and 800°C. According to Abdullah *et al.*, (2021), the calcination of $MgCO_3$ in dolomite occurs at lower temperatures and is much faster than that of $CaCO_3$. As the temperature increased, the calcination of $CaCO_3$ occurred once $MgCO_3$ was completely calcined, and the particles reached their peak porosity and specific surface area. (Abdullah *et al.*, 2021). Abdullah *et al.*, (2021) further reported that calcination of dolomite for 6 hours occurred in two stages, starting to decompose at 600°C and completing at 800°C. At these temperatures, calcite and magnesium oxide were formed, whereas at higher temperatures, calcite decomposed to CaO. The absence of periclase indicated that it might have reacted with other clay minerals or oxides to form Mg-containing minerals, such as cordierite.

Table 4.4: Mineralogical composition of calcined FL clays

°C	Quartz	Anatase	Periclase	Lime	Muscovite	Cordierite	Calcite	Dolomite	Amorphous
600	4.5	0.4	0	0	2.2	0.3	0	0.3	92.4
650	4.5	0.3	0	0	3	0.1	0	0.3	91.7
700	3.6	0.3	0	0	1.1	0.3	0.1	0.3	94.2
750	4.5	0.4	0	0	1.7	0.3	0.1	0.2	92.8
800	4.1	0.3	0.1	0	1.9	0.4	0	0	93.3

As shown in Table *4.4*, kaolinite transformed into amorphous metakaolinite at temperatures from 600 to 800°C, with no collapse of the crystal structure of muscovite. Additionally, muscovite preserved its crystalline structure as it was dehydroxylated in this temperature range. Quartz and anatase remained intact after calcination, as the minerals retained their crystalline structures at all calcination temperatures. Traces of newly formed cordierite were also observed between 600 °C and 800°C. The raw FL clay contained trace amounts of dolomite at 0.1%, which persisted after calcination at 600, 650, 700, and 750°C, although at trace levels of 0.3%, 0.3%, 0.3%, and 0.2%, respectively. However, at 700 °C and 750°C, dolomite partially decomposed to calcite, and no periclase was observed in the semi-quantitative XRD results. Transitional calcite formed at 700 and 750 °C fully decomposed at 800°C, but no free lime was detected in the semi-quantitative XRD results. Interestingly, periclase was observed at 800°C in the absence of dolomite and calcite. The presence of periclase at 800 °C indicated that not all MgO was used in the formation of cordierite. Mineralogical changes similar to BL clay samples calcined at 700°C were observed for FL clay samples calcined at 700 and 750°C.

The semi-quantitative XRD results for the calcined F clay are displayed in Table *4.5*, revealing the mineralogical compositions of the calcined F clays. At temperatures ranging from 600 to 800°C, kaolinite was transformed into amorphous metakaolinite by the release of structural water. Additionally, smectite was converted into an amorphous phase between calcination temperatures of 600 and 800 °C (Hollanders, 2017). Muscovite underwent dehydroxylation while preserving its crystalline structure, whereas the presence of quartz was persistent at all calcination temperatures. According to Erdemoğlu et al. (2020), the

dehydroxylation process of muscovite was not consistent, causing some OH groups to be lost while others remained and became strongly attached to the five-fold-coordinated Al cations, thereby inhibiting additional dehydroxylation. Biswas et al. (2023) reported that micas did not become fully amorphous after dehydroxylation at temperatures above 800°C but remained in a structurally modified state.

Table 4.5: Mineralogical composition of calcined F clays

°C	Quartz	Anatase	Periclase	Lime	Muscovite	Cordierite	Calcite	Dolomite	Amorphous
600	35.4	0	0.1	0	8.8	0.7	9.7	6.8	38.5
650	37.6	0	0.3	0	9.2	0.6	11.5	2.6	38.2
700	35.5	0	0.8	0	7.8	0.8	7.4	0	47.6
750	44	0	1.5	0.1	11.3	1.2	0.9	0	41
800	42.7	0	1.6	0.5	10.1	0.9	0.5	0	43.8

The disappearance of anatase and the emergence of cordierite were observed at all calcination temperatures. In addition, similar to the observations for calcined BL clay at 600°C, anatase disappeared in all calcined F clays, with no new phase related to the decomposition of anatase. Cordierite has emerged as a new mineral phase in solid-state reactions that involve MgO, Al_2O_3, and SiO_2. At 600 °C and 650°C, dolomite partially decomposed into calcite and periclase, adding to the calcite content already present in raw F clay from 7.5% to 9.7% at 600 °C and 11.5% at 650 °C. This indicated that calcite decomposition did not occur at 600 and 650 °C. Furthermore, dolomite fully decomposed at 700°C to calcite and periclase, as shown in Equation 4.1 and 4.2. At the same temperature of 700 °C, calcite partially decomposed into free lime and releasing carbon dioxide gas. However, no free lime was observed after the calcination at 700°C. Calcite partially decomposed further to lime at 750 °C and 800 °C, as shown in Equation 4.3. Dolomite was absent above 700°C, whereas traces of calcite were observed at 750 °C and 800°C. The issue is the disappearance of calcium from calcite, as XRD did not reveal any other crystalline phase that contains calcium. The Rietveld refinement suggested that only a small fraction of the decomposed calcite can be accounted for at 750°C (0.1%) and 800°C (0.5%) in terms of the available free lime. According to Overmann et al. (2024), CaO may be deposited in a granular form on metakolinite, functioning as

an amorphous intermediate stage between free lime and metakaolinite, before the recrystallization of the Ca-containing phase. Zunino et al. (2020) found that calcite impurity deposits on the metakaolin surface reduced the specific area and, consequently, reactivity.

$$CaMg(CO_3)_2(dolomite) \rightarrow CaCO_3(calcite) + MgO(periclase) + CO_{2(g)} \quad 4.1$$

$$CaMg(CO_3)_2(dolomite) \rightarrow CaO(lime) + MgO(periclase) + CO_{2(g)} \quad 4.2$$

$$CaCO_3(calcite) \rightarrow CaO(free\ lime) + CO_{2(g)} \quad 4.3$$

Determining the ideal calcination temperature for mixed clays is challenging because of the differing activation mechanisms of various clay minerals. For example, kaolinite requires a lower calcination temperature than illite and montmorillonite, owing to the availability of accessible OH^- ions on the interlayer surface of the octahedral sheet (Overmann et al., 2024). In contrast, three-layer silicates have OH^- ions situated between SiO_4 tetrahedral sheets, necessitating higher dehydroxylation temperatures (Overmann et al., 2024). Furthermore, after dehydroxylation, these minerals retain their crystalline structures, and amorphization takes place at elevated temperatures through sintering, leading to a decrease in specific surface area (Overmann et al., 2024). Consequently, a reduction in reactivity occurs in a physical manner. However, within the calcination temperature range of this study, the muscovite structure did not completely break down. The transformation of kaolinite through dehydroxylation led to the formation of an amorphous metakaolinite structure accompanied by lattice distortions. Moreover, the optimal temperature for the dehydroxylation process was highly sensitive to the makeup of the smectite clays. Although dehydroxylation of

muscovite occurred, no changes in the mineralogy were visible by XRD. Overmann et al, (2024) noted that, in contrast to kaolinite, illite amorphization primarily takes place through sintering and glass formation, similarly to montmorillonite.

Calcination caused mineralogical changes in the BL, FL, and F clay minerals. As a result, an amorphous phase was formed, likely due to the thermal decomposition and reorganization of the original crystalline structures present in the raw BL, FL, and F clays (Figure *4.8*). This amorphous phase persisted over the range of calcination temperatures (600-800°C). The amorphous phase of the calcined BL clay ranged from 85.3% at 600°C to 85.4% at 800°C, and the amorphous phase of the calcined FL clay ranged from 92.4% at 600°C to 93.3% at 800°C. The consistently high levels of amorphous content across the temperature range indicated significant sensitivity of the BL and FL clay minerals to calcination conditions. This temperature-dependent trend indicated that higher calcination temperatures were effective in promoting the formation of the amorphous phase.

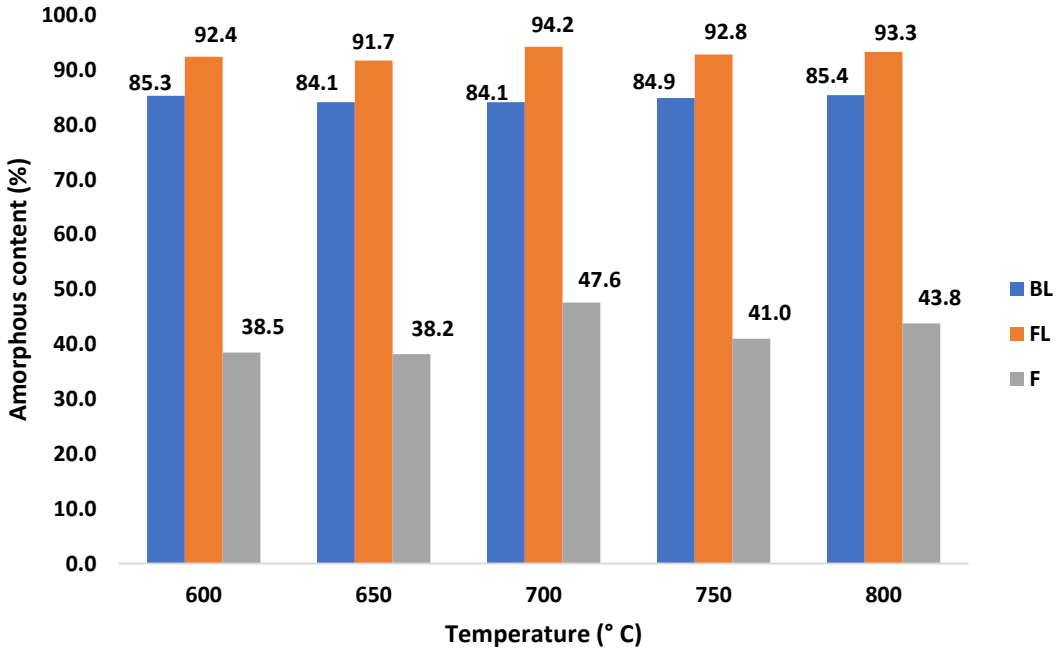

Figure 4.8: Amorphous content of calcined BL, FL, and F clays

The calcined F clay exhibited an amorphous content that varied between 38.5% and 43.8% as the calcination temperature was elevated from 600 °C to 800°C. This variation demonstrates the responsiveness of the clay minerals to increasing calcination temperatures during the process. Moreover, this nonlinear trend indicates that multiple factors are involved in shaping the formation of the amorphous phase at different temperatures. According to Ramadji et al. (2022), the early development of the amorphous content can be attributed to the disintegration and transformation of the crystalline structures within the clay, leading to the formation of an amorphous phase. Furthermore, the subsequent decline suggested the restructuring of the amorphous phase. Ramadji et al. (2022) further emphasized that the content of amorphous kaolinite is crucial in determining the reactivity of calcined clays, as calcination has the potential to induce kaolinite recrystallization. However, there is no clear agreement in the literature regarding the slight impact of increasing the calcination temperature on the reactivity. Overmann et al. (2024) stated that at approximately 600°C, complete dehydroxylation results in high reactivity, and kaolinite exhibits reduced sensitivity to elevated temperature treatments, extending up to approximately 900 °C.

4.3.3 Fourier transform infrared spectroscopy results for raw and calcined clays

Infrared analysis is a widely utilized tool for identifying minerals in clay materials, evaluating their structures, and detecting possible differences in their structures (Ramadji *et al.*, 2022). According to Vaculíková et al. (2011), the infrared spectrum can reveal the kaolinite structural disorder by highlighting the variations in the locations and relative intensities of the OH bending and stretching bands. Furthermore, the doublets at 3696 and 3620 cm^{-1} doublets are distinctive to the kaolin group (Vaculíková *et al.* 2011). The transformation of kaolinite to the amorphous phase is commonly linked to the elimination of water molecules and dehydroxylation of kaolinite, which involves the loss of hydroxyl groups from its structure.

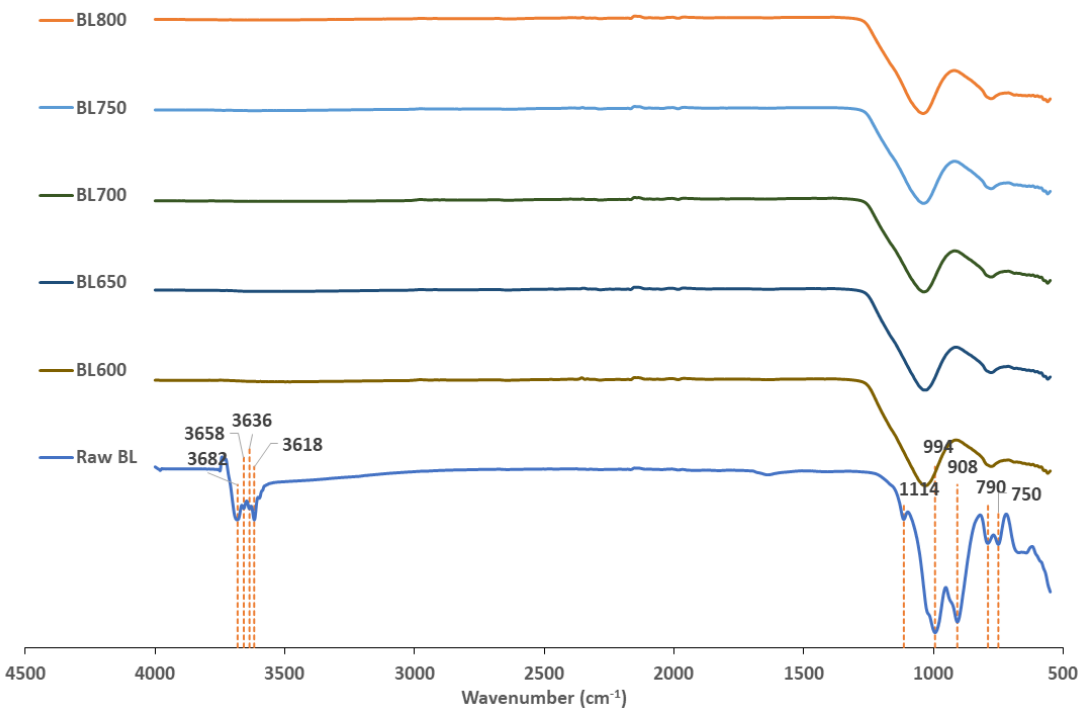

Figure 4.9: IR spectra of raw and calcined BL clays

Figure *4.9* shows that in raw BL clay, the peak at 750 cm^{-1} (OH translation of Al^{VI}-OH) is ascribed to the lattice vibration of kaolinite, which disappears upon dehydroxylation (Zunino *et al.*, 2020) and 790 cm^{-1} is assigned to the Si-O-Si symmetric stretching vibrations of kaolinite (Xue *et al.*, 2023). The band at approximately 908 cm^{-1} was assigned to OH^- bending vibrations, whereas the peak at 994 cm^{-1} was attributed to the Si-O-Si asymmetric stretching vibrations of kaolinite, which widened as the structure underwent dehydroxylation-induced distortion (Zunino *et al.*, 2020). The peak at 1114 cm^{-1} is assigned to the vibration of O^{-2} atoms perpendicular to the kaolinite layers (Si-O-Al^{VI}), and is also impacted by defects in stacking that may be caused by the calcination of clay (Zunino *et al.*, 2020). Moreover, the feature bands of quartz at 1114 and 790 cm^{-1} were weak, indicating that the quartz content in raw BL clay was lower than that of kaolinite, which corresponds to the XRD results in **Error! Reference source not found.** (Xue *et al.*, 2023). The peak at 3618 cm^{-1} was assigned to the inner hydroxyl groups located at the junction of the Si tetrahedral and Al octahedral layers, whereas those

at 3636, 3658, and 3682 cm^{-1} were related to the OH^- stretching vibrations of the hydroxyl groups located at the basal surface of the Al layer of kaolinite (Souri *et al.*, 2015). Dehydroxylation is expected to lead to the disappearance of the latter peaks, as they are associated with water molecules present in kaolinite (Zunino *et al.*, 2020).

The FTIR analysis confirmed the structural changes in the BL clay samples calcined at 600–800°C (Figure *4.9*). In the calcined BL clay samples, the weak peak at 1114 cm^{-1} was combined with the band at 994 cm^{-1}, associated with the Si-O stretching vibrations of kaolinite, which widened and moved towards higher wavenumbers. Moreover, the Si-O-Si symmetric stretching vibration of kaolinite at 790 cm^{-1}broadened. These changes indicated that the degree of crystallinity of kaolinite was reduced (Xue *et al.*, 2023). The peaks linked to hydroxyl stretching vibrations at 3618, 3636, 3658, and 3682 cm^{-1} and the OH bending vibrations at 908 cm^{-1} completely disappeared. This indicated that OH was completely removed by calcination (Xue *et al.*, 2023).

According to Xue et al. (2018), a peak should appear at approximately 876 cm-1, indicating that the VI-coordinated Al in kaolinite was transformed into IV-coordinated Al in metakaolinite. However, this peak was not observed in the IR spectra of calcined BL clays. As the diffraction peak intensities of kaolinite disappeared at 600°C (Figure 4.5), kaolinite was completely transformed into an amorphous phase, and this observation was maintained up to 800°C. It is possible that during the calcination of the raw BL clay, the layers of metakaolinite became compact and sintered, transforming into amorphous aluminosilicate owing to the long calcination time (Xue *et al.*, 2023). Consequently, the reactivity of kaolinite was reduced. The HCl leaching results of Al show the reactivity of the amorphous phase formed in section 5.1.

In the FTIR spectrum of the raw FL clay (Figure *4.10*), the peak at 1116 cm^{-1} was assigned to the Si-O-Si^{VI} (apical Si) stretching vibrations (Xue *et al.*, 2023), and the peak at 998 cm^{-1} resulted from the asymmetric stretching vibrations of Si-O-Si (Tantawy and Alomari, 2019). The peak at 910 cm^{-1} was attributed to the bending of Al-O-H vibrations (OH groups positioned on the alumina faces)(Tantawy and

Alomari, 2019). The peaks at 642 and 750 cm^{-1} and 792 cm^{-1} are assigned to the OH translation of Al^{VI}-OH and Si-O-Si symmetric stretching of kaolinite lattice vibrations, respectively (Xue *et al.*, 2023).

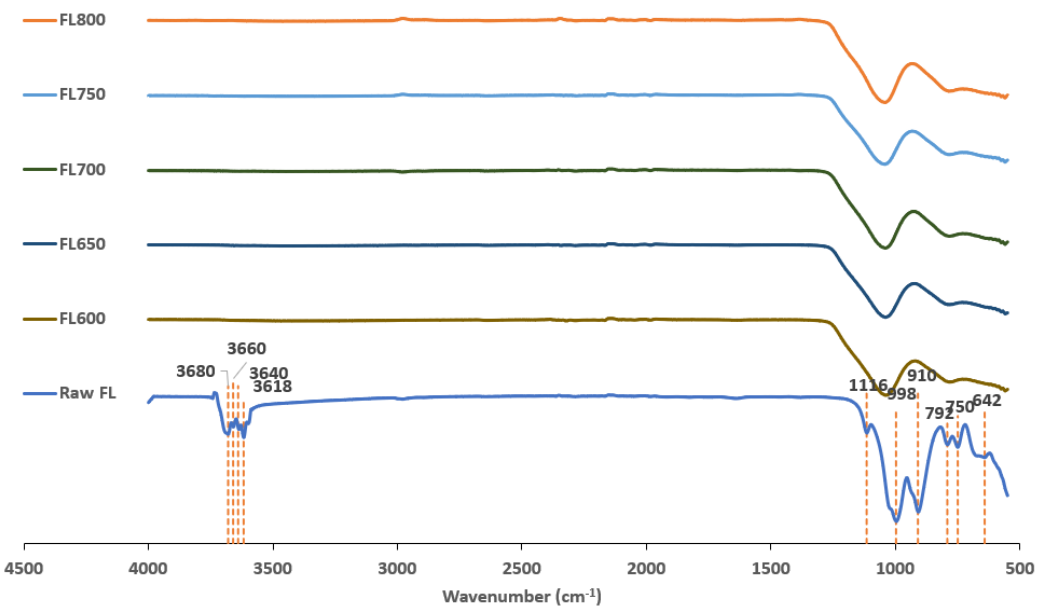

Figure 4.10: IR spectra of raw and calcined FL clays

The quartz content in raw FL clay was lower than that of kaolinite, indicated by weak feature bands at 1116 and 792 cm^{-1}, which corresponded to the XRD results in **Error! Reference source not found.** (Xue et al., 2018). The peak at 3618 cm^{-1} was assigned to the stretching band of the intra-layer OH group, whereas the peaks at 3640, 3660, and 3680 cm^{-1} were related to the inner-surface OH groups stretching modes (Kuranga *et al.*, 2018; Zunino *et al.*, 2020).

In the FTIR spectra of the FL calcined clays, the peak at 1116 cm^{-1} combined with the peak at 998 cm^{-1} broadened and shifted to approximately 1090 cm^{-1}. This suggested the presence of Si-O stretching vibrations of amorphous SiO_2 (Tantawy and Alomari, 2019). The peak at 792 cm^{-1}, assigned to Si-O-Si symmetric stretching vibrations, also broadened. Moreover, the hydroxyl groups and peaks at 642 and 750 cm^{-1} disappeared at all calcination temperatures.

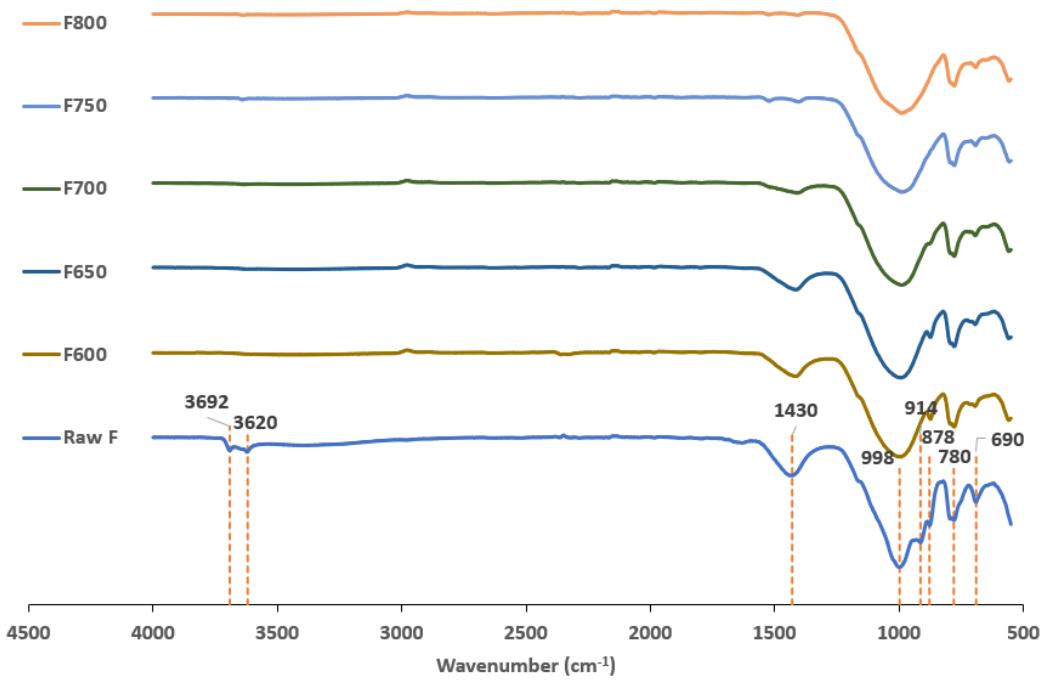

Figure 4.11: IR spectra of raw and calcined F clays

Figure *4.11* for calcined F clays showed that the peak at 878 cm^{-1} matched with the asymmetric out-of-plane bending of CO_3 (Zunino *et al.*, 2020). The peaks at 690 and 780 cm^{-1} were assigned to the O-Si-O bending and Si-O-Si symmetric stretching of the kaolinite lattice vibration, respectively. The strong intensities of the peaks at 690 and 780 cm^{-1} in the spectrum suggested that the quartz content in the raw F clay was higher than the kaolinite content, which is consistent with the XRD results shown in **Error! Reference source not found.**.The band at approximately 914 cm^{-1} was assigned to OH bending vibrations, whereas the peak at 998 cm^{-1} was attributed to the Si-O-Si asymmetric stretching vibrations of kaolinite. The broad band at 1430 cm^{-1} is assigned to the asymmetric stretching of CO_3^{2-} (Xue *et al.*, 2023). The peak at 3620 cm^{-1} is assigned to the inner OH group stretching bond in the kaolinite structure, in the plane between tetrahedral and octahedral sheets, whereas the peak at 3692 cm^{-1} is related to the OH vibrations that are related to Al octahedral sheet (Tironi *et al.*, 2014).

The asymmetric stretching of the CO_3 peak at 1430 cm^{-1} was visible at 600, 650, and 700 °C, indicated the presence of calcite in the calcined clays, which agrees

with the XRD results (Figure 4.7). At 750 and 800 °C, the carbonates in the F clay samples appeared to be fully decomposed because the two small peaks that emerged within 1400 and 1600 cm^{-1} were associated with calcite residues. Moreover, a gradual decrease in peak intensity at 1430 cm^{-1} was observed as the calcination temperature increased, particularly at 700°C, indicating the partial decomposition of calcite. The asymmetric out-of-plane bending of the CO_3 peak at 878 followed the same trend as that of the peak at 1430 cm^{-1} for the calcined clays. However, a notable peak typically associated with free lime at around 3650 cm^{-1} was not identified in these particular samples (Zunino *et al.*, 2020). These results may be explained by the formation of a new phase, most likely an amorphous transition state between free lime and metakolinite, and the crystalline phases expected at higher temperatures, such as wollastonite, anorthite, and gehlenite (Zunino *et al.*, 2020). Furthermore, upon decomposition of calcite, CaO can combine with kaolinite to produce a calcium-rich phase that covers the metakolinite particles, thereby decreasing their specific surface area.(Zunino *et al.*, 2020).

The inner and inner surface OH stretching vibrations at 3620 and 3692 cm^{-1} disappeared at all calcination temperatures. Meanwhile, the asymmetric stretching of Si-O-Si gradually broadened as the calcination temperature increased without shifting to higher wavenumbers. These different changes indicated partial disorder effects compared with the BL and FL results. Although no kaolinite peaks were visible in the XRD analysis (Figure 4.7), the semi-quantitative XRD results showed less than 50% amorphous phase at all calcination temperatures. The kaolinite dehydroxylation results, displaying a mass loss of 2.170%, validated the low kaolinite content present, as suggested by DGA/DTA analysis (Figure *4.4*).

Several studies reported complete dehydroxylation of kaolinite between 450 to 850 °C by the disappearance of Al-OH and OH bands and the Si-O characteristic bands of kaolinite present in the raw clay transitioning into a single absorption band, indicative of the characteristic of amorphous silica (Tironi *et al.*, 2012 ; Kassa et al., 2022 ; Tantawy and Ali Alomari, 2019). Overall, FTIR analysis showed structural changes in calcined BL, FL, and F clays.

During calcination, the octahedral coordination of alumina changes to tetrahedral; hence, tetrahedrally coordinated aluminum is more receptive to acid attack (Suraj *et al.*, 1998). Acid attack leaches the metal ions from the lattice structure because of the disorder caused by the transition of kaolinite to metakaolinite. After calcination, the LOI values were low at all temperatures and below 1.6% for BL and FL clays, confirming the occurrence of dehydroxylation (Table *4.6*).

Table 4.6: Loss of ignition of calcined clays

Loss of ignition (%)			
°C	BL	FL	F
600	1.40	1.54	9.19
650	1.28	1.49	8.07
700	0.835	0.866	5.10
750	0.730	0.692	2.30
800	0.495	0.046	1.54

The LOI measures the weight loss experienced by a material when subjected to heating, indicating the presence of volatile components such as organic matter, water, and carbonates (Heiri *et al.*, 2001). Moreover, the LOI value is directly linked to the oxidation of organic matter, decomposition of carbonates, and hydroxides, dehydroxylation of clay minerals (Chinet al., 2017). Raw BL clay (**Error! Reference source not found.**) initially exhibited an LOI of 12.6 %, suggesting a significant proportion of volatile constituents. Table *4.6* shows that as the temperature increased, the LOI values consistently decreased, indicating the progressive removal of volatile components. At 600°C, the LOI decreased to 1.40%, and this trend continued, with lower values at higher calcination temperatures: 1.28% at 650°C, 0.835% at 700°C, 0.730% at 750 °C, and 0.495% at 800 °C. The initial LOI value of 13.5% (Table 4.2 indicated a substantial amount of volatile constituents, including water, organic matter, and carbonates, within the raw FL clay. As the calcination temperature increased during the calcination process, a consistent decrease in the LOI values was observed. At 600°C, the LOI was

reduced to 1.54%, followed by further decrease at higher temperatures: 1.49% at 650 °C, 0.866% at 700 °C, 0.692% at 750 °C, and a remarkably low value of 0.046% at 800°C. The decrease in LOI values can be ascribed to the discharge of water, carbon dioxide, and other volatile compounds during the calcination process. Additionally, the decrease in the LOI was particularly pronounced at higher calcination temperatures.

The initial LOI of the raw F clay sample (Table 4.2) was 14.2%. As the calcination temperature was increased, a notable decrease in the LOI values was observed. At 600 °C, the LOI decreased to 9.19%, followed by further reductions at higher temperatures: 8.07% at 650 °C, 5.10% at 700 °C, 2.30% at 750 °C, and 1.54% at 800°C. This systematic decline suggests effective removal of volatile components, such as water, from the raw F clay matrix. The initial LOI values of the BL, FL, and F raw clays differed, indicating the occurrence of differing levels of volatile components in their natural states. The higher the initial LOI, the more volatile are the substances that are likely to be present. The F clay, with an initial LOI of 14.2%, appeared to retain more volatiles even after calcination than the BL and FL clays. At 800 °C, F clay achieved the same LOI of 1.54% as FL clay at 600 °C. The increased reactivity potential of kaolinite stems from its higher hydroxyl group content, which is situated within the crystal structure where Al is coordinated to a greater extent (Overmann *et al*., 2024). Throughout the dehydroxylation process, this results in increased disorder and enhanced exposure of the aluminum groups on the surface of the phases.

Chapter 5 Leaching of the Calcined Clays

5.1. HCl acid leaching of calcined clays results

The impact of changes in the calcination temperature on the extraction of Al and impurities, such as Ca, Fe, Ti, Si, Mg, and K was examined. In addition, the impact of the amorphous content of the calcined clays on the leaching efficiency was observed. Previous research (Al-ajeel and Al-sindy, 2006; Tantawy and Alomari, 2019; Dagde, 2019; Nnanwube and Onukwuli, 2023;Bagani *et al.*, 2021) on the leaching of kaolinitic clays in acid solutions has been conducted; however, based on our current information, the effects of calcination temperature on the mineralogical transformation and extraction of Al from South African kaolinitic clays have not been investigated. The connection between the structural changes and chemical reactivity induced by calcination was demonstrated by the leaching results. When a clay mineral is subjected to acid attack, the ions located in the octahedral sites leach out. Initially, mineral acids chemically attack the clay by absorbing onto the surface of the solid and replacing the exchangeable cations with protons. The protons that are adsorbed subsequently spread out into the lamella, and a chemical reaction takes place within it.(Do Nascimento *et al.*, 2015). In an octahedral sheet, the cations that constitute the structure become soluble, are selectively removed from the solid phase, and are absorbed into the liquid phase (Do Nascimento *et al.*, 2015). During HCl leaching, clay minerals lose exchangeable cations from both the octahedral and tetrahedral sheets, but the SiO_4 group in the tetrahedral sheets remains largely unchanged (Hu *et al.*, 2022). The impact of the calcination temperature on the recovery of alumina from BL, F, and FL clays was examined by leaching samples of clay calcined at temperatures of 600, 650, 700, 750, and 800°C. Other experimental conditions, such as acid

concentration, stirring rate, leaching duration and temperature, and solid/liquid ratio (S/L), were kept constant at 3M, 250 rpm, 2 hours, 70°C, and 0. l g/ml, respectively.

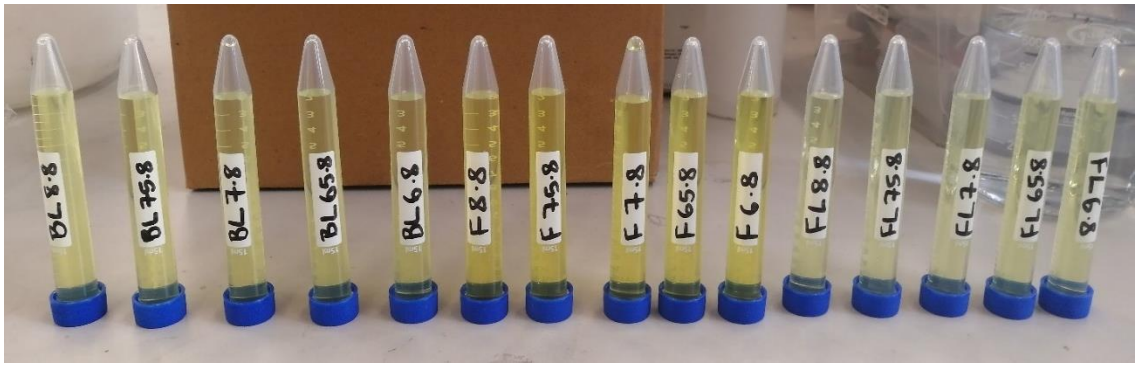

Figure 5.1: Leachates samples of calcined BL, FL, and F clays

Acid leaching of the calcined clays resulted in a color change, as shown in **Error! Reference source not found.**. The intensity of the yellow color decreased in the order of F clay > BL clay > FL clay. Additionally, the yellow color suggested the presence of iron (Al-Harahsheh *et al.*, 2023).

5.1.1. Element extractions at different calcination temperatures

The elemental extraction percentage was calculated using Equation 5.1. The initial concentration of elements in the clay sample was obtained from the ICP-OES results of the calcined clays, while the extraction of elements was based on the ICP-OES results of the leachates.

$$x = \left(\frac{C_{leachate}}{C_{calcined\ clay}}\right) \times 100 \qquad 5.1$$

Where x represents the element extraction percentage, $C_{leachate}$ is the amount of element in the leachate in grams and $C_{calcined\ clay}$ is the amount of element in the calcined clay in grams. An example is shown in Appendix B: Calculation example of extraction percentage.

Error! Reference source not found. shows Al and Fe extraction percentages for calcined BL clays at different calcination temperatures. The Al and Fe extraction of raw BL clay was 3.03 and 19.5%, respectively. After thermal heating of the BL clay at 600 °C, 79.4 % Al extraction was achieved. Large error bars indicated more variability, meaning the data points were more spread out. This could have been due to differences in the analytical equipment used to measure the leachate since the set of leachates was measured at different times. Furthermore, the highest Al extraction percentage at 600 °C was ascribed to the complete kaolinite dehydroxylation, progressive dehydroxylation of muscovite, and formation of the cordierite phase, which drastically increased aluminum solubility. The formation of an amorphous metakaolinite phase was validated by XRD (Figure 4.5), in which the kaolinite diffraction peaks disappeared at 600 °C, and by IR spectroscopy (Figure 4.9), in which all the characteristic absorptions of the hydroxyl groups disappeared at 600 °C. In addition, this was consistent with the thermal behavior results of BL clay in the TGA/DTA analyses (Figure 4.2) because the transformation of kaolinite occurred between 330 and 700 °C.

The resulting structure of kaolinite (amorphous metakaolinite) was disordered, and at the same time, Al octahedra of the kaolinite reformed to Al-tetrahedra (Nevrla *et al.*, 2021), exposing these Al groups at the surface of the plane to be leached to acid solution (Overmann et al., 2024). On the other hand, the crystallographic arrangement of the muscovite atoms did not change after dehydroxylation (Fernandez et al., 2011). However, the structural damage from calcination not only provided active sites but also increased the specific surface area to reduce the internal diffusion resistance of the leaching agents (Pei *et al.*, 2018). The fundamental component elements of cordierite are Al^{3+}, Mg^{2+}, and Si^{4+}. According to Bai and Guo (2006), the acid preferentially dissolved Al^{3+}, Mg^{2+}, and impurities including Fe^{3+}, K^{+}, and Na^{+}, while Si seems to remain within the cordierite structures treated with acid (Bai and Guo, 2006).

At a calcination temperature of 650 °C, the Al extraction reduced to 69.9% and 65.6% at 700 °C and 63.9% at 750 °C suggesting the structural rearrangement of amorphous metakaolinite to insoluble spinels (Johnston *et al.*, 2022a). A further calcination temperature increases from 650 °C to 800 °C showed no difference in

kaolinite transformation observations compared to the XRD results at 600 °C. Additionally, the IR spectra of the calcined BL clay at 650–800 °C showed no difference in the characteristic absorptions of the hydroxyl groups compared to those at 600 °C. The conversion of the amorphous metakaolinite phase to insoluble spinels was confirmed by the thermal behavior of the BL clays (Figure 4.2), in which the endothermic peak at 874.77 °C was assigned to spinel formation. Despite the formation of insoluble spinel, Al extraction slightly increased to 65.2% at 800°C, suggesting the release of Al ions from the initial breakdown structure of muscovite. Based on the presented results, a calcination temperature of 600 °C emerged as the optimal temperature for aluminum extraction from BL clay within the investigated calcination temperature range because a high aluminum recovery was obtained.

Compared with the results of this study, several studies have reported various Al extractions with thermally treated clays. The research conducted by Si, Qiao and Yu (2012) reported Al extraction from low-grade kaolin (K-JS) of 89.34 wt% and high-grade kaolin (K-SX) of 83.37 wt% at a calcination temperature of 600 °C. The Al extraction for K-SX decreased after calcination at 700 °C to 900°C, and for K-JS started after 600 °C. Another study by Al-Zahrani and Abdul-Majid (2009) reported that optimal conditions including, calcination at 600°C for 1 hour, followed by leaching with 6M HCl under reflux at boiling conditions, resulted in 63% alumina extraction. Furthermore, optimal conditions involving calcination at 600°C for 60 minutes, resulted in increased alumina solubilization (Udochukwu *et al.*, 2019). Other studies found high Al extraction at other calcination temperatures other than 600 °C, including Tantawy and Ali Alomari (2019), who found optimal conditions involving calcination at 850°C for 2 hours, followed by leaching with 6M HCl, resulting in 75% alumina recovery. Another study by Al-ajeel and Al-sindy (2006) achieved 99% alumina extraction by calcination at 720°C for 45 min, followed by leaching in 28 wt% HCl for 45 min at 100°C. Due to the difference in mineralogical compositions and crystallinity of kaolinitic clays from different locations, clay would obtain high Al dissolution under various calcination and leaching conditions.

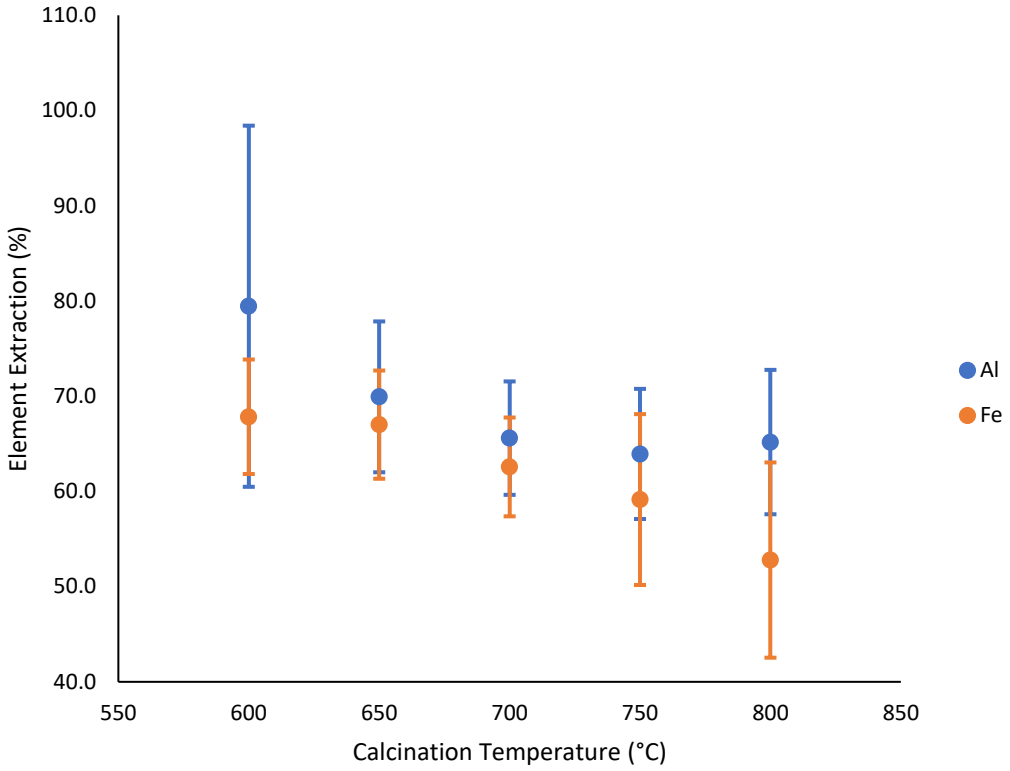

Figure 5.2: Al and Fe extraction percentages for calcined BL clay

The connection between the thermal dehydroxylation temperature and iron extraction revealed that an increase calcination temperature, reduced the amount of extracted iron as shown in **Error! Reference source not found.**. The presence of Fe_2O_3 can be accounted for by isomorphic substitution within the clay mineral structures or by a lower content of iron oxide, which was not detected by XRD analysis. Moreover, muscovite may exhibits potential substitutions of Fe^{2+} and Fe^{3+} in the octahedral sheets and Ca^{2+} in the interlayer (Barton and Karanthanasis, 2005). The high Fe dissolution at 600 and 650 °C of 67.8 and 67.0%, respectively, was attributed to the concurrent dissolution of Al and Fe which resulted in an increased number of sites susceptible to acid attack (Johnston *et al.*, 2022a). Gridi-bennadji *et al.* (2008) described the dehydroxylation of muscovite as progressive, suggesting the gradual removal of hydroxyl groups over a spectrum of temperatures rather than at a precise temperature. Therefore, isomorphic Fe was accessed more rapidly in the interlayer of the dehydroxylated muscovite structure at lower calcination

temperatures than in the octahedral region of muscovite at higher calcination temperatures.

The Fe extraction percentages at 700 °C, 750 °C, and 800 °C were 62.6%, 59.1%, and 52.8%, respectively. Additionally, the further decrease in the Fe extraction trend above 650 °C was associated with the suppression of Fe because of the development of spinels at increased calcination temperatures (Johnston *et al.*, 2022a). Al-ajeel and Al-sindy (2006) found that calcination at 750 °C resulted in the formation of a minor recrystalline-phase aluminum silicate. Johnston *et al.* (2022a) found that the iron oxide components in low-quality kaolin transformed into an insoluble aluminum spinel phase at a calcination temperature of 750 °C, causing a decrease in the ability of acid to dissolve aluminum and iron. The migration of Fe ions into amorphous metakaolinite in the BL clay was more pronounced from 700 to 750 °C. Furthermore, the integration of Fe into the spinel structure effectively locks up Fe, preventing its dissolution during the formation of spinels and mullite (Lecomte-Nana *et al.*, 2013). Because Fe was bound before and during the formation of spinels, the dissolution of Fe was hindered.

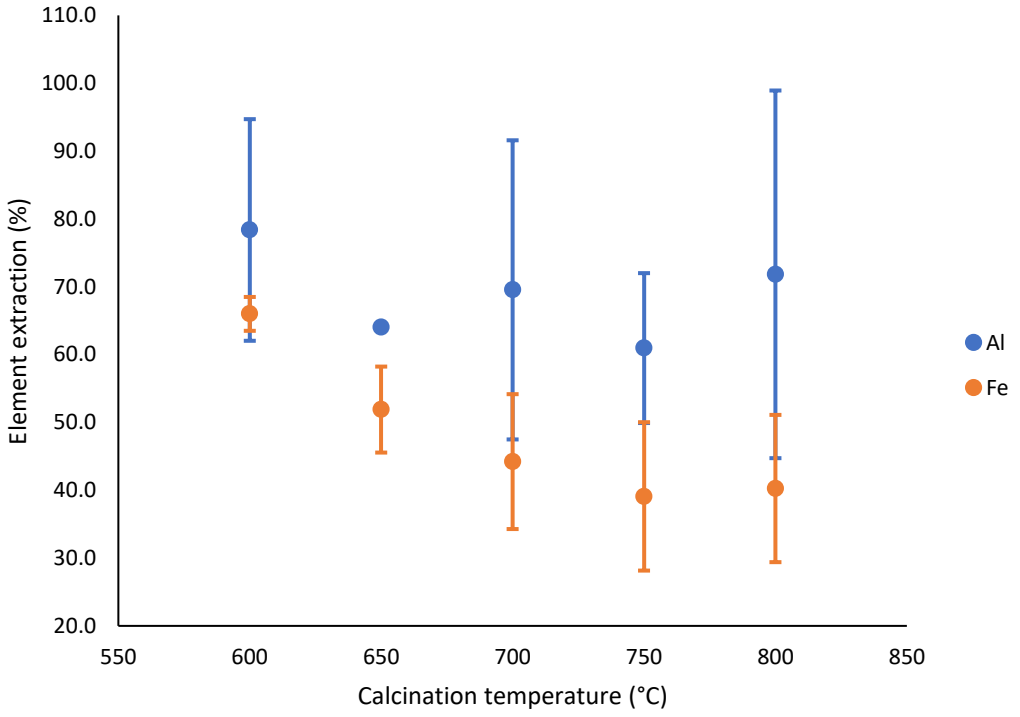

Figure 5.3: Al and Fe extraction percentages for calcined FL clays

The Al and Fe extraction of raw FL clay was 3.13 and 17.9%, respectively. Compared to BL clay (**Error! Reference source not found.**), the dissolution of Al from calcined FL clay exhibited a distinct leaching pattern (**Error! Reference source not found.**). The Al extraction percentage was observed as 78.4% at 600 °C because of the transformation of kaolinite to metakaolinite, decreased to 64.0% at 650 °C, followed by an unexpected increase of 69.5% at 700 °C, decrease of 61.0% at 750 °C, and increase of 71.8% 800 °C. The XRD (Figure 4.6) and IR (Figure 4.10) analyses indicated that the thermal dehydroxylation of the FL clay was complete at 600 °C, corresponding to higher Al dissolution. A similar trend was observed for the Fe extraction percentages at different calcination temperatures for FL clay and BL clay. However, the Fe extraction percentages for the FL clay were lower than those for the BL clay. The Fe extraction percentages for FL clays were 66.0% at 600°C, 51.9% at 650°C, 44.2% at 700 °C, 39.1% at 750°C, and 40.2% at 800 °C, showing a decreasing trend attributed to the Fe ions migration into the metakaolinite structure. In contrast, from the thermal behavior of the FL clay (Figure 4.3), a single area of mass loss was detected between 340 and 700 °C, which corresponded to the loss of structural hydroxyl groups. Additionally, it agreed with the major DTA peak resulting from thermal dehydroxylation. Consequently, no spinel formation was observed at temperatures exceeding 700 °C.

In comparison to the BL clay dissolution behaviour, the Al extraction for the FL clay did not decrease at 700 and 800 °C. As observed in the Fe observations of BL clay, the presence of iron oxide phases resulted in a reduction in the temperature necessary for the formation of spinel-mullite (Lecomte-Nana *et al.*, 2013). Nevertheless, the lower amounts of Fe in FL clay compared to BL clay in Appendix C (Table C 2 and Table C 1, respectively) prevented the formation of spinels, resulting in no observed decrease in Al, except at 650 °C and 750 °C. The effect of Fe ion migration into the metakaolinite structure was more pronounced at temperatures of 650 and 750 °C, where lower Al extraction percentages were observed. Additionally, it was speculated that Al coordination within the amorphous metakaolinite present at different calcination temperatures might have played a role in the observed oscillating Al extraction trend.

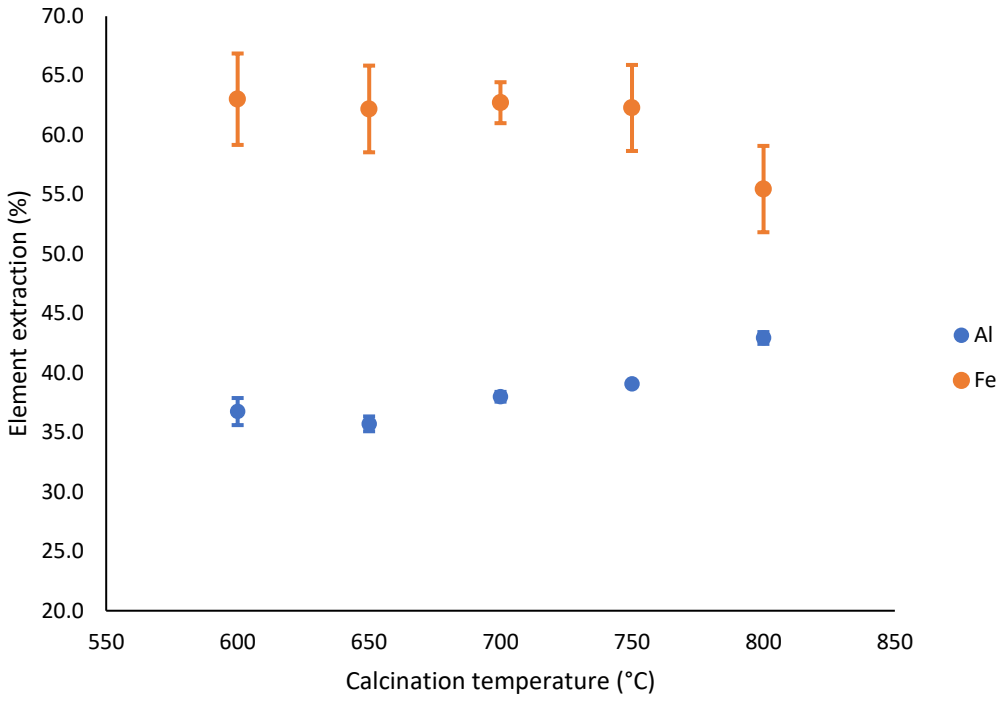

Figure 5.4: Al and Fe extraction percentages for calcined F clays

The Al extraction of raw F clay was 6.71%, while the Fe extraction of 36.7% was obtained. The leaching pattern of Al from F clay exhibited a distinct profile, in contrast to BL and FL clays (**Error! Reference source not found.**). The Al extraction percentages were relatively stable at 600 and 650 °C (36.7 and 35.7%, respectively), then increased with increasing calcination temperature from 700 to 800 °C (38.0% at 700 °C, 39.1% at 750 °C and 42.9% at 800 °C). The chemical analyses of raw F clay (Table 4.2) showed that the primary components of the clay were SiO_2, CaO, and Al_2O_3, while F_2O_3, K_2O, and MgO were present in lower concentrations. The XRD results (Figure 4.7) showed that at 600 °C, the basal reflections of kaolinite disappeared due to the reduced crystallinity resulting from the dehydroxylation of kaolinite (D'Elia *et al.*, 2018). Moreover, the increase in the Al concentration in F clay was attributed to the reactive amorphous phase from the dehydroxylation of kaolinite and smectite and the progressive dehydroxylation of muscovite. The IR analysis (Figure *4.11*) showed that calcination at 600°C was accountable for the complete dehydroxylation of kaolinite and smectite as evidenced by the disappearance of the OH stretching bands. Nevertheless, the IR

spectra showed no significant differences between most calcination temperatures, except for carbonates, where a notable difference was observed after 600 °C. However, the LOI values after calcination were higher at lower calcination temperatures and lower at higher calcination temperatures (Table *4.6*), suggesting that more structural water was released at higher temperatures, allowing high Al dissolution. Hence, Al extraction increased at higher calcination temperatures.

The Fe extraction percentages slightly decreased with increasing temperature from 600 to 650°C (63 and 62.2%, respectively), then slightly increased at 700°C to 62.7%, followed by a decrease to 62.3 and 58.0% at 750 and 800°C, respectively. The simultaneous dissolution of Al and Fe at each calcination temperature favored the dissolution of Fe, as indicated by the higher Fe extraction percentages than the Al extraction percentages. The Fe dissolution at all calcination temperatures was attributed to the rapid liberation of Fe from the interlayer of smectite because of ion exchange reactions (Etz et al., 2005). The decreasing Fe trend indicating the diffusion of Fe ions into metakaolinite network in preparation for formation of a spinel (Lecomte-Nana *et al.*, 2013), was not clearly observed in the F clays. Although F clay had a relatively low kaolinite content compared to BL and FL clays (Table 4.1), the Ca dissolution (**Error! Reference source not found.**) led to competition for the reaction with H^+ protons. At lower calcination temperatures, Ca dissolution resulted from the presence of dolomite and calcite, whereas at higher calcination temperatures, it was influenced by the products of dolomite and calcite decomposition.

Table 5.1: Al and Fe Selectivity ratios at different calcination temperatures for BL, FL, and F clay

Calcination temperature (°C)	BL clay	FL clay	F clay
600	1.17	1.19	0.583
650	1.04	1.23	0.606
700	1.05	1.57	0.627
750	1.08	1.56	0.627
800	1.23	1.78	0.774

The selectivity ratio in this context of Al extraction refers to the percentage of Al extracted to the percentage of Fe extracted. Table 5.1 provided a quantitative measure of the selective extraction of Al relative to Fe impurities during the acid leaching process. A higher selectivity ratio indicated that Al was more efficiently extracted than Fe, whereas a lower ratio suggested less efficient extraction of Al relative to Fe. The highest selectivity ratios were observed at 800°C (1.23) for BL clay, at 800°C (1.78) for FL clay, and at 800 °C (0.774) for F clay. The highest Al dissolution of 79.4% with Fe dissolution of 67.8% was noted for BL clay calcination at 600°C, whereas the highest Al dissolution of 78.4% with Fe dissolution of 66.0% was observed for FL clay calcination at 600 °C. When comparing these two clays, the lower calcination temperature for thermal treatment prior to Al extraction for BL and FL clay is beneficial from an energy utilization perspective. Both clays require less energy to transform kaolinite to amorphous metakaolinite during thermal treatment. However, this was associated with the higher Fe concentration in the leachate. Conversely, the higher calcination temperature for BL and FL clay thermal treatment (high energy requirement) prior to Al extraction results in a trade-off of moderate Fe content in the leachate solution (Al extraction of 65.2% and Fe extraction of 52.8% for BL at 800°C, while FL clay achieved Al extraction of 71.8% with Fe extraction of 40.2%). Both observations have implications for the downstream processing and production of high-purity alumina.

After leaching, the intermediate compound (aluminum chloride) is formed from the dissolved Al in the leachates, which is then calcined to yield alumina (Pepper *et al.*, 2021). Nevertheless, kaolin feeds with low iron content are usually preferred because of the challenges linked to the separation of Fe impurities in the intermediate and alumina products (Pepper *et al.*, 2021). The vital aspect of these processes is obtaining high-purity salts at a low processing cost. Aly et al, (2019) demonstrated that kaolin clay with Fe_2O_3 composition of 1.19% required three stage purification process to increase the purity of hexahydrate crystals to 99.961%. Meanwhile, Pepper et al. (2021b) demonstrated that kaolin clay with Fe_2O_3 composition of 19.0 % also required three stage crystallization process of aluminum chloride, which yielded >99.99% Al_2O_3. Another study by Pak et al, (2019) used

two stage crystallization of aluminum chloride hexahydrate from kaolin clay with Fe_2O_3 composition of 6.14 % to produce 99.7% Al_2O_3. The raw BL and FL clays contained Fe_2O_3 composition of 0.706% and 0.524%, respectively. Therefore, if both BL and FL clays are used as raw materials for HPA production, the effect of high Fe content extraction on the comprehensive quality of the end HPA product would not be substantial. Furthermore, either clays calcined at 600 °C or 800 °C could be used as feedstock to produce HPA. However, the calcined clay which required a minimum amount of energy in the pretreatment step (i.e., calcination) prior to leaching would be selected.

To determine whether there is a significant difference in Al and Fe leaching results between calcined BL clay and FL clay, a statistical analysis was conducted using the student's t-test.

Null Hypothesis (H_0): No significant difference exists in Al and Fe leaching results between calcined BL clay and FL clay.

Alternative Hypothesis (H_1): A significant difference exists in Al and Fe leaching results between calcined BL clay and FL clay.

The leaching results for calcined BL and FL clays were assumed to follow a normal distribution. Measurements of Al and Fe leaching were taken at five different calcination temperatures.

For Al leaching results, the mean values for calcined BL clay and FL clay were 68.8 and 68.9, respectively, with standard deviations of 6.36 and 6.81. For Fe leaching results, the mean values for calcined BL clay and FL clay were 61.8 and 48.3, with standard deviations of 6.17 and 11.1, respectively. The student's t-test calculations were performed in Microsoft Excel using Equation 5.2, with a significance level set

$$t = \frac{X_1 - X_2}{\sqrt{\frac{s_1^2}{n_1} + \frac{s_2^2}{n_2}}} \qquad 5.2$$

X_1 and X_2 are the clay sample means,

S_1^2 and S_2^2 are the variances,

N_1 and N_2 are the sample sizes

The t-test for Al leaching results yielded a t-value of 2.306 with 8 degrees of freedom, resulting in a p-value of 0.9761. This p-value was well above the 0.05 significance level, indicating a very high likelihood that any observed difference in Al leaching results was due to random chance. For Fe leaching results, the t-test yielded a t-value of 2.447 with 6 degrees of freedom and a p-value of 0.05387. This p-value was close to but slightly above the 0.05 threshold. Since it did not meet the 5% significance level, there was insufficient evidence to reject the null hypothesis.

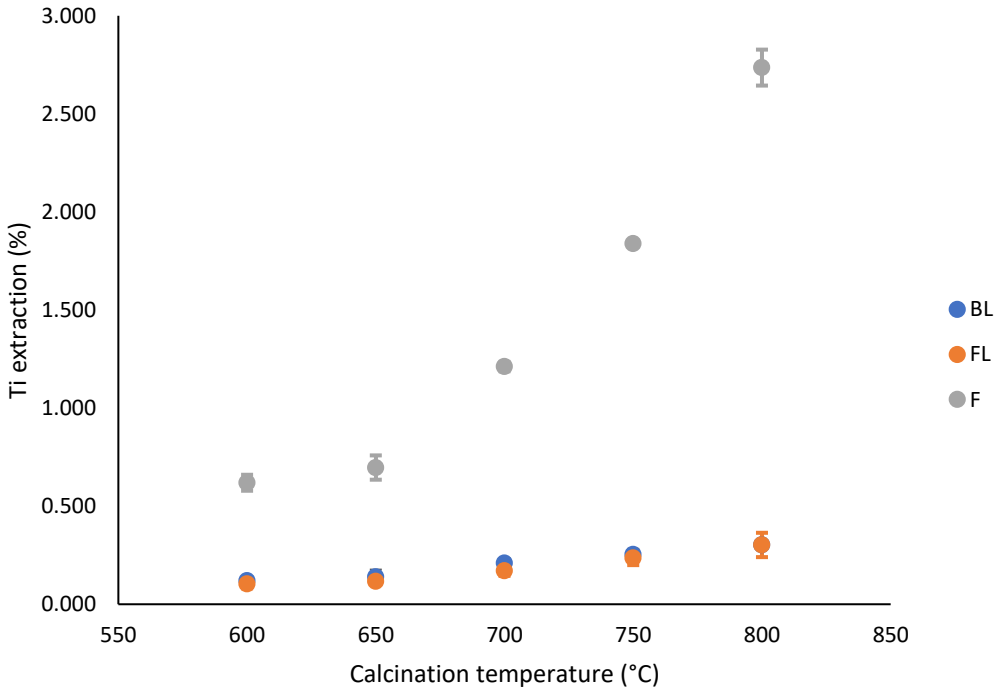

Figure 5.5: Ti extraction percentages at different calcination temperatures for BL, FL, and F clay

The amount of Ti dissolved from kaolinite thermally treated at different calcination temperatures did not exceed 0.5 % for BL and FL clays (**Error! Reference source not found.**), signifying that the calcination of kaolinite did not influence the release

of Ti into the acid solution. Anatase in the raw clay may initially be associated with kaolinite surfaces at the nanometric level (Fabbri et al., 2013). Fabbri et al. (2013) further stated that changes in crystal size and structure of kaolinite during calcination affect the surface properties of anatase, potentially altering its affinity for metakaolinite. The leaching process selectively removed Ti, allowing for the isolation and extraction of anatase from the kaolinite matrix. Notably, titanium can be obtained from muscovite due to replacement of octahedral Al^{3+} by Ti^{4+} (Lu et al., 2020). An increasing trend in the dissolution of Ti was observed in all clays, with a more noticeable increase in the F clay. This increase was attributed to the dissolution of Ti associated with kaolinite surfaces and the dissolution of isomorphic Ti due to the dehydroxylation of muscovite as the calcination temperature increased. Although an increase in Ti dissolution was observed in the leachate, it was not comparable to the amount of Ti retained in the leached residue (Table 5.6, Table 5.7, and Table 5.8).

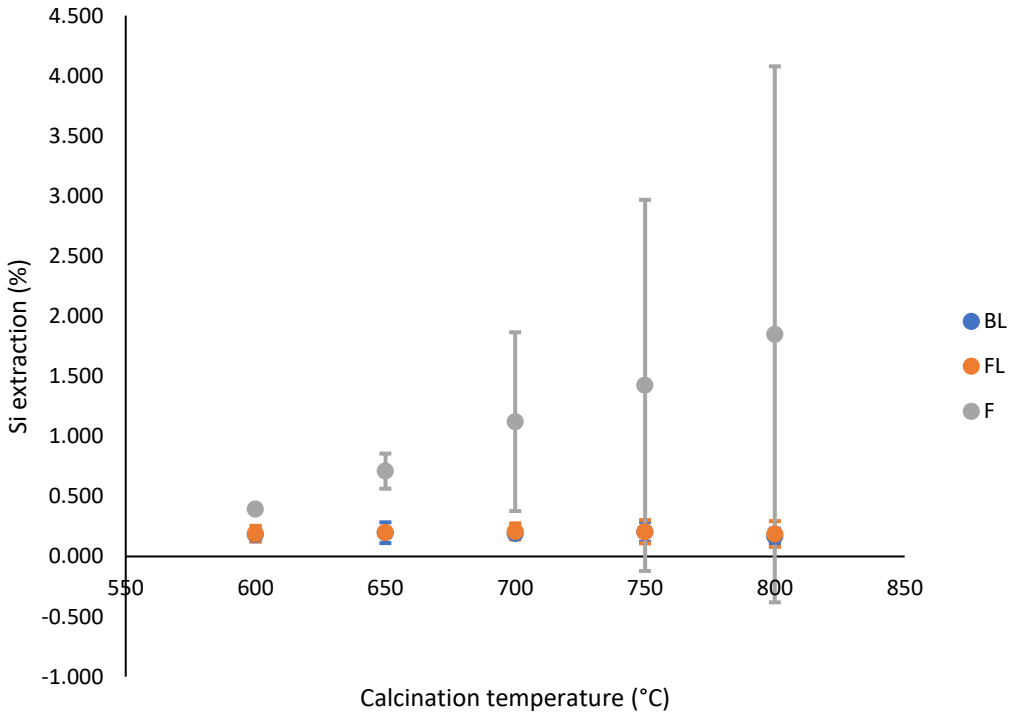

Figure 5.6: Si extraction percentages at different calcination temperatures for BL, FL, and F clay

Error! Reference source not found. depicts that the amount of Si dissolved from kaolinite thermally treated at different calcination temperatures did not exceed 0.25% for the BL and FL clays, signifying that the calcination of kaolinite did not influence the release of Si into the acid solution. Si was mainly distributed in silicate minerals, such as (amorphous content, muscovite) and quartz. Al-Harahsheh *et al.*, (2023) reported that hydrochloric acid causes the partial breakdown of an aluminosilicate framework releasing silicon into the solution, and the released silicon undergoes polymerization to form silica particles. As a result, a high Si content was reported in the leached residue. Nevertheless, the Si extraction percentages for BL and FL clays were relatively equal at all calcination temperatures, except for Si dissolution at 750 °C, where BL clay had a high amount of 0.204% and FL clay had the least Si dissolution of 0.187% at 800°C. Moreover, F clay also reported the highest Si extraction of 1.85% at 800 °C. The Si extraction for the F clay increased from 600 °C (0.409%), reaching the highest peak at 650 °C, followed by a gradual decrease in Si extraction up to 800 °C. Furthermore, F clay reported higher Si extraction percentages at all calcination temperatures than BL and FL clays.

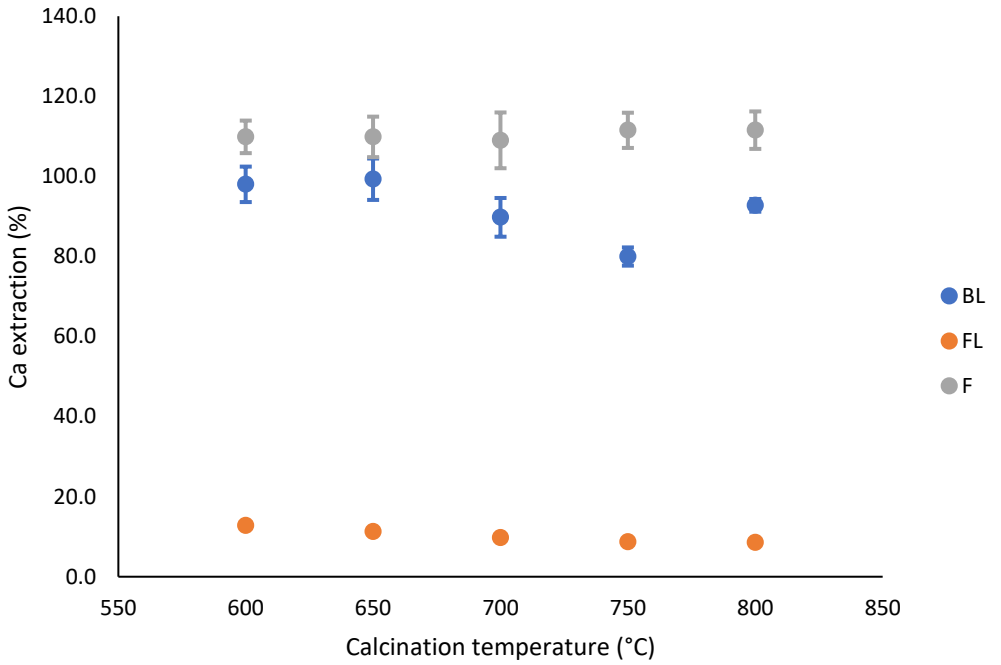

Figure 5.7: Ca extraction percentages at different calcination temperatures for BL, FL, and F clay

Error! Reference source not found. shows the Ca extraction percentages of calcined BL, FL, and F clays at calcination temperatures between 600 and 800 °C. The order of Ca extraction percentage was F> BL> FL clay. Furthermore, the Ca extractions for calcined F clays were over 100%, suggesting that almost all the Ca from the calcined clays leached into the acid solution at all calcination temperatures. The raw F clay contained both calcite and dolomite (Table 4.1). However, only dolomite partially decomposed to calcite and periclase at 600 and 650 °C adding to the amount of calcite present at these temperatures (Table *4.5*). In addition, dolomite fully decomposed to calcite and periclase, and calcite almost completely decomposed to free lime and released carbon dioxide gas. However, the presence of lime was not observed. The absence of free lime suggested that CaO reacted with aluminum silicates forming amorphous metastable phases (Allegretta et al, 2016). Overmann et al, (2024) stated that CaO can form granular deposits on metakolinite as a probable amorphous transition state between metakaolinite and free lime before recrystallization process of the Ca-containing phase. Therefore, the Ca dissolution of F clay was associated with dolomite, calcite and amorphous smectite at

calcination temperatures between 600 and 650 °C. At temperatures above 700 °C, Ca dissolution was attributed to the reactivity of calcite, free lime, amorphous Ca metastable phases, and amorphous smectite. Although Ca extraction was related to the different Ca-containing mineral phases at different calcination temperatures, high Ca dissolution was observed at all calcination temperatures.

The Ca extraction percentage for BL clay slightly increased from 98% at 600 °C to the highest peak of 99% at 650 °C, and then gradually decreased to 89.8% at 700 °C and 80% at 750 °C. However, the Ca dissolution increased to 92.8% at 800 °C. The Ca dissolution at 600 and 650 °C was attributed to the reactivity of dolomite, and Ca dissolution at 700 °C was associated with the presence of dolomite and calcite. At higher calcination temperatures (750 and 800 °C), Ca dissolution was ascribed to the formation of Ca-containing metastable phases. Hence, the transformation of dolomite and calcite to amorphous metastable phases reduced Ca dissolution at higher calcination temperatures. Trindade *et al*. (2009) suggested that the reaction of calcite, lime, periclase, quartz, and aluminum silicates in certain cases with clay minerals led to the formation of metastable calcium and/or magnesium phases due to the presence of iron levels in the raw clay. Cultrone and Rosua (2020) suggested that when clay minerals decompose, a portion of the iron within them is oxidized to form FeO, a highly reactive component that plays a significant role in solid-state reactions. Furthermore, according to Maniatis *et al.* (1983), in the calcareous clays, the initial clay minerals degrade rapidly, followed by the formation of calcium aluminosilicates that trap ferric ions. This results in iron being transported directly into the emerging phases present within the calcareous clays. In contrast, the increased Ca extraction at 800 °C was associated with the highly disorganized structure of muscovite, which released the isomorphic Ca^{2+} to the acid solution.

However, the lowest Ca dissolution was seen for FL clay compared to BL and F clays. Moreover, Ca dissolution in FL clay gradually decreased with increasing calcination temperature. In addition, the Ca dissolution observed at 600, 650, 700, 750, and 800 °C was 12.8, 11.2, 9.4, 8.6, and 8.5%, respectively. Furthermore, the Ca dissolution of FL clay was associated with the presence of dolomite at lower calcination temperatures and from 700 to 800°C, which was attributed to the

presence of dolomite and transitional calcite formed from the partial decomposition of dolomite. The dissolution of Ca at higher temperatures (800 °C) was associated to the presence of metastable Ca-containing phases formed from the decomposition of dolomite and transitional calcite. These phases contained fewer Ca ions in their structures.

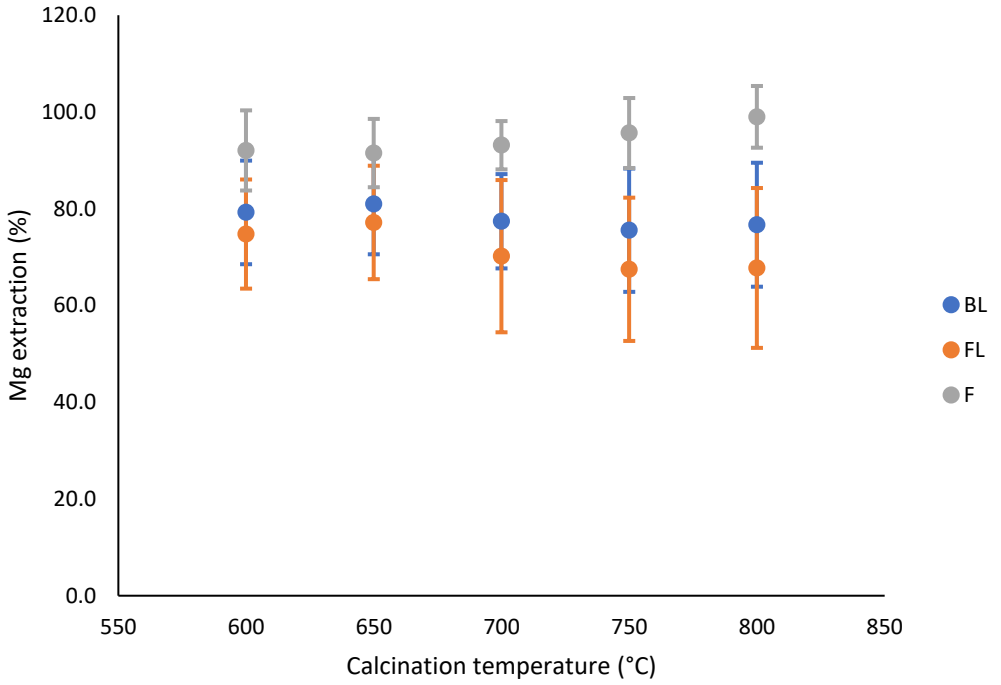

Figure 5.8: Mg extraction percentages at different calcination temperatures for BL, FL, and F clay

Error! Reference source not found. depict Mg extraction of over 70%, and the Mg dissolution was observed in the order F>BL>FL clay. Additionally, the Mg extraction slightly increased from 600 to 650°C, then a gradual reduction to 700 and 750°C, and a slight increase in Mg extraction at 800 °C for both BL and FL clays. Meanwhile, the Mg extraction increased with increasing calcination temperature for F clay. The increase in Mg extraction for BL and FL clays at lower calcination temperatures was associated with dissolution of dolomite and isomorphic Mg substitution in the formed cordierite phase. Meanwhile, a decrease in Mg extraction indicated a reduced dissolution of dolomite, periclase, and Mg-containing metastable phases formed at higher calcination temperatures. Even

though there were slight changes in Mg extraction, the Mg dissolution of BL clay was relatively stable across various calcination temperatures. The gradual increase in Mg extraction with increasing calcination temperature for F clay is attributed to the gradual release of Mg cations from the smectite interlayer.

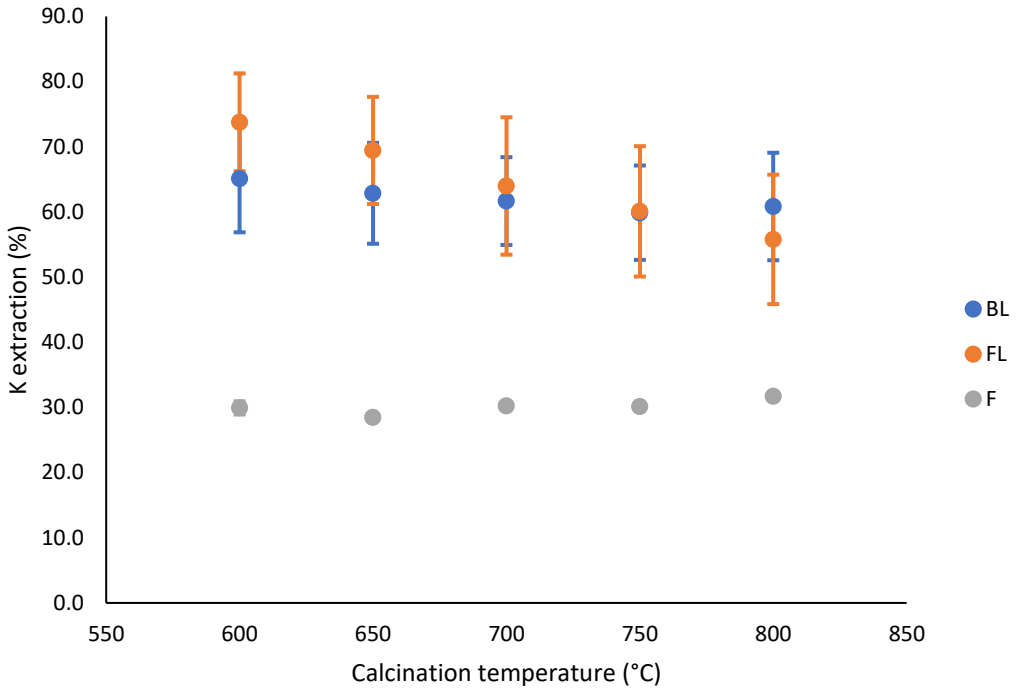

Figure 5.9: K extraction percentages at different calcination temperatures for BL, FL, and F clay

An inversely linear relationship between calcination temperature and K dissolution for BL and FL clay is shown in **Error! Reference source not found.**, characterized by a gradual decrease in solubility with increasing calcination temperature. The K ions dominated in the interlayer of muscovite. The K extraction percentages for F clay were relatively stable at various calcination temperatures. Furthermore, the observed K extraction order among the three different clays was FL >BL > F clay. The K extraction percentages for BL and FL clays were over 55%, whereas the K extraction percentages for F clay were less than 33% across various calcination temperatures. The reason for the decrease in K extraction was the higher potassium adsorption and absorption, which resulted in a reduction of potassium in the solution. The formation of the smectite phase was due to the precise matching of potassium ions with the hollow space within pseudohexagonal rings of oxygen in

the neighboring silica tetrahedral sheet of muscovite (Danner *et al.,* 2018). The presence of smectite in F clay appeared to have prevented the dissolution of K from occurring within the muscovite structure and, instead, caused the isomorphic cation to be released from the smectite.

Table 5.2 show the BL, FL, and F clays with the highest Al dissolution and impurity dissolution. The order of impurity dissolution for BL clay was Ca > Mg > Fe > K > Si >Ti, whereas for FL clay, the order was Mg > K > Fe > Ca > Si > Ti. Furthermore, the order observed for the F clay was Ca > Mg > Fe > K > Ti > Si.

Table 5.2: Comparison between BL, FL, and F clays with highest Al extraction

Extracted ion	BL 600	FL600	F800
	%		
Al	79.4	78.4	42.9
Fe	67.8	66	55.5
Ti	0.120	0.105	2.74
Si	0.184	0.190	1.848
Ca	98	12.8	111.5
Mg	79.2	74.8	99
K	65.1	73.8	31.7

The order of dissolution may have reflected the sequence in which the minerals in the calcined clays broke down under acidic conditions. Quartz is primarily comprised of SiO_2, which is largely insoluble in HCl; therefore, the dissolution of Si from quartz was minimal in this environment compared to the dissolution of other elements. Additionally, anatase is generally insoluble in HCl, so Ti dissolution from anatase was minimal compared to the dissolution of other elements. The dissolution of potassium from partially dehydroxylated muscovite was slower in calcined BL and F clays, whereas it was moderately fast in calcined FL clay. This suggested removal of hydroxyl groups in the muscovite structure occurred faster in FL clay, resulting in increased porosity, which enhanced the accessibility of HCl to the K ions within the mineral, potentially accelerating

dissolution. Dissolution of Fe varied depending on the mineral form in the clay. In this case, Fe existed as iron oxides in the calcined clays. Dolomite (Ca- and Mg-containing minerals) readily dissolved in HCl acid solution because of the ability of the acid to react with carbonates. Compared to calcined BL and F clays, the minimal Ca dissolution from calcined FL clay suggested that the product formed from decomposition of CaO was probably bound into structures of new crystalline phases developing at 800 °C (Dabare and Svinka, 2013). Additionally, calcined FL clay may have contained periclase that had calcium impurities with relatively lower solubility of calcium compounds. Hence, a slower Ca dissolution occurred.

Overall, as indicated by the extraction results, when the calcination temperature surpassed the dehydroxylation domain of kaolinite, most impurities diffused into the poorly ordered metakaolinite during the structural reorganization process. This phenomenon was more pronounced in the BL clay than in the FL clay. Consequently, Al extraction was reduced because Al was closed within the newly formed insoluble structures.

5.1.2. Mineralogical composition of leached residue

The HCl leaching process for calcined clay effectively dissolves alumina while leaving silica intact in the dehydroxylated amorphous aluminosilicate phases (Tantawy and Alomari, 2019). The H^+ ions interact with the Al-O bonds, substituting the ions Al^{3+}, while unstable orthosilicic acid groups $Si(OH)_4$ or H_4SiO_4, are formed in hot acid solutions (Barry *et al.*, 2019). The leached residues from BL, FL, and F clay were rich in SiO_2 from quartz and amorphous SiO_2 in smectite and amorphous content. The results are presented in Table 5.3, Table 5.4, and Table 5.5. This silica-rich residue can be utilized as SiO_2 source for the production of zeolites (Rahayu *et al.*, 2019). Moreover, these residues have potential applications as construction materials (Pak *et al.*, 2019).

Table 5.3: Mineralogical composition of BL leached residue

°C	Quartz	Anatase	Smectite	Muscovite	Amorphous
600	17.1	0.71	5.7	0	76.49

650	15.18	0.71	5.42	0	78.68
700	16.77	0.82	3.41	0	79
750	15.2	0.74	6.35	0	77.71
800	13.79	0.75	5.17	0	80.29

Table 5.3 showed that the solid residue after acid leaching was enriched with quartz and anatase when all the calcined BL samples were observed at different temperatures. The presence of quartz and anatase confirmed that less silicon dioxide and titanium dioxide dissolved during the hydrochloric acid leaching. Smectite appeared as a new phase after acid leaching at all the calcination temperatures. The appearance of smectite in the leached clay was noteworthy, as smectite minerals often contain aluminum. Besselink *et al.*, (2020) described a mechanism of Mg-rich trioctahedral smectite crystallization from amorphous intermediate. The two-stage process of mechanistic pathways involved rapid co-precipitation, during which available Mg was incorporated into an aluminosilicate network, and a much slower crystallization mechanism, during which the remaining Mg gradually became integrated into the developing smectite sheet structure. This process occurred when Mg^{2+} was incorporated into amorphous metakaolinite, resulting in the crystallization of smectite. Some Al^{3+} from amorphous metakaolinite dissolved, others rearranged into octahedral coordination, and others remained in tetrahedral coordination during acid leaching (Besselink *et al.*, 2020). The formation of Mg-smectite contributed to the Al content observed after acid leaching (Table 5.6).

Another way for the formation of smectite involves the perfect fitting of potassium ions (with a radius of 1.38 Å) within the cavities of the pseudohexagonal rings of oxygen in the adjacent silica tetrahedral sheets of muscovite.(Danner *et al.*, 2018). Muscovite and traces of cordierite completely disappeared at all calcination temperatures after acid leaching. The disappearance of muscovite was attributed to the dissolution of Al and interlayer cations and the formation of smectite. The amorphous phase in the leached residue increased with elevated calcination temperature, indicating a gradual reduction in leachability of the element.

Table 5.4: Mineralogical composition of FL leached residue

°C	Quartz	Anatase	Smectite	Muscovite	Amorphous
600	4.22	0.67	2.77	0	92.34
650	4.68	0.62	3.47	0	91.23
700	4.57	0.76	3.36	0	91.31
750	5.3	0.66	3.12	0	90.92
800	4.92	0.66	3.1	0	91.32

The mineralogical content of the FL leached residue is similar to that of the BL clay, with differences in the relative mineral amounts presented in Table 5.4. Muscovite vanished in the residue, smectite formed as a new phase, and quartz and anatase were present in the leached residue.

Table 5.5: Mineralogical composition of F leached residue

°C	Quartz	Anatase	Smectite	Muscovite	Amorphous
600	45.55	0.08	4.59	4.27	45.51
650	49.27	0	5.61	4.89	40.23
700	50.74	0.09	3.07	4.24	41.87
750	49.02	0.11	2.31	3.54	45.02
800	50.46	0.1	4.12	4.24	41.09

The F clay residue followed the same mineralogical trend as the BL and FL clays with different relative contents, except that the muscovite structure was not completely dissolved in the acidic solution (Table 5.5). This suggested that since smectite was present in the F clay, potassium in the solution could not diffuse into the tetrahedral sheet of muscovite to form more smectite, resulting in an increase in K ions in the solution. Anatase appeared in the residue, whereas it was absent in the calcined F clays.

5.1.3. Chemical compositions of leached residues

The Al_2O_3 content after leaching was between 10-16% in all clays at different calcination temperatures for BL, FL, and F clays. The BL and FL clays reported more TiO_2 than the F clay, whereas the F clay contained more Fe_2O_3 and K_2O.

Table 5.6: Chemical composition of BL leached residue

BL chemical composition (%)								
°C	Fe_2O_3	SiO_2	Al_2O_3	K_2O	CaO	MgO	TiO_2	LOI
600	0.311	77.7	10.2	0.139	0.09	<0.01	2.13	9.48
650	0.328	78.1	11.5	0.166	0.11	<0.01	2.18	7.58
700	0.352	77.9	12.1	0.176	0.131	<0.01	2.17	7.12
750	0.358	75.9	13.8	0.197	0.16	<0.01	2.10	7.08
800	0.438	76.4	13.5	0.212	0.172	<0.01	2.12	6.49

Table 5.6 highlights the oxide composition of the leached residue. The SiO_2 content in calcined clays increased from 56.3-57% (Table C 1) to 75.9-78.1% in the leached residue. In contrast, the Al_2O_3 content dropped from 37-38.1% to 10.2-13.8%. Additionally, the TiO_2 content increased from 1.58-1.60% in the calcined clays to 2.1-2.18% in the leached residue.

Table 5.7: Chemical composition of FL leached residue

FL chemical composition (%)								
°C	Fe_2O_3	SiO_2	Al_2O_3	K_2O	CaO	MgO	TiO_2	LOI
600	0.343	76.9	10.9	0.19	0.037	<0.01	1.99	9.23
650	0.378	75.0	13.6	0.216	0.04	<0.01	1.93	8.96
700	0.407	73.1	14.9	0.23	0.05	<0.01	1.88	8.885
750	0.441	73.3	15.4	0.256	0.055	<0.01	1.87	8.128
800	0.411	74.2	14.7	0.265	0.056	<0.01	1.86	7.801

The SiO_2 level in calcined FL clays initially ranged between 53.3% and 53.9% but increased to between 73.1% and 76.9% in the leached residue (Table 5.7). Meanwhile, the Al_2O_3 content decreased from 41.2%-42.4% to 10.9%-15.4%. The TiO_2 content, on the other hand, increased from 1.37% to 1.39% in the calcined clays to 1.86% to 1.99% in the leached residue.

Table 5.8: Chemical composition of F leached residue

F chemical composition (%)								
°C	Fe_2O_3	SiO_2	Al_2O_3	K_2O	CaO	MgO	TiO_2	LOI
600	1.16	79.8	11.5	1.93	0.218	0.456	0.798	4.42
650	1.20	79.9	11.2	1.94	0.235	0.44	0.794	4.09
700	1.19	80.7	11.2	1.95	0.232	0.403	0.799	3.75
750	1.20	80.3	11.1	1.98	0.252	0.368	0.792	3.81
800	1.44	81.1	10.5	1.96	0.269	0.274	0.795	3.73

The data in Table 5.8 displayed that the percentage of SiO_2 in calcined F clays increased from 58-63.2% to between 79.8-81.1% in the leached residue. At the same time, the percentage of Al_2O_3 decreased from 13.5-14.7% to 10.5-11.5%. This small difference confirmed that the amorphous metakaolinite in the F clays was not efficiently leached to remove Al from the clay to the acid solution. Additionally, the percentage of TiO_2 increased from 0.586-0.636% in the calcined clays to 0.794-0.799% in the leached residue.

5.2. Experimental design and statistical analysis

This study evaluated the impact of leaching factors such as acid concentration, temperature, duration, and solid-to-liquid ratio on the dissolution of Al. Design Expect software (version 13 trial version) was used to analyze the statistically significant factors and their interactions to optimize the recovery of Al.

5.2.1. Statistical study of Al leaching recovery

The objective of this study was to examine the impact of leaching conditions on Al extraction. Additionally, samples BL800, FL700, and F600 were used for statistical analysis. The results of Al extraction from the experimental runs for the 2^3 full factorial design are presented in Table 5.9 for the BL clay. Furthermore, the outcomes of Al extraction from the experimental runs for the 2^4 full factorial design are provided in

Table *5.10* and

Table *5.11*, along with the actual and coded values. A 2^3 full factorial design was conducted for BL clay owing to running out of BL clay. Eight experiments were performed using the values of variables A, B, and C, and the alumina extraction percentage was calculated for BL clay (Table 5.9). Moreover, 16 additional experiments were conducted using the values of variables A, B, C, and D, and the alumina extraction percentage was determined for the FL and F clays (

Table *5.10* and

Table *5.11*, respectively). The actual factor levels coded as the values of (-1) and (+1) are as follows: A (acid concentration); 3M (-1) and 5M (+1); B (leaching temperature): 50°C (-1) and 90°C (+1); C (leaching time): 2 h (-1) and 4 h (+1); D (solid/liquid ratio): 0.05 g/ml (-1) and 0.15 g/ml (+1).

The primary goal of this DOE (Design of Experiments) was to explore how various factors interact and affect extraction efficiency, aiming to identify the most promising factor combinations for maximizing aluminum extraction. By conducting a single set of unique experimental conditions without replication, the study was able to cover a broader experimental space, providing a clearer understanding of which factors had the most significant impact on aluminum extraction. The decision to forego replication was influenced by the need to allocate resources efficiently and adhere to project time constraints. Modern statistical tools were employed to compensate for the absence of replication. Techniques such as analysis of variance (ANOVA) allowed for meaningful analysis of unreplicated

designs by estimating the effects of different factors and their interactions. Software used in DOE analysis, such as Design-Expert, includes algorithms that adjust for the lack of replication by modeling variability through factor interactions or higher-order terms. As a result, meaningful conclusions could still be drawn, despite the absence of replicated runs. This set of experiments provided sufficient data to identify trends and determine which conditions were most effective for aluminum extraction.

Table 5.9: Al extraction results for 2^3 full factorial design for BL clay

Random Run Order	Standard Run order	Control Factors			Al extraction (%)
		A	B	C	
7	1	-1	+1	+1	43.6
6	2	+1	-1	+1	19.8
4	3	+1	+1	-1	42.5
1	4	-1	-1	-1	29.6
3	5	-1	+1	-1	41.8
2	6	+1	-1	-1	24.8
5	7	-1	-1	+1	19.4
8	8	+1	+1	+1	47.3

Table 5.10: Al extraction results for the 2^4 full factorial design for FL clay

Random Run Order	Standard Run order	Control Factors				Al extraction (%)
		A	B	C	D	
6	1	+1	+1	+1	-1	16.8
9	2	-1	-1	-1	+1	9.5
14	3	+1	+1	+1	+1	16.3
2	4	+1	-1	-1	-1	22.9
5	5	-1	+1	+1	-1	12.9
16	6	+1	+1	+1	+1	100
4	7	+1	-1	-1	-1	58.2
8	8	+1	+1	+1	-1	61.6
13	9	-1	+1	+1	+1	15.3
10	10	+1	-1	-1	+1	14.5
12	11	+1	-1	-1	+1	98.8

3	12	-1	-1	-1	-1	56.9
1	13	-1	-1	-1	-1	13.1
15	14	-1	+1	+1	+1	83.2
11	15	-1	-1	-1	+1	85.8
7	16	-1	+1	+1	-1	59.5

Table 5.11: Al extraction results for the 2^4 full factorial design for F clay

Random Run Order	Standard Run order	Control Factors				Al extraction (%)
		A	B	C	D	
12	1	+1	+1	-1	+1	60.9
3	2	-1	+1	-1	-1	20.6
9	3	-1	-1	-1	+1	39.2
2	4	+1	-1	-1	-1	15.8
6	5	+1	-1	+1	-1	16.4
16	6	+1	+1	+1	+1	68.8
4	7	+1	+1	-1	-1	20.1
5	8	-1	-1	+1	-1	16.0
15	9	-1	+1	+1	+1	56.9
13	10	-1	-1	+1	+1	35.6
7	11	-1	+1	+1	-1	23.2
1	12	-1	-1	-1	-1	15.7
10	13	+1	-1	-1	+1	31.7

11	14	-1	+1	-1	+1	54.1
14	15	+1	-1	+1	+1	41.1
8	16	+1	+1	+1	-1	22.5

The experimental data given in Table 5.9,

Table *5.10* and

Table *5.11* were used to estimate the main and interactional effects presented in Figure 5.10, Figure 5.11, and Figure 5.12, respectively. The following list serves as a guide for understanding these figures.

- *A – acid concentration*
- *B – leaching temperature*
- *C – leaching time*

- *D – solid/liquid ratio*
- *Interactive effects: AB, AC, AD, BC, BD, CD, ABC, ABD, ACD, BCD, ABCD*
- *Limit value as the vertical line across the bar graphs*
- *Non-significant value as indicated by Bar graph not crossing the limit value line*
- *Significant value as indicated by the Bar graph crossing beyond the limit value line*
- *Blue bar graph shows a negative effect*
- *Orange bar graph shows a positive effect*

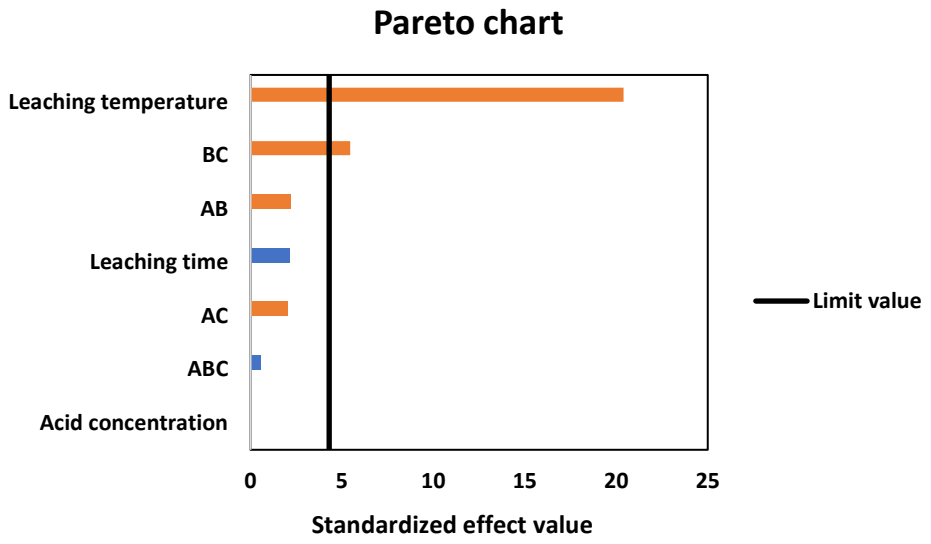

Figure 5.10: Pareto diagram illustrating significance of main and interactive effects for BL clay

The Pareto diagram in Figure *5.10* highlighted which factors had the most influence on leaching efficiency in BL clay. In this case, the factors of leaching temperature and the BC interaction were statistically significant because their bars on the chart exceeded the threshold line, indicating a strong effect on the response variable. This suggested that these factors contributed substantially to the variability in leaching efficiency and are likely key drivers in the leaching process. On the other hand, while leaching time and acid concentration did not exceed the significance threshold, they still showed a negative effect on leaching efficiency. This means

that although these factors influenced the process, their impact was not strong enough to be statistically significant. The lower influence of these factors could be due to a limited effect within the specific experimental range or because they interacted with other variables in ways that did not produce a noticeable independent impact on the leaching outcome.

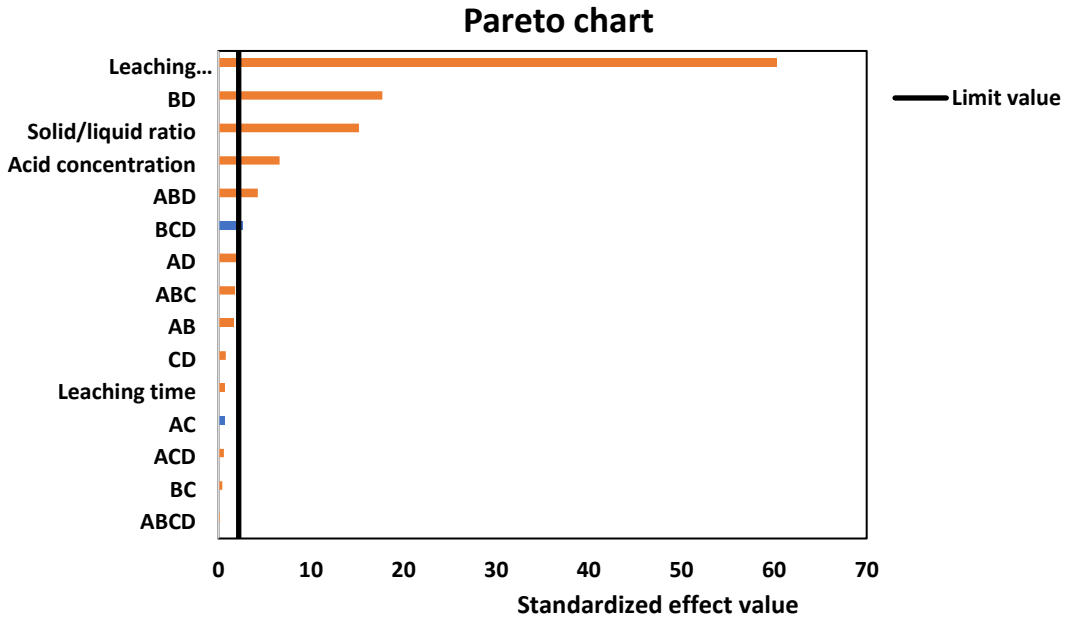

Figure 5.11: Pareto diagram illustrating significance of main and interactive effects for FL clay

The Pareto diagram for FL clay (Figure 5.11) indicated that the solid/liquid ratio, leaching temperature, and acid concentration were statistically significant because they exceeded the limit. Furthermore, the chart shows that the interactions between BD, ABD, and BCD were significant. Nevertheless, the leaching time was not statistically significant because the bar graph was below the limit. Although statistically significant, the BCD interaction had a detrimental effect on the aluminum extraction process owing to its negative effect.

The temperature at which the Al dissolution occurred in the clay was significantly influenced by the leaching process. Higher temperatures promote diffusion, increase the likelihood of reactant collisions, and provided extra thermal energy to overcome energy barriers (Udochukwu *et al.*, 2019a). At elevated leaching temperatures, the rate at which $Al(OH)^{3-X}$ and H^{+} species move through the

depleted layer and enter porous pockets is accelerated (Nnanwube and Onukwuli, 2023). Acid concentration exerted a crucial influence on the dissolution of Al from the clay. In acidic conditions, the proton-promoted mechanism dictated the dissolution rate by disrupting Al-O bonds and forming $AlOH_2^+$ groups (Bagani *et al.*, 2021). The dissolution rate of several minerals, including kaolin, varied with pH and was proportional to the fractional power of the hydrogen ion activity within specific ranges. Thus, the use of higher HCl concentrations, and consequently, greater hydrogen ion concentrations, correlated with a higher dissolution rate (Bagani *et al.*, 2021).

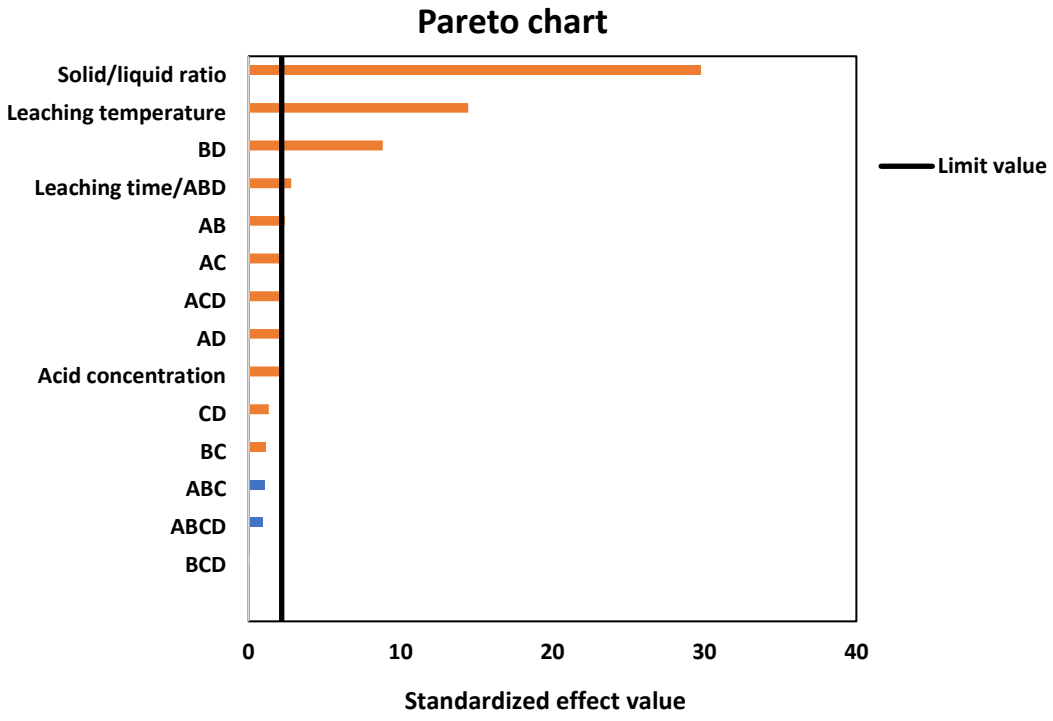

Figure 5.12: Pareto diagram illustrating significance of main and interactive effects for F clay

The Pareto diagram for F clay in Figure 5.12 showed that the solid/liquid ratio, leaching temperature, and leaching time were statistically significant because they exceeded the threshold value. Moreover, the BC and ABD interactions were found to be statistically significant. The other interactions were not statistically significant because they were below this limit.

5.2.2. Normal probability plot of effects

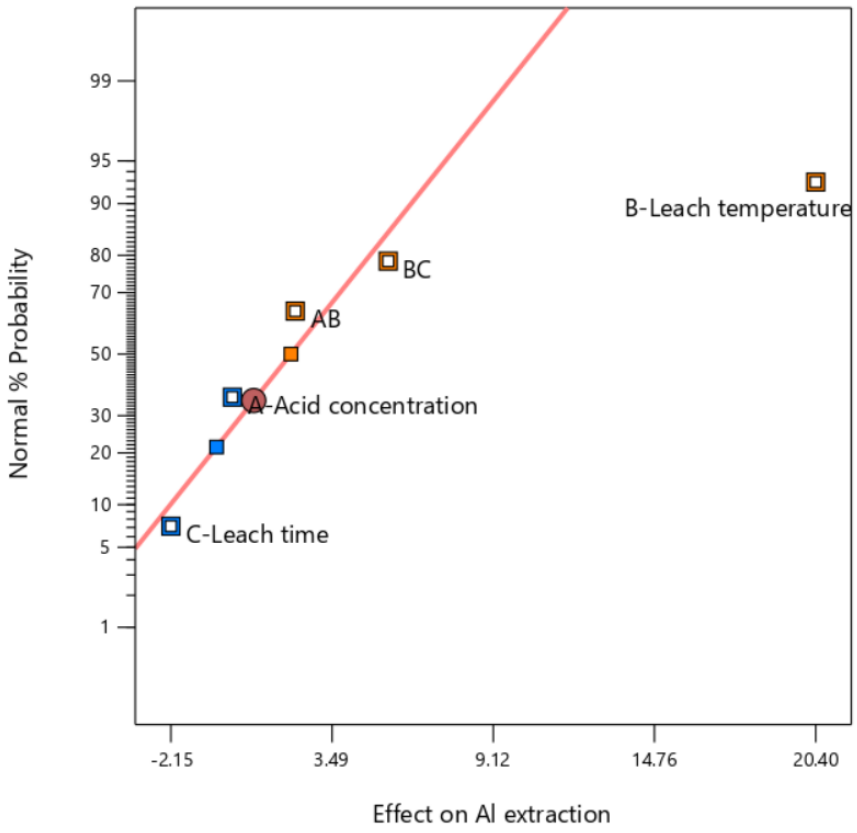

Figure 5.13: Graphical representation displaying effects of the main factors and factor interactions for BL clay

Figure 5.13 shows that in the leaching of BL clay, the leaching temperature and BC interactions were statistically significant. The acid concentration, leaching time, and other interactions were not statistically significant because they were close to the zero mean and distributed around a fixed zero mean (Shemi, 2013).

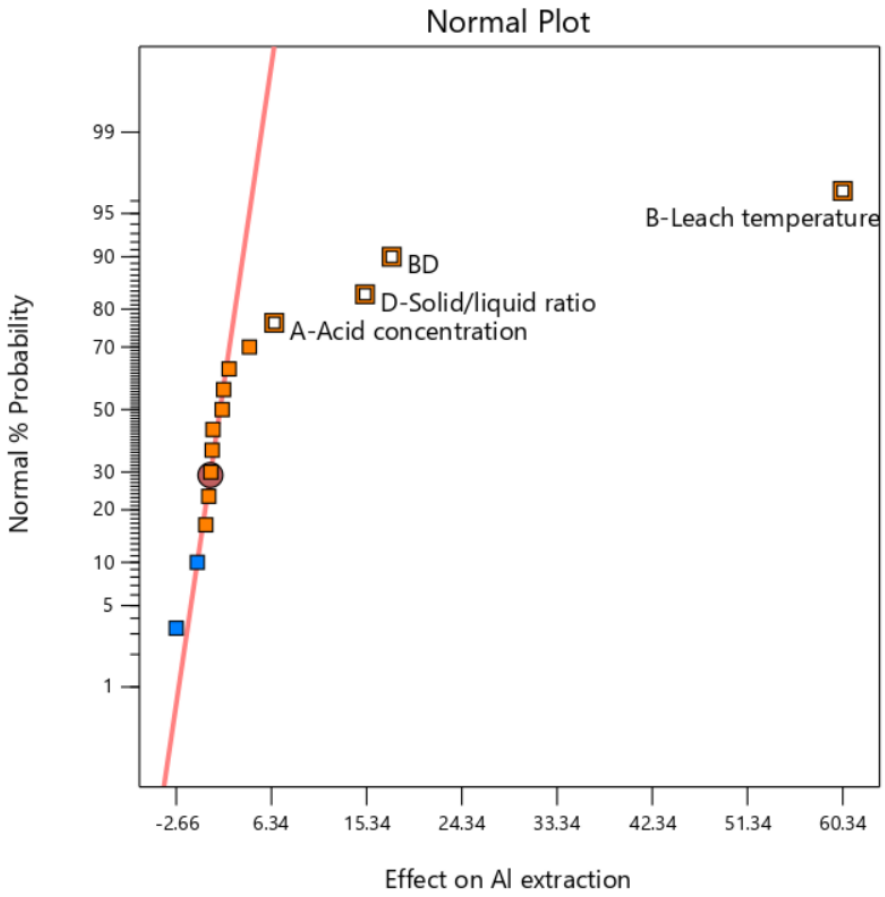

Figure 5.14: Graphical representation displaying effects of main factors and factor interactions for FL clay

The graphical representation displaying effects for FL clay shown in Figure 5.14 was used to identify significant effects. The probability plots indicated that the leaching temperature, acid concentration, solid/liquid ratio, and interactions BD, and ABD were statistically significant because they were not evenly distributed around a central value of zero and were far from this value (Shemi, 2013). Furthermore, the leaching time and other interactions were not statistically significant, because they were found to be normally distributed and close to the zero mean (Shemi, 2013).

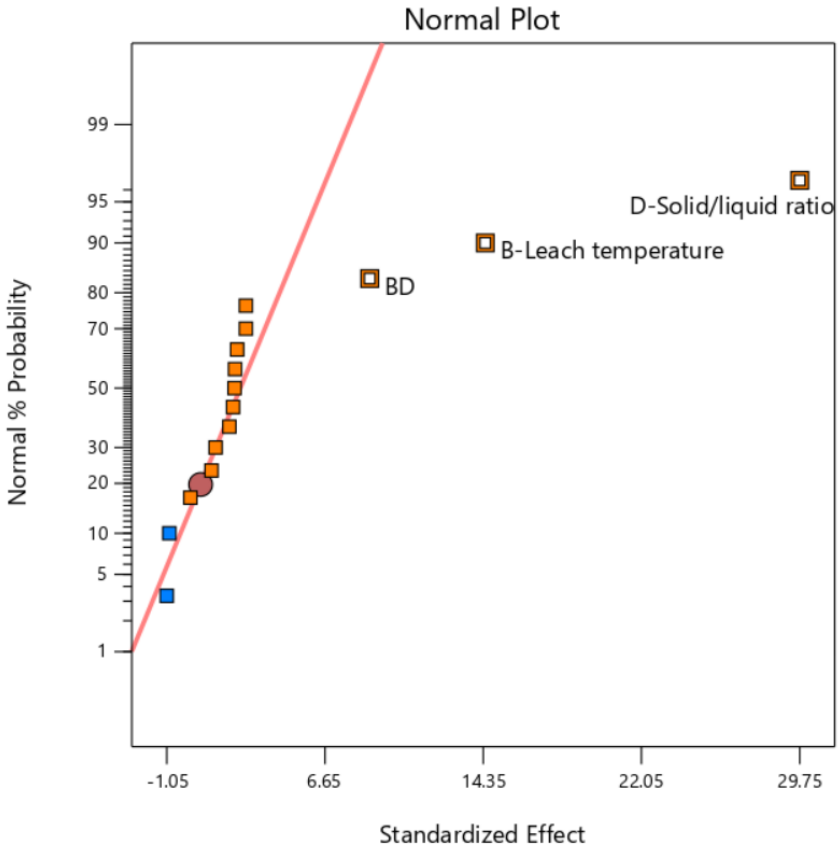

Figure 5.15: Graphical representation displaying effects of main factors and factor interactions for F clay

For F clay, the leaching temperature, leaching time, and solid/liquid ratio were statistically significant, as shown in Figure 5.15. Only the interactions BD and ABD were statistically significant. Additionally, Significant factors were distributed around the fixed zero and far from the zero mean (Shemi, 2013).

5.2.3. Polynomial model of the clays

F-tests were carried out using analysis of variance (ANOVA) to determine the significance of the model. In addition to the F-test, the coefficient of variation (CV), coefficient of determination (R^2), and adjusted coefficient of determination (R^2) were used to assess the adequacy of the model. The coefficient of determination (R^2) measures the efficiency of the experimental variables and their interactions in explaining the variability in the actual response values (Ohale *et al.*, 2017). A large disparity between the predicted and adjusted R2 values may indicate an issue with

either the data or model (Ohale *et al.*, 2017). The coefficient of variation (CV), which is a dimensionless ratio of the standard deviation of an estimate to its mean value, was used to evaluate the reproducibility and repeatability of the model, and remained unaffected by the unit of measurement (Ohale *et al.*, 2017).

The F-value of the BL clay model was 40.43 and the p-value was 0.0243, which implies that the model term in Equation 5.3 was significant, and that there was only a 2.43 % chance that such a large F-value occurred due to noise. The significance of the model terms is indicated by a p-value of less than 0. 0500.The only significant model term is X_B (0.0054). The model can effectively predict the percentage recovery of aluminum from BL clay. The F-value for the independent variable X_B was estimated at 184.75 and, indicating that the independent variables had a significantly high effect on the dependent variable. The calculations demonstrated a coefficient of variation of 6.32%, indicating that the model was reasonably replicable. Moreover, the signal-to-noise ratio, expressed as adequacy precision, was 15.260, suggesting satisfactory signal quality.

$$Y = 33.60 + 0.00X_A + 10.20X_B - 1.08X_C + 1.10X_AX_B + 2.73X_BX_C \qquad 5.3$$

The FL clay model demonstrated a noteworthy F-value of 297.71, with a p-value of less than 0.0001. This suggested that the model term (as per Equation 5.4) was significant and that there was only a 0.01% probability that such a large F-value would emerge due to random noise. The terms X_A, X_B, X_D, and X_BX_D were identified as significant model terms, with p-values less than 0.0001, except for X_A (0.0049). The F-values for X_A, X_B, and X_D were estimated to be 12.31, 1025.22, and 64.96, respectively, indicating that the independent variables had a substantial impact on the dependent variable, particularly X_B. The CV of the model was 8.31 %, indicating that it was reasonably reproducible. The signal-to-noise ratio was 40.184, suggesting an adequate balance between signal and noise in the model.

$$Y = 43.33 + 3.31X_A + 30.17X_B + 7.59X_D + 8.86X_BX_D \quad 5.4$$

The results of the F clay model revealed an F-value of 103.51 and a p-value of less than 0.0001, suggesting that the model term in Equation 5.5 was significant and had a less than 0.01% chance of being due to noise. Based on these findings, X_B (<0.0001), X_D (<0.0001), and X_BX_D (0.0007) were found to be the significant model terms. The F-values for independent variables X_B and X_D were estimated to be 55.34, and 234.56, respectively, indicating that X_D had a high effect on the dependent variable. A CV value of 11.54 % suggested that the model was reasonably replicable. The signal-to-noise ratio was 22.754, indicating an adequate relationship between signal and noise.

$$Y = 33.66 + 7.22X_B + 14.88X_D + 4.41X_BX_D \quad 5.5$$

Table 5.12: Regression values summary

	Std.Dev.	Mean	R^2	Adjusted R^2	Predicted R^2	PRESS
BL	2.12	33.60	0.9902	0.9657	0.8432	144.16
FL	3.77	45.33	0.9908	0.9875	0.9806	330.57
F	3.88	33.66	0.9628	0.9535	0.9339	321.98

The models for FL and F clays showed close correspondence with the experimental data, with R^2 values of 0.9908 and 0.9628, respectively (Table 5.12), except for BL clay. The aforementioned models accounted for 99% and 96% of the experimental data variability in the FL and F clays, respectively (Al-Zahrani and Abdul-Majid, 2009). The adjusted R^2 and predicted R^2 for BL clay were far apart from each other, indicating that there may be an issue with the data or model. The models (Equations 5.4, and 5.5) can be effectively used to predict the aluminum percentage recovery from FL and F clays, considering the specific levels of each factor. These models

play a important role in assessing the influence of various factors by comparing the coefficients associated with each one.

The model Equation 5.3 offered valuable insights into the relationship between the leaching temperature and the predicted Al extraction. The positive coefficient of X_B suggests that as the leaching temperature increased, the predicted Al extraction also increased by 10.20 %. Furthermore, in Equation 5.4, the coefficients for X_A, X_B and X_D were positive, indicating that as the acid concentration, leaching temperature and solid/liquid ratio increased, the predicted aluminum extraction increased by 3.3, 30.17 and 7.59 %, respectively. Additionally, the positive coefficient for X_BX_D indicated that the interaction between leaching temperature and solid/liquid ratio increased the aluminum extraction by 8.86 %. The coefficients for X_B and X_D were positive, indicating that an increase in the leaching temperature, and solid/liquid ratio would result in corresponding increases in Al extraction of 7.22 % and 14.88 %, respectively, as shown in Equation 5.5. Furthermore, the interaction term X_BX_D, which had a positive coefficient, indicated that the combined effects of the leaching temperature and solid/liquid ratio had a positive impact on Al extraction, increasing it by 4.41 %.

5.2.4. Interactions between the different leaching conditions

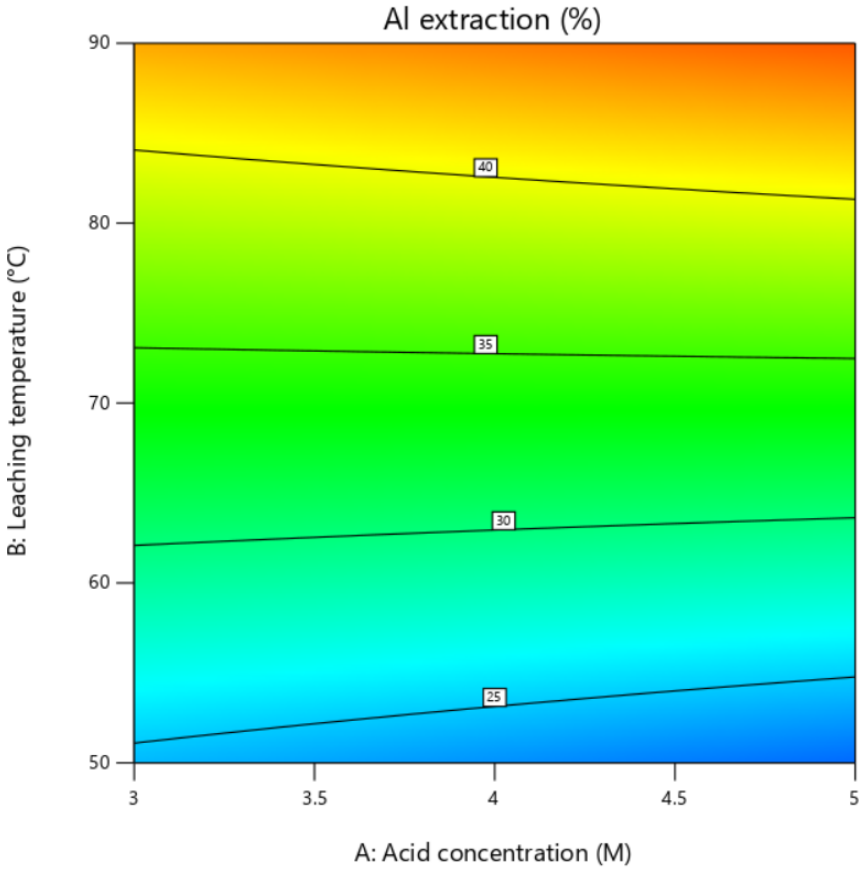

Figure 5.16: Influence of acid concentration and leaching time during Al extraction from BL clay

The contour lines in Figure 5.16 suggest that for BL clay, operating at a high leaching temperature can achieve Al extraction of over 40%, whereas operating at low leaching temperatures, less than 25% Al extraction can be obtained. Nevertheless, these effects occur regardless of operating at either high or low acid concentration.

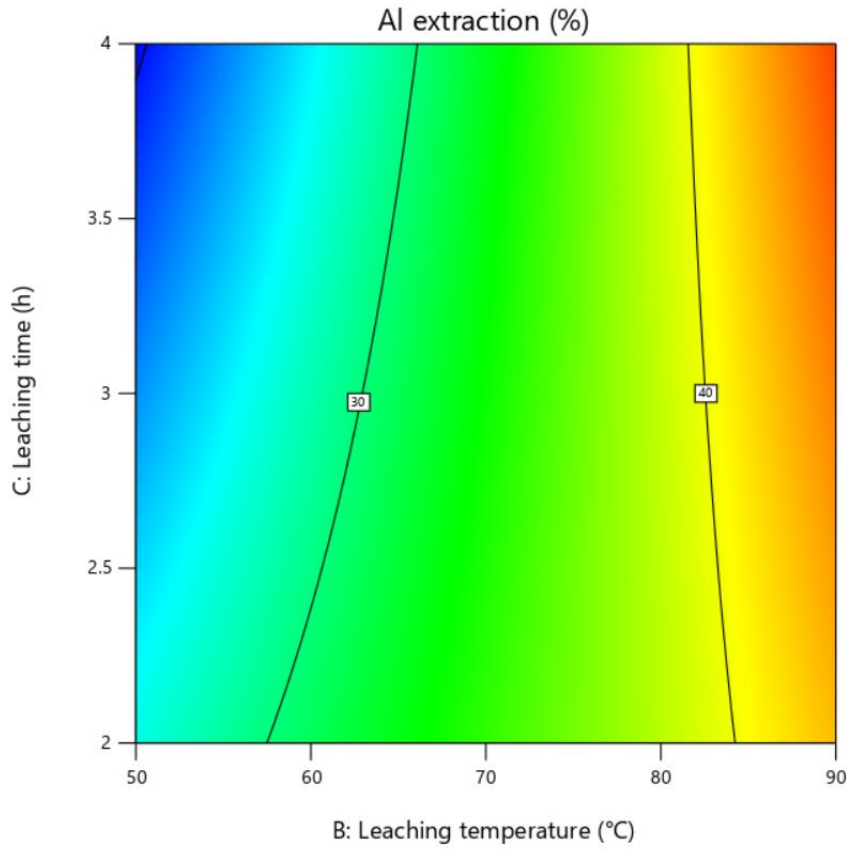

Figure 5.17: Influence of leaching temperature and time during Al extraction from BL clay

The Figure 5.17 illustrates that a high leaching temperature may result in an Al extraction of more than 40%, whereas a low leaching temperature may yield less than 30% Al extraction, regardless of the duration of the leaching process.

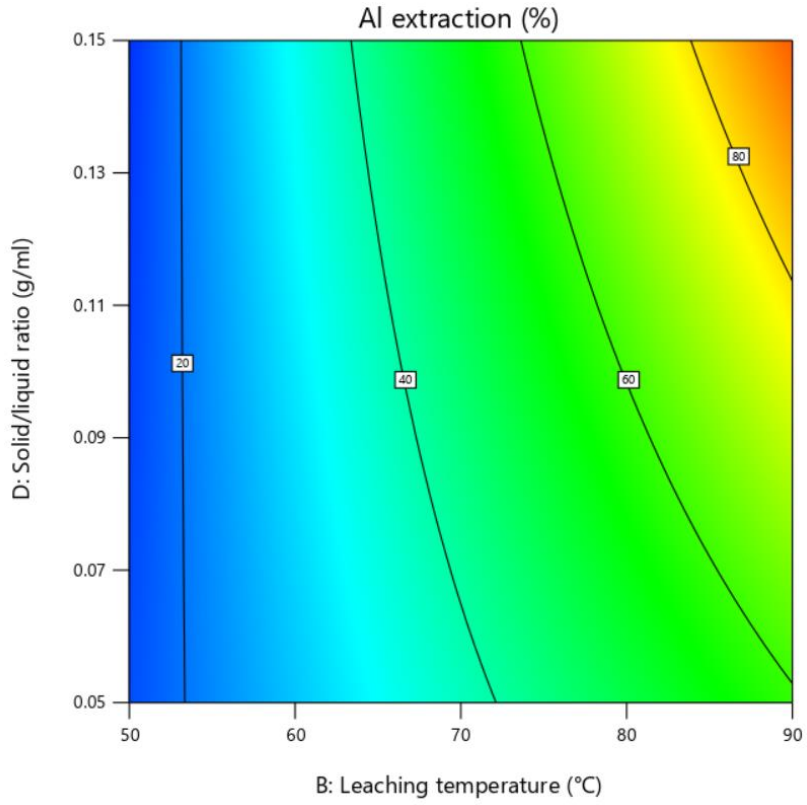

Figure 5.18: Influence of leaching temperature and solid/liquid ratio during Al extraction from FL clay

The Al extraction percentage of the FL clay increased with increasing leaching temperature, as displayed in Figure 5.18. The contour lines suggested that operating at low temperatures would yield low Al extraction, regardless of whether operating at lower or higher solid/liquid ratios. Additionally, the contour lines indicate that Al extraction of over 80% can be achieved.

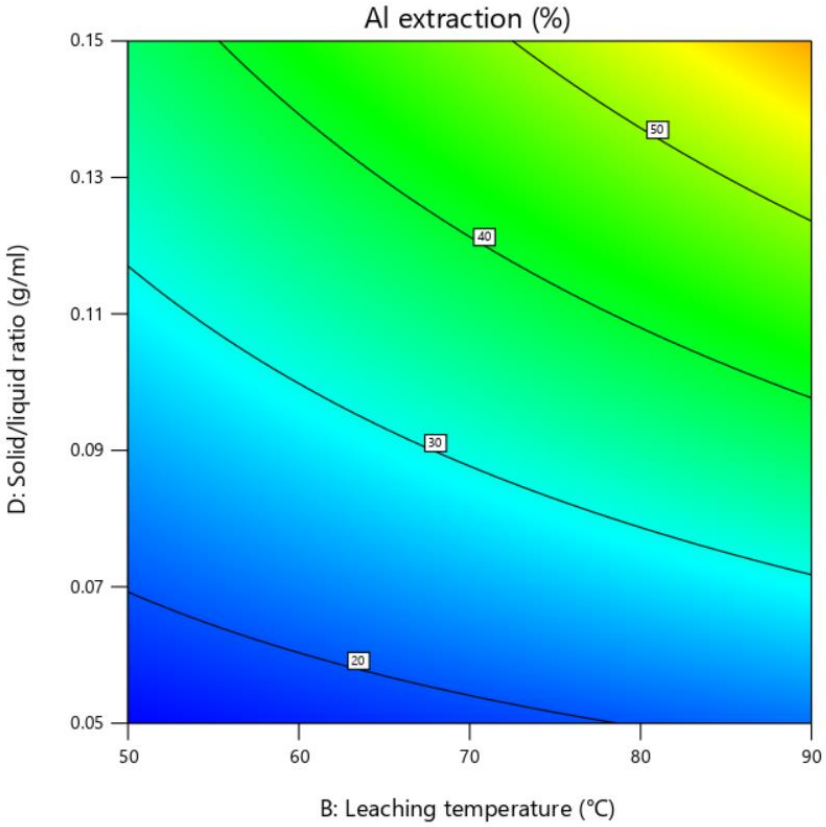

Figure 5.19: Influence of leaching temperature and solid/liquid ratio during Al extraction from F clay

As shown in Figure 5.19, increasing the leaching temperature and solid/liquid ratio increased the Al extraction % from F clay. The contour lines indicate that at 90°C and 0.15 g/ml, Al extraction of over 50 % can be achieved.

5.3. Summary

Calcined BL and FL clays are better sources of aluminum than calcined F clay, and they offer potential economic benefits for the South African aluminum industry. Additionally, these clays have lower energy requirements for the pretreatment step before acid leaching and higher aluminum recovery rates, which could make them valuable sources of aluminum in the future.

Chapter 6 Conclusion and Recommendations

6.1. Overview

The need for high-purity alumina (HPA) is anticipated to persist, as it is an essential component in the production of LEDs and Li-ion battery separators, both of which demand a purity level of 99.99% or higher. Currently, HPA is produced from a very expensive feedstock, high-purity Al metal (which is linked to the Bayer process), and bauxite ore (whose reserves are depleting). Therefore, there is considerable interest in developing new processing routes for low-cost materials, particularly aluminosilicate clays. The most promising process for treating kaolinitic clays is the HCl processing route. South Africa neither mines nor refines the bauxite. Moreover, the South African aluminum industry roadmap was designed to tackle the challenge of sustaining and cultivating an academic and research and development community that supports regional growth, promotes native innovation, nurtures indigenous design, and readies young talent to join and contribute to the sector. Furthermore, South Africa has abundant and easily accessible kaolinitic clays throughout the country. Hence, the feasibility of alumina extraction from South African clays through the HCl processing route was investigated, with a focus on assessing the selectivity of aluminum extraction relative to iron impurities.

In this study, three kaolinitic clays were prepared and characterized for their mineralogical and chemical compositions. The clays were thermally treated via calcination followed by HCl leaching to recover Al. Furthermore, the impact of calcination temperature on the mineralogical thermal behavior of clays and the reactivity of the clays to HCl acid, focusing on the extraction of Al, was assessed. Statistical analysis was conducted on three calcined samples (one from the three kaolinitic clays) to examine the effect of leaching conditions such as acid concentration, leaching temperature and time, and solid/liquid ratio on the recovery of Al. The objectives of this research were accomplished, and the findings were reported.

6.2. Key findings of the research study

Mineralogical and characterization analysis of South African kaolinitic clay samples

The three South African kaolinitic clays exhibited varying compositions. BL clay was characterized by high levels of kaolinite (82.4%) and quartz (14.3%). FL clay contained even more kaolinite (91.1%) with a lower quartz content (6.6%), while F clay had significantly less kaolinite (16.5%) and more quartz (44.7%). BL and FL clays also contained minor amounts of muscovite and traces of anatase. In contrast, F clay was distinguished by its elevated levels of dolomite (17.4%), calcite (7.5%), muscovite (8.1%), smectite (5.5%), and traces of anatase. Chemical analysis further revealed differences among the clays. BL clay contained 33.8% Al_2O_3 and 50.4% SiO_2, whereas FL clay contained 36.9% Al_2O_3 and 46.8% SiO_2. On the other hand, F clay displayed lower levels of Al_2O_3 (12.8%) and higher levels of SiO_2 (54.6%). Regarding Fe_2O_3 content, BL clay contained 0.706%, FL clay had 0.524%, and F clay demonstrated a notably higher concentration of 2.245%. These variations in composition among the clays highlighted their distinct characteristics and potential applications in HPA production.

Thermal behaviour of raw kaolinitic clays

Dehydroxylation of kaolinite domain for both BL and FL clays occurred between 330 and 700°C, while for F clay occurred between 390 and 540 °C.

Pre-treatment method via calcination process results (Mineralogical and structural changes)

At a calcination temperature of 600 °C, kaolinite in the BL, FL, and F clays underwent a complete transformation into the amorphous phase, a change that persisted up to 800 °C without significant alteration. Notably, the quartz exhibited no significant mineralogical changes during the thermal process. Muscovite, however, underwent dehydroxylation while maintaining its crystalline structure within the 600–800 °C temperature range. The decomposition of calcite and dolomite into free lime and the release of CO_2 occurred at higher calcination

temperatures, typically between 750 and 800 °C. Moreover, the free lime reacted with the amorphous phase, forming amorphous Ca-containing transitional phases before recrystallization of the amorphous phase. Structural analysis indicated the absence of OH hydroxyl groups and Al-OH bands due to the complete removal of structural water in the clay matrix at 600 °C. Furthermore, structural changes revealed the emergence of characteristic amorphous SiO_2 features, where the Si-O characteristic bands were transformed into a single absorption band. Despite the transformations, the Si-O characteristic bands of quartz remained consistently present at all calcination temperatures. In the case of F clay, the characteristic bands of carbonate clay minerals (calcite and dolomite) gradually decreased with increasing calcination temperature up to 700 °C, and completely disappeared at 750 and 800 °C. These findings illustrate the complex thermal behaviors and structural transformations occurring within clay minerals under varying calcination conditions.

HCl acid leaching experiments results (impact of calcination temperature on extraction of Al and Fe)

The highest Al extraction (79.4%) and Fe extraction (67.8%) were achieved for BL clay calcined at 600 °C, indicating the high reactivity of the amorphous metakaolinite phase. However, Al extraction decreased with increasing calcination temperature from 650 °C to 700 °C for calcined BL clay, with a slight increase observed at 800 °C. This suggests structural rearrangement of the amorphous phase, with iron diffusing into the amorphous phase during spinel phase formation. Consequently, the reactivity of calcined clay decreased due to reduced dissolution, likely caused by Fe diffusion into the amorphous metakaolinite phase. For calcined FL clay, three Al extraction peaks were observed at 600 °C (78.4%), 700 °C (69.5%), and 800 °C (71.8%). The corresponding Fe extraction rates were 66, 44, and 40.2%, respectively. Despite the small amount of Fe in the raw FL clay, leading to the absence of spinel formation at 600 °C, 700 °C, and 800 °C, Fe diffusion into the amorphous phase at 650 °C and 750 °C reduced Al extraction. The Al extraction for F clay remained below 50% and increased with higher calcination temperatures. However, owing to the higher impurity content and elevated Fe extraction compared to Al extraction at all calcination temperatures, the F clay exhibited a

lower overall reactivity. Calcined BL and FL clays showed Si extraction rates of less than 0.5% across various calcination temperatures, indicating that calcination temperature had minimal effect on Si dissolution in calcined clays.

HCl acid leaching experiments results (effect of leaching conditions on the extraction of Al)

Statistical analysis revealed notable impacts of leaching temperature on Al extraction for calcined BL clay, with the model equation indicating a 10.20% increase in the predicted Al extraction at higher leaching temperatures. For FL clay, the leaching temperature, solid/liquid ratio, acid concentration, and their interactions significantly influenced Al extraction. The model equation suggested that as acid concentration, leaching temperature, and solid/liquid ratio increased, predicted aluminum extraction increased by 3.3%, 30.17%, and 7.59%, respectively, with an additional 8.86% increase due to the interaction between leaching temperature and solid/liquid ratio. Similarly, Al extraction from F clay was notably affected by the solid/liquid ratio, leaching temperature, and their interaction. The model equation indicated that increases in leaching temperature and solid/liquid ratio corresponded to increases in Al extraction of 7.22% and 14.88%, respectively, with a further 4.41% increase attributed to the combined effects of leaching temperature and solid/liquid ratio.

In summary, both XRD and FTIR analyses confirmed the transformation of kaolinite into a reactive amorphous phase by calcination. Two of the three South African kaolinitic clays can be used to extract alumina. Although BL and FL clays calcined at 600 °C offered high Al dissolution, it would be costly to process high iron impurities in the downstream processes to produce HPA. Meanwhile, calcined FL clay offered three calcination temperatures (600, 700, and 800°C) at which high Al dissolution could be obtained in the leachate. Processing calcined FL clay at 800 °C for Al extraction has the benefit of reducing the cost of the downstream processes because of its moderate iron content. However, this comes at the cost of requiring more energy in the pretreatment step. Calcined F clay is not suitable for alumina extraction because it contains many impurities. The use of low-cost

kaolinitic clays will create new opportunities for economic gains for the South African aluminum industry using local resources.

6.3. Recommendations for future studies

Suggestions for further research based on the results of this study are as follows:

- Calcination of raw BL and FL clay at the lower tail temperatures of the dehydroxylation of the kaolinite domain, which is between 400 and 600 °C, and assessment of the Al and Fe extraction obtained at that calcination temperature range.
- Processing the leachates to the final alumina product for BL and FL clays.
- Future studies can focus on replicating DOE leaching conditions to confirm their efficacy and further refine the process.

References

Abdullah, S.F.A., Saleh, S.S.M., Mohammad, N.F., Idris, M.S. and Saliu, H.R. (2021) 'Effect of Thermal Treatment on Natural Dolomite', in *Journal of Physics: Conference Series*.

Abyzov, A.M. (2019) 'Aluminum Oxide and Alumina Ceramics (review). Part 1. Properties of Al2O3 and Commercial Production of Dispersed Al2O3', *Refractories and Industrial Ceramics*, 60(1), pp. 24–32.

Ajemba, R.O. and Onukwuli, O.D. (2012a) 'Determination Of The Optimum Dissolution Conditions Of Ukpor Clay In Hydrochloric Acid Using Response Surface Methodology', *International Journal of Engineering Research and Applications (IJERA)*, 2(5), pp. 732–742.

Ajemba, R.O. and Onukwuli, O.D. (2012b) 'Studies of the Effects Of Hydrochloric Acid-Leaching On The Structural And Adsorptive Performance Of NTEJE (Nigeria) Clay', 1(3), pp. 1–11.

Al-ajeel, A.W.A., Abdullah, S.Z., Muslim, W.A., Abdulkhader, M.Q., Al-Halbosy, M.K. and Al-Jumely, F.A. (2014) 'EXTRACTION OF ALUMINA FROM IRAQI COLORED KAOLIN BY LIME-SINTER PROCESS', *Iraqi Bulletin of Geology and Mining*, 10(3), pp. 109–117.

Al-ajeel, A.W.A. and Al-sindy, S.I. (2006) 'ALUMINA RECOVERY FROM IRAQI KAOLINITIC CLAY BY HYDROCHLORIC ACID ROUTE', *Iraqi Bulletin of Geology and Mining*, 2(1), pp. 67–76.

Al-Harahsheh, M., Olaem, N.A., Tahat, O. and Altarawneh, M. (2023) 'Pressure leaching of aluminum from kaolin by HCl: Experimental and DFT study', *Hydrometallurgy*, 221(July), p. 106122.

Al-Zahrani, A. and Abdul-Majid, M. (2009) 'Extraction of Alumina from Local Clays by Hydrochloric Acid Process', *Journal of King Abdulaziz University-Engineering Sciences*, 20(2), pp. 29–41.

Al-Zahrani, A.A. and Abdul-Majid, M.H. (2009) 'Extraction of Alumina from Local Clays by Hydrochloric Acid Process', *JKAU:Eng.Sci*, 20(2), pp. 29–41.

Ali, A.H. and Al-taie, M.H. (2019) 'The Extraction of Alumina from Kaolin', *Engineering and Technology Journal*, 37(04), pp. 133–139.

Allegretta, I., Pinto, D. and Eramo, G. (2016) 'Effects of grain size on the reactivity of limestone temper in a kaolinitic clay', *Applied Clay Science*, 126, pp. 223–234.

Aly, S., Ibrahim, I. and Abadir, M. (2019) 'UTILIZATION OF KALAPSHA KAOLIN TO PREPARE HIGH PURITY ALUMINA', *Egyptian Journal of Chemistry*, 62(9), pp. 1699–1712.

Alyosif, B., Uysal, T. and Erdemoğlu, M. (2023) 'Potassium chloride recovery from mechanically activated microcline through the chlorination roasting and leaching route', *Physicochemical Problems of Mineral Processing*, 59(5).

Authier-Martin, M., Forté, G., Ostap, S. and See, J. (2001) 'The mineralogy of bauxite for producing smelter-grade alumina', *Jom*, pp. 36–40.

Bagani, M., Balomenos, E. and Panias, D. (2021) 'Exploitation of Kaolin as an Alternative Source in Alumina Production', *Materials Proceedings*, 5(1), p. 24.

Bagherzadeh, Y., Golmakani, M.H. and Karimi, E.Z. (2023) 'Straight synthesis of α and γ alumina from kaolin by HCl acid leaching', *Journal of Mining and Metallurgy, Section B: Metallurgy*, 59(2), pp. 195–204.

Bai, J. and Guo, L. (2006) 'Effects of chemical treatments on thermal expansion properties of cordierite ceramics', *Journal Wuhan University of Technology, Materials Science Edition*, 21(3), pp. 100–102.

Barakan, S. and Aghazadeh, V. (2021) 'The advantages of clay mineral modification methods for enhancing adsorption efficiency in wastewater treatment: a review', *Environmental Science and Pollution Research*, 28(3), pp. 2572–2599.

Barry, T.S., Uysal, T., Birinci, M. and Erdemoğlu, M. (2019) 'Thermal and Mechanical Activation in Acid Leaching Processes of Non-bauxite Ores Available for Alumina Production—A Review', *Mining, Metallurgy and Exploration*, 36(3), pp. 557–569.

Barton, C.D. and Karanthanasis, A.D. (2005) 'Clays Minerals', in *Encyclopedia of soil science*, pp. 379–381.

Bergaya, F., Theng, B.K.G. and Lagaly, G. (2006) 'Iron redox processes in smectites', in *Handbook of Clay Science*. Elsevier, pp. 1–40.

Besselink, R., Stawski, T.M., Freeman, H.M., Hövelmann, J., Tobler, D.J. and Benning, L.G. (2020) 'Mechanism of Saponite Crystallization from a Rapidly Formed Amorphous

Intermediate', *Crystal Growth & Design*, 20(5), pp. 3365–3373.

Birincia, M., Uysala, T., Erdemoğlua, M., Porgalıb, E. and T.S. Barry. (2017) 'Acidic leaching of thermally activated pyrophyllite ore from acidic leaching of thermally activated pyrophyllite ore from pütür-ge (malatya -turkey) deposit', *XVII balkan mineral processing congress* [Preprint], (November).

Biswas, B., Islam, M.R., Deb, A.K., Greenaway, A., Warr, L.N. and Naidu, R. (2023) 'Understanding Iron Impurities in Australian Kaolin and Their Effect on Acid and Heat Activation Processes of Clay', *ACS Omega*, 8(6), pp. 5533–5544.

Cao, P., Luo, J., Jiang, H., Zhang, X., Rao, M. and Li, G. (2022) 'Extraction of alumina from low-grade kaolin in the presence of lime and NaOH via multi-stage hydrothermal process', *Applied Clay Science*, 229(July), p. 106675.

Capuzzi, S. and Timelli, G. (2018) 'Preparation and Melting of Scrap in Aluminum Recycling: A Review', *Metals*, 8(4), p. 249.

Chang, L. (2016) *A Comprehensive Mechanistic Study on Using Fine Lightweight Aggregate to Mitigate Alkali-silica Reaction*, *October*.

Chin, C.L., Ahmad, Z.A. and Sow, S.S. (2017) 'Relationship between the thermal behaviour of the clays and their mineralogical and chemical composition: Example of Ipoh, Kuala Rompin and Mersing (Malaysia)', *Applied Clay Science*, 143(March), pp. 327–335.

Crundwell, F.K. (2014) 'The mechanism of dissolution of minerals in acidic and alkaline solutions: Part II Application of a new theory to silicates, aluminosilicates and quartz', *Hydrometallurgy*, 149, pp. 265–275.

Cultrone, G. and Carrillo Rosua, F.J. (2020) 'Growth of metastable phases during brick firing: Mineralogical and microtextural changes induced by the composition of the raw material and the presence of additives', *Applied Clay Science*, 185(December 2019), p. 105419.

D'Elia, A., Pinto, D., Eramo, G., Giannossa, L.C., Ventruti, G. and Laviano, R. (2018) 'Effects of processing on the mineralogy and solubility of carbonate-rich clays for alkaline activation purpose: mechanical, thermal activation in red/ox atmosphere and their combination', *Applied Clay Science*, 152(November 2017), pp. 9–21.

Dabare, L. and Svinka, R. (2013) 'Influence of thermal treatment and combustible additives on properties of Latvian clay ceramics pellets', *Processing and Application of Ceramics*, 7(4), pp. 175–180.

Dagde, K.K. (2019) 'Production of Alumina from Local Clays using Nitric and Acetic Acids (Part A)', *Chemical and Process Engineering Research*, pp. 39–51.

Daniels, A.L., Muzenda, E., Belaid, M. and Ntuli, F. (2012) 'Recovery of aluminium oxide from flint clay through H2SO4 leaching', in *Proceedings of the World Congress on Engineering*, pp. 1388–1390.

Danner, T., Norden, G. and Justnes, H. (2018) 'Characterisation of calcined raw clays suitable as supplementary cementitious materials', *Applied Clay Science*, 162(June), pp. 391–402.

David (2018) *Aluminum Extraction Method with Chloride*, *911 metallurgist*. Available at: https://www.911metallurgist.com/chloride-method-extracting-aluminum-clay/.

Debure, M., Lerouge, C., Warmont, F., Bocher, L., Lundy, M., Madé, B. and Grangeon, S. (2021) 'On the interaction between calcite and dolomite: Insights from gas and aqueous geochemistry and mineralogical characterization', *Chemical Geology*, 559(October 2020), p. 119921.

Department of Science and Technology and Council for Scientific and Industrial Research (2017) *The South African Aluminium Industry Roadmap*.

Diko, M., Ekosse, G. and Ogola, J. (2015) 'Fourier transform infrared spectroscopy and thermal analyses of kaolinitic clays from South Africa and Cameroon', *Acta Geodynamica et Geomaterialia*, 13(2), pp. 149–158.

Donaldson, D. and Raahauge, B.E. (2008) 'Light Metals', in. Switzerland: Springer International Publishers, pp. 95–95.

Ekosse, G.I.E. (2010) 'Kaolin deposits and occurrences in Africa: Geology, mineralogy and utilization', *Applied Clay Science*, 50(2), pp. 212–236.

ElDeeb, A.B., Brichkin, V.N., Kurtenkov, R. V. and Bormotov, I.S. (2019) 'Extraction of alumina from kaolin by a combination of pyro- and hydro-metallurgical processes', *Applied Clay Science*, 172(March), pp. 146–154.

ElDeeb, A.B., Brichkin, V.N., Bertau, M., Savinova, Y.A. and Kurtenkov, R. V. (2020) 'Solid state and phase transformation mechanism of kaolin sintered with limestone for alumina extraction', *Applied Clay Science*, 196(July), p. 105771.

Erdemoğlu, M., Birinci, M., Uysal, T., Porgalı Tüzer, E. and Barry, T.S. (2018) 'Mechanical activation of pyrophyllite ore for aluminum extraction by acidic leaching', *Journal of Materials Science*, 53(19), pp. 13801–13812.

Erdemoğlu, M., Birinci, M. and Uysal, T. (2020a) 'Thermal Behavior of Pyrophyllite Ore during Calcination for Thermal Activation for Aluminum Extraction by Acid Leaching', *Clays and Clay Minerals*, 68(2), pp. 89–99.

Erdemoğlu, M., Birinci, M. and Uysal, T. (2020b) 'Thermal Behavior of Pyrophyllite Ore during Calcination for Thermal Activation for Aluminum Extraction by Acid Leaching', *Clays and Clay Minerals*, 68(2), pp. 89–99.

Escalera, E., Tegman, R., Antti, M.L. and Odén, M. (2014) 'High temperature phase evolution of Bolivian kaolinitic-illitic clays heated to 1250°C', *Applied Clay Science*, 101, pp. 100–105.

Escalera, E., Antti, M.L. and Odén, M. (2012) 'Thermal treatment and phase formation in kaolinite and illite based clays from tropical regions of Bolivia', *IOP Conference Series: Materials Science and Engineering*, 31.

Evans, K. (2016) 'The History, Challenges, and New Developments in the Management and Use of Bauxite Residue', *Journal of Sustainable Metallurgy*, 2(4), pp. 316–331.

Fabbri, B, Gualtieri, S. and Leonardi, C. (2013) 'Modifications induced by the thermal treatment of kaolin and determination of reactivity of metakaolin', *Applied Clay Science*, 73, pp. 2–10.

Fabbri, B., Gualtieri, S. and Leonardi, C. (2013) 'Modifications induced by the thermal treatment of kaolin and determination of reactivity of metakaolin', *Applied Clay Science*, 73(1), pp. 2–10.

Fernandez, R., Martirena, F. and Scrivener, K.L. (2011) 'The origin of the pozzolanic activity of calcined clay minerals: A comparison between kaolinite, illite and montmorillonite', *Cement and Concrete Research*, 41(1), pp. 113–122.

Forano, C., Hibino, T., Leroux, F. and Taviot-Guého, C. (2006) 'Chapter 13.1 Layered Double Hydroxides', in *Developments in Clay Science*, pp. 1021–1095.

Fujiwara, S., Tamura, Y., Maki, H., Azuma, N. and Takeuchi, Y. (2007) *Development of New High-Purity Alumina, "SUMITOMO KAGAKU", vol. 2007-I.*

Gasparini, E., Tarantino, S.C., Ghigna, P., Riccardi, M.P., Cedillo-González, E.I., Siligardi, C. and Zema, M. (2013) 'Thermal dehydroxylation of kaolinite under isothermal conditions', *Applied Clay Science*, 80–81, pp. 417–425.

Ghafar, H.H.A., Radwan, E.K. and El-Wakeel, S.T. (2020) 'Removal of Hazardous Contaminants from Water by Natural and Zwitterionic Surfactant-modified Clay', *ACS Omega*, 5(12), pp. 6834–6845.

Ghazali, N., Muthusamy, K. and Wan Ahmad, S. (2019) 'Utilization of Fly Ash in Construction', *IOP Conference Series: Materials Science and Engineering*, 601(1), p. 012023.

Gopinath, G. (2016) *Engineering ceramics*, *Slideshare*. Available at: https://www.slideshare.net/GopinathGuru3/engineering-ceramics.

Gridi-Bennadji, F., Beneu, B., Laval, J.P. and Blanchart, P. (2008) 'Structural transformations of Muscovite at high temperature by X-ray and neutron diffraction', *Applied Clay Science*, 38(3–4), pp. 259–267.

Habashi, F. (2017) 'Hydrochloric Acid in Hydrometallurgy', in *56th Annual Conference of Metallurgists*.

Haekal, H. and Mubarok, F. (2021) 'The Effect of the Holding Time on the Formation of Niobium-Vanadium Carbide Coating Onto Aisi 420 by Thermo Reactive Diffusion Process', *Jurnal Teknik ITS*, 9(2), pp. 374–379.

Hamer, C.A. (1977) *Acid Extraction For Non-Bauxite Alumina Materials*.

Hanein, T. *et al.* (2022) 'Clay calcination technology: state-of-the-art review by the RILEM TC 282-CCL', *Materials and Structures/Materiaux et Constructions*, 55(1).

Heckroodt, R.O. (1991) 'Clay and clay materials in South Africa', *Journal of The South African Institute of Mining and Metallurgy*, 91(10), pp. 343–363.

Heiri, O., Lotter, A.F. and Lemcke, G. (2001) 'Loss on Ignition as a Method for Estimating Organic and Carbonate Content in Sediments : Reproducibility and Comparability of Results Loss on ignition as a method for estimating organic and carbonate content in sediments : reproducibility and comparabilit', *Journal of Paleolimnology*, 25(January), pp. 101–110.

Hollanders, S., Adriaens, R., Skibsted, J., Cizer, Ö. and Elsen, J. (2016) 'Pozzolanic reactivity of pure calcined clays', *Applied Clay Science*, 132–133, pp. 552–560.

Hollanders, S. (2017) *Mineralogical study of the pozzolanic properties of calcined clays*.

Hu, B., Zhang, C. and Zhang, X. (2022) 'The Effects of Hydrochloric Acid Pretreatment on Different Types of Clay Minerals', *Minerals*, 12(9).

Ibrahim, K.M., Moumani, M.K. and Mohammad, S.K. (2018) 'Extraction of γ-alumina from low-cost kaolin', *Resources*, 7(4).

Izadifar, M., Thissen, P., Steudel, A., Kleeberg, R., Kaufhold, S., Kaltenbach, J., Schuhmann, R., Dehn, F. and Emmerich, K. (2020) 'Comprehensive Examination of Dehydroxylation of Kaolinite, Disordered Kaolinite, and Dickite: Experimental Studies and Density Functional Theory', *Clays and Clay Minerals*, 68(4), pp. 319–333.

Johnston, Cameron J., Pepper, R.A., Martens, W.N. and Couperthwaite, S. (2022) 'Improvement of aluminium extraction from low-grade kaolinite by iron oxide impurities: Role of clay chemistry and morphology', *Minerals Engineering*, 176(January 2021), p. 107346.

Johnston, Cameron J, Pepper, R.A., Martens, W.N. and Couperthwaite, S. (2022) 'Relationship between thermal dehydroxylation and aluminium extraction from a low-grade kaolinite: Role of clay chemistry and crystallinity', *Hydrometallurgy*, 214(April), p. 105967.

Kassa, A.E., Shibeshi, N.T., Tizazu, B.Z. and Prabhu, S.V. (2022) 'Characteristic Investigations on Ethiopian Kaolinite: Effect of Calcination Temperature on Pozzolanic Activity and Specific Surface Area', *Advances in Materials Science and Engineering*. Edited by R. Černý, 2022, pp. 1–8.

Kassa, A.E., Shibeshi, N.T. and Tizazu, B.Z. (2022) 'Characterization and Optimization of Calcination Process Parameters for Extraction of Aluminum from Ethiopian Kaolinite',

International Journal of Chemical Engineering, 2022.

Kaunisto, K., Lagerbom, J., Honkanen, M., Varis, T., Lambai, A., Mohanty, G., Levänen, E., Kivikytö-Reponen, P. and Frankberg, E. (2023) 'Evolution of alumina phase structure in thermal plasma processing', *Ceramics International*, 49(13), pp. 21346–21354.

Kaußen, F.M. and Friedrich, B. (2016) 'Methods for Alkaline Recovery of Aluminum from Bauxite Residue', *Journal of Sustainable Metallurgy*, 2(4), pp. 353–364.

Khalifa, A.Z., Pontikes, Y., Elsen, J. and Cizer, Ö. (2019) 'Comparing the reactivity of different natural clays under thermal and alkali activation', *RILEM Technical Letters*, 4(January 2020), pp. 74–80.

Khalifa, A.Z., Cizer, Ö., Pontikes, Y., Heath, A., Patureau, P., Bernal, S.A. and Marsh, A.T.M. (2020) 'Advances in alkali-activation of clay minerals', *Cement and Concrete Research*, 132(February), p. 106050.

Kuranga, I.A., Alafara, A.B., Halimah, F.B., Fausat, A.M., Mercy, O.B. and Tripathy, B.C. (2018) 'Production and characterization of water treatment coagulant from locally sourced kaolin clays', *Journal of Applied Sciences and Environmental Management*, 22(1), pp. 103–109.

Lecomte-Nana, G., Bonnet, J.-P. and Soro, N. (2013) 'Influence of iron onto the structural reorganization process during the sintering of kaolins', *Journal of the European Ceramic Society*, 33(4), pp. 661–668.

Lecomte-Nana, G., Bonnet, J.P. and Soro, N. (2013) 'Influence of iron on the occurrence of primary mullite in kaolin based materials: A semi-quantitative X-ray diffraction study', *Journal of the European Ceramic Society*, 33(4), pp. 669–677.

Lee, S.O. (2005) *Dissolution of iron oxides by oxalic acid*.

Lee, S.O., Jung, K.H., Oh, C.J., Lee, Y.H., Tran, T. and Kim, M.J. (2009) 'Precipitation of fine aluminium hydroxide from Bayer liquors', *Hydrometallurgy*, 98(1–2), pp. 156–161.

Li, S., Bo, P., Kang, L., Guo, H., Gao, W. and Qin, S. (2020) 'Activation pretreatment and leaching process of high-alumina coal fly ash to extract lithium and aluminum', *Metals*, 10(7), pp. 1–14.

Libbohole, A. and Kennedy, K.K. (2022) 'Adsorptive Removal of Copper (II) Ions from

Aqueous Solution using Acid and Thermally Activated Iron Oxide Sand', *Texila International Journal of Academic Research*, 9(4), pp. 100–107.

Lima, P.E.A., Angélica, R.S. and Neves, R.F. (2014) 'Dissolution kinetics of metakaolin in sulfuric acid: Comparison between heterogeneous and homogeneous reaction methods', *Applied Clay Science*, 88–89, pp. 159–162.

Liu, C., Wang, W., Wang, H., Zhu, C. and Ren, B. (2023) 'A Review on Removal of Iron Impurities from Quartz Mineral', *Minerals*, 13(9).

Liu, Y., Naidu, R. and Ming, H. (2011) 'Red mud as an amendment for pollutants in solid and liquid phases', *Geoderma*, 163(1–2), pp. 1–12.

Makó, É., Frost, R.L., Kristóf, J. and Horváth, E. (2001) 'The Effect of Quartz Content on the Mechanochemical Activation of Kaolinite', *Journal of Colloid and Interface Science*, 244(2), pp. 359–364.

MANIATIS, Y., SIMOPOULOS, A., KOSTIKAS, A. and PERDIKATSIS, V. (1983) 'Effect of Reducing Atmosphere on Minerals and Iron Oxides Developed in Fired Clays: The Role of Ca', *Journal of the American Ceramic Society*, 66(11), pp. 773–781.

Matmatch (2019) *Aluminium Oxide: Properties, Production, and Applications*. Available at: https://matmatch.com/learn/material/aluminium-oxide.

Metz, V., Amram, K. and Ganor, J. (2005) 'Stoichiometry of smectite dissolution reaction', *Geochimica et Cosmochimica Acta*, 69(7), pp. 1755–1772.

Do Nascimento, A.R., Alves, J.A.B.L.R., De Freitas Melo, M.A., De Araújo Melo, D.M., De Souza, M.J.B. and Pedrosa, A.M.G. (2015) 'Effect of the acid treatment of montmorillonite clay in the oleic acid esterification reaction', *Materials Research*, 18(2), pp. 283–287.

Nawel, S., Mounir, L. and Hedi, H. (2020) 'Effect of temperature on pozzolanic reaction of Tunisian clays calcined in laboratory', *SN Applied Sciences*, 2(2), p. 157.

Nevrla, B., Ctibor, P., Koudelkova, V., Lukac, F. and Neufuss, K. (2021) 'Plasma spraying of natural kaolinite and metakaolinite', *Boletin de la Sociedad Espanola de Ceramica y Vidrio*, 60(5), pp. 274–282.

Nnanwube, I.A. and Onukwuli, O.D. (2023) 'Characterization and kinetics of alumina leaching from calcined Akpugo kaolinite for potential aluminum recovery', *South African*

Journal of Chemical Engineering, 43(September 2022), pp. 24–37.

Novikova, L. and Belchinskaya, L. (2016) 'Adsorption of Industrial Pollutants by Natural and Modified Aluminosilicates', in *Clays, Clay Minerals and Ceramic Materials Based on Clay Minerals*. InTech, p. 13.

Obada, D.O., Dodoo-Arhin, D., Dauda, M., Anafi, F.O., Ahmed, A.S. and Ajayi, O.A. (2017) 'The impact of kaolin dehydroxylation on the porosity and mechanical integrity of kaolin based ceramics using different pore formers', *Results in Physics*, 7, pp. 2718–2727.

Ogbonnaya, E.S., Onyebuchukwu, M.G. and Rita, M.-I. (2018) 'Optimization And Process Modeling Of The Extraction Of Alumina From Aku Clay By Hydrochloric Acid Leaching', *American Journal of Engineering Research (AJER)*, 7(11), pp. 158–169.

Ohale, P.E., Uzoh, C.F. and Onukwuli, O.D. (2017) 'Optimal factor evaluation for the dissolution of alumina from Azaraegbelu clay in acid solution using RSM and ANN comparative analysis', *South African Journal of Chemical Engineering*, 24, pp. 43–54.

Okon, O.E., Israel, A.U., Inam, E.J. and Etim, U.J. (2019) 'Preparation and characterization of Fe 2 O 3 / mesoporous clay composite from Nigerian local bentonite clay', *Journal of Materials and Environmental Sciences*, 10(7), pp. 618–623.

Okwuzu, F.T., Igwegbe, C.A., Okafor, V.N., Ugwu, J.I. and Obi, C.V. (2022) 'Kinetics Study of Alumina Leaching from Ogbunike Clay Using Hydrochloric Acid', *European Journal of Sustainable Development Research*, 6(4), p. em0201.

Olaremu, A.G. (2015) 'Sequential Leaching for the Production of Alumina from a Nigerian Clay', *International Journal of Engineering Technology, Management and Applied Sciences (IJETMAS)*, 3(7), pp. 103–109.

Orosco, P., Ruiz, M. del C. and González, J. (2014) 'Synthesis of cordierite by dolomite and kaolinitic clay chlorination. Study of the phase transformations and reaction mechanism', *Powder Technology*, 267, pp. 111–118.

Ortega, A., Macías, M. and Gotor, F.J. (2010) 'The multistep nature of the kaolinite dehydroxylation: Kinetics and mechanism', *Journal of the American Ceramic Society*, 93(1), pp. 197–203.

Orugba, Henry Oghenero, Onukwuli, O.D., Babayemi, A.K. and Umezuegbu, C. (2020)

'Application of the Shrinking Core Models to Hydrochloric Acid Dissolution of Alumina from Clay', *ABUAD Journal of Engineering Research and Development (AJERD)*, 3(1), pp. 59–67.

Orugba, H O, Onukweli, O.D., Babayemi, A.K. and Umezuegbu, J.C. (2020) 'FIVE-FACTOR RESPONSE SURFACE OPTIMISATION OF HYDROCHLORIC ACID DISSOLUTION OF ALUMINA FROM A NIGERIAN CLAY', *Arid Zone Journal of Engineering, Technology & Environment (AZOJETE)*, 16(4), pp. 821–832.

Overmann, S., Vollpracht, A. and Matschei, T. (2024) 'Reactivity of Calcined Clays as SCM—A Review', *Materials*, 17(2), p. 312.

Pak, Vyacheslav I., Kirov, S.S., Nalivaiko, A.Y., Ozherelkov, D.Y. and Gromov, A.A. (2019) 'Obtaining alumina from kaolin clay via aluminum chloride', *Materials*, 12(23).

Pak, Vyacheslav I, Kirov, S.S., Nalivaiko, A.Y., Ozherelkov, D.Y. and Gromov, A.A. (2019) 'Obtaining Alumina from Kaolin Clay via Aluminum Chloride', *Materials*, 12(23), p. 3938.

Pehlivan, A., Alp, A. and Aydin, A.O. (2012) 'Alumina Extraction From Low-Grade Diasporic Bauxite By Pyro-Hydro Metallurgical Process', *SAÜ Fen Bilimleri Enstitüsü Dergisi*, 16(2), pp. 92–98.

Pei, Z., Lin, M., Liu, Y. and Lei, S. (2018) 'Dissolution Behaviors of Trace Muscovite during Pressure Leaching of Hydrothermal Vein Quartz Using H2SO4 and NH4Cl as Leaching Agents', *Minerals*, 8(2), p. 60.

Pepper, R.A., Perenlei, G., Martens, W.N. and Couperthwaite, S.J. (2021) 'High purity alumina synthesised from iron rich clay through a novel and selective hybrid ammonium alum process', *Hydrometallurgy*, 204(January), p. 105728.

Perkins, A.T. (1964) 'Decomposition of Silicate Minerals by Acid Extractions Chemical Composition and Exchange Capacity', *Kansas Academy of Science*, 67(3), pp. 486–495.

Peters, F.A., Kirby, R.C. and Higbie, K.B. (1967) 'Methods for producing alumina from clay-an evaluation', *Journal of Metals* [Preprint].

Poo-arporn, Y., Luengprasert, K., Tonlublao, S., Loiha, S., Ruangvittayanon, A. and Poo-arporn, R.P. (2020) 'The influence of calcination temperature on (photo)electrochemical property of TiO 2 prepared by the sol-gel method', in *IOP Conference Series: Materials*

Science and Engineering, p. 012005.

Pourghahramani, P., Altin, E., Mallembakam, M.R., Peukert, W. and Forssberg, E. (2008) 'Microstructural characterization of hematite during wet and dry millings using Rietveld and XRD line profile analyses', *Powder Technology*, 186(1), pp. 9–21.

Ptáček, P., Frajkorová, F., Šoukal, F. and Opravil, T. (2014) 'Kinetics and mechanism of three stages of thermal transformation of kaolinite to metakaolinite', *Powder Technology*, 264, pp. 439–445.

Rahayu, E.S., Subiyanto, G., Shoelarta, S., Hartono, M.I. and Elisafa, H. (2019) 'The effect of the process condition on synthesis amorphous silica alumina from metakaolin on pore structure and crystallinity of product', in A. Orbecido et al. (eds) *MATEC Web of Conferences*, p. 04002.

Ramadji, C., Messan, A., Sore, S.O., Prud'homme, E. and Nshimiyimana, P. (2022) 'Microstructural Analysis of the Reactivity Parameters of Calcined Clays', *Sustainability*, 14(4), p. 2308.

Salahudeen, N., Ahmed, A.S., Al-Muhtaseb, A.H., Dauda, M., Waziri, S.M. and Jibril, B.Y. (2015) 'Synthesis of gamma alumina from Kankara kaolin using a novel technique', *Applied Clay Science*, 105–106, pp. 170–177.

Sampath, A.H.J., Wickramasinghe, N.D., de Silva, K.M.N. and de Silva, R.M. (2023) 'Methods of Extracting TiO2 and Other Related Compounds from Ilmenite', *Minerals*, 13(5), p. 662.

San Cristóbal, A.G., Castelló, R., Martín Luengo, M.A. and Vizcayno, C. (2009) 'Acid activation of mechanically and thermally modified kaolins', *Materials Research Bulletin*, 44(11), pp. 2103–2111.

Schackow, A., Correia, S.L. and Effting, C. (2020) 'Influence of microstructural and morphological properties of raw natural clays on the reactivity of clay brick wastes in a cementitious blend matrix', *Ceramica*, 66(378), pp. 154–163.

Sellaeg, H., Kolbeinsen, L. and Safarian, J. (2017) 'Iron Separation from Bauxite Through Smelting-Reduction Process', *Minerals, Metals and Materials Series*, pp. 127–135.

Shemi, A. (2013) *EXTRACTION OF ALUMINIUM FROM COAL FLY ASH USING A TWO-STEP*

ACID LEACH PROCESS. University of Witwaterand.

Si, P., Qiao, X. and Yu, J. (2012) 'Alumina recovery from kaolin with mineral impurities', *Journal Wuhan University of Technology, Materials Science Edition*, 27(6), pp. 1139–1143.

Sibanda, V., Ndlovu, S., Dombo, G., Shemi, A. and Rampou, M. (2016) 'Towards the Utilization of Fly Ash as a Feedstock for Smelter Grade Alumina Production: A Review of the Developments', *Journal of Sustainable Metallurgy*, 2(2), pp. 167–184.

Smith, R.J., Rampe, E.B., Horgan, B.H.N. and Dehouck, E. (2018) 'Deriving Amorphous Component Abundance and Composition of Rocks and Sediments on Earth and Mars', *Journal of Geophysical Research: Planets*, 123(10), pp. 2485–2505.

Souri, A., Kazemi-Kamyab, H., Snellings, R., Naghizadeh, R., Golestani-Fard, F. and Scrivener, K. (2015) 'Pozzolanic activity of mechanochemically and thermally activated kaolins in cement', *Cement and Concrete Research*, 77, pp. 47–59.

Sperinck, S., Raiteri, P., Marks, N. and Wright, K. (2011) 'Dehydroxylation of kaolinite to metakaolin - A molecular dynamics study', *Journal of Materials Chemistry*, 21(7), pp. 2118–2125.

Statista (2024) *Bauxite reserves worldwide top countries 2023*. Available at: https://www.statista.com/statistics/271671/countries-with-largest-bauxite-reserves/.

Stevenson, C.M. and Gurnick, M. (2016) 'Structural collapse in kaolinite, montmorilonite and illite clay and its role in the ceramic rehydroxylation dating of low-fired earthenware', *Journal of Archaeological Science*, 69, pp. 54–63.

Suraj, G., Iyer, C.S.P. and Lalithambika, M. (1998) 'Adsorption of cadmium and copper by modified kaolinites', *Applied Clay Science*, 13(4), pp. 293–306.

Takbiri, M., Jozani, K.J., Rashidi, A.M. and Bozorgzadeh, H.R. (2013) 'Preparation of nanostructured activated alumina and hybrid alumina-silica by chemical precipitation for natural gas dehydration', *Microporous and Mesoporous Materials*, 182, pp. 117–121.

Tantawy, M.A. and Alomari, A.A. (2019) 'Extraction of Alumina from Nawan Kaolin by Acid Leaching', *Oriental Journal of Chemistry*, 35(3), pp. 1013–1021.

Tironi, A., Trezza, M.A., Scian, A.N. and Irassar, E.F. (2012) 'Kaolinitic calcined clays: Factors affecting its performance as pozzolans', *Construction and Building Materials*,

28(1), pp. 276–281.

Tironi, A., Trezza, M.A., Scian, A.N. and Irassar, E.F. (2014) 'Thermal analysis to assess pozzolanic activity of calcined kaolinitic clays', *Journal of Thermal Analysis and Calorimetry*, 117(2), pp. 547–556.

TRINDADE, M., DIAS, M., COROADO, J. and ROCHA, F. (2009) 'Mineralogical transformations of calcareous rich clays with firing: A comparative study between calcite and dolomite rich clays from Algarve, Portugal', *Applied Clay Science*, 42(3–4), pp. 345–355.

Udochukwu, M., Anyakwo, C.N., Onyemaobi, O.O. and Nwobodo, C.S. (2019a) 'Conditions for Thermal Activation of Ngwo Clay as an Alternative Resource for Alumina', *Natural Resources*, 10(01), pp. 1–15.

Udochukwu, M., Anyakwo, C.N., Onyemaobi, O.O. and Nwobodo, C.S. (2019b) 'Determination of the Calcination Procedure Required to Activate Edda Clay for Optimal Leaching of Alumina', *Journal of Minerals and Materials Characterization and Engineering*, 07(02), pp. 49–63.

Udochukwu, M., Anyakwo, C.N., Onyemaobi, O.O. and Nwobodo, C.S. (2019c) 'Effect of Calcination Condition on Thermal Activation of Ibere Clay and Dissolution of Alumina', *International Journal of Nonferrous Metallurgy*, 08(02), pp. 9–24.

Udochukwu, M., Anyakwo, C.N., Onyemaobi, O. and Nwobodo, C.S. (2019) 'The Thermal Activation of Nsu Clay for Enhanced Alumina Leaching Response', *International Journal of Engineering and Technologies*, 16, pp. 34–46.

Vaculíková, L., Plevová, E., Vallová, S. and Koutník, I. (2011) 'Characterization and differentiation of kaolinites from selected Czech deposits using infrared spectroscopy and differential thermal analysis', *Acta Geodynamica et Geomaterialia*, 8(1), pp. 59–67.

Varadwaj, G.B.B. and Parida, K.M. (2013) 'Montmorillonite supported metal nanoparticles: An update on syntheses and applications', *RSC Advances*, 3(33), pp. 13583–13593.

Wang, H., Cao, Z., Wang, J., Wang, Z., Chen, J. and Shen, L. (2023) 'Alkali Methods for Alumina Extraction from the By-products of High Alumina Coal: A Review', *Mining, Metallurgy and Exploration*, 40(5), pp. 1681–1694.

Wundermold (2014) *12 Uses of Aluminium Oxide Pt. 2*. Available at: https://www.wundermold.com/what-6-key-applications-aluminium-oxide/.

Xue, H., Dong, X., Fan, Y., Ma, X. and Yao, S. (2023) 'Study of Structural Transformation and Chemical Reactivity of Kaolinite-Based High Ash Slime during Calcination', *Minerals*, 13(4), p. 466.

Zirczy, G.N. (1972) *Kinetics of cordierite formation*.

Zunino, F., Boehm-Courjault, E. and Scrivener, K. (2020) 'The impact of calcite impurities in clays containing kaolinite on their reactivity in cement after calcination', *Materials and Structures/Materiaux et Constructions*, 53(2).

Appendices

Appendix A: MgO-Al2O3-SiO2 phase diagram

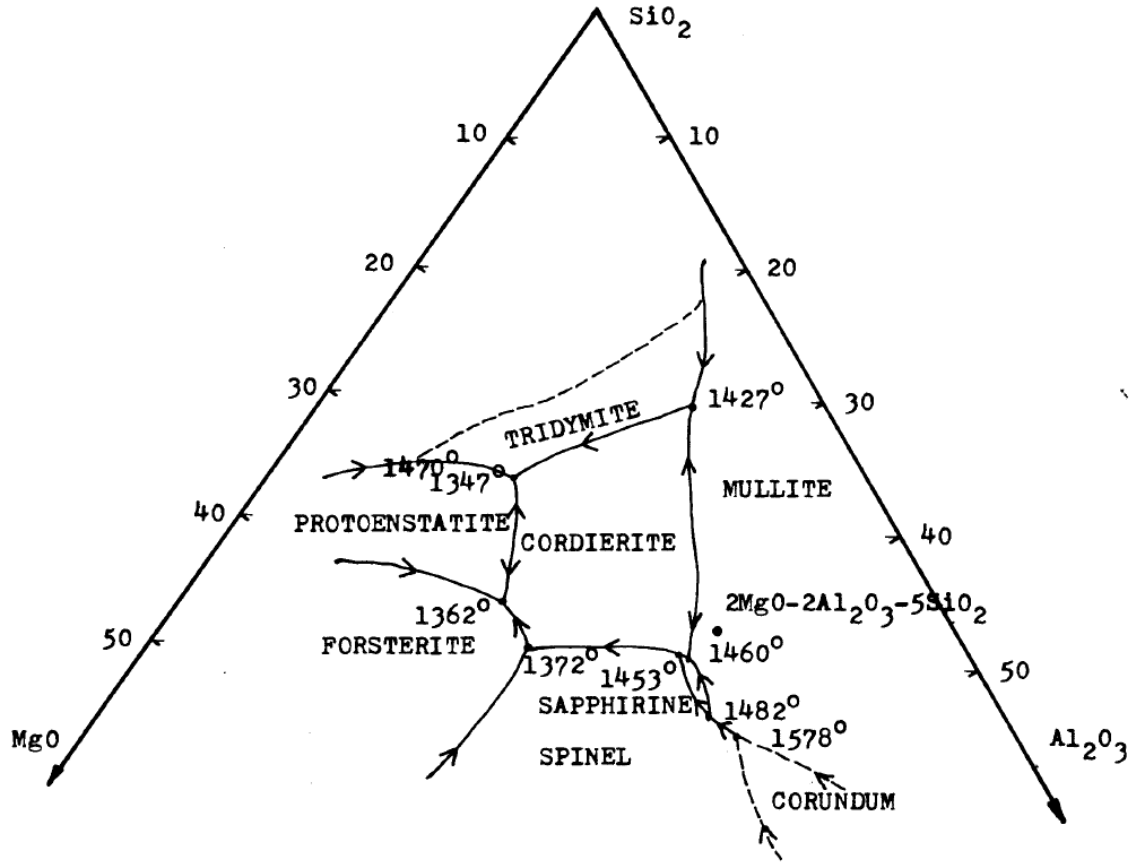

Figure A 1: MgO-Al2O3-SiO2 phase diagram (Zirczy, 1972)

Appendix B: Calculation example of extraction percentage

Al extraction calculation for BL clay calcined at 600 °C

Al Concentration of calcined BL clay (ICP-OES) = 20.24663 %

Al concentration in leachate (ICP-OES) = 18800 mg/l

About 10 g of calcined BL clay was leached in 100 ml HCl acid solution

Amount of Al in calcined BL clay = 0.2024663* 10 g

= 2.024663 g

Al concentration in leachate = 18800 mg/l * 0.1L

=1880 mg ≈1.88 g

Using Equation 5.1 for element extraction

$$Al\ (\%) = \frac{1.88g}{2.024663\ g} \times 100$$

Al (%) = 92.9

Appendix C: Chemical composition of calcined clays

Table C 1:Chemical composition of calcined BL clay

BL chemical composition (%)									
	Fe_2O_3	SiO_2	Al_2O_3	K_2O	CaO	MgO	TiO_2	Other	LOI
BL600	0.806	56.6	37.7	0.455	0.565	0.107	1.58	0.601	1.40
BL650	0.806	56.3	37.7	0.466	0.565	0.122	1.58	0.602	1.28
BL700	0.819	57.0	38.0	0.463	0.569	0.116	1.59	0.596	0.835
BL750	0.817	56.6	37.0	0.461	0.567	0.118	1.58	0.597	0.730
BL800	0.818	57.0	38.1	0.459	0.572	0.115	1.60	0.604	0.495

Table C 2: Chemical composition of calcined FL clay

FL chemical composition (%)									
	Fe_2O_3	SiO_2	Al_2O_3	K_2O	CaO	MgO	TiO_2	Other	LOI
FL600	0.619	53.3	41.9	0.536	0.075	0.014	1.37	0.297	1.54
FL650	0.602	53.5	42.1	0.538	0.073	0.021	1.37	0.307	1.49
FL700	0.617	53.9	42.3	0.529	0.074	0.01	1.38	0.303	0.866
FL750	0.633	53.9	42.3	0.537	0.071	0.019	1.39	0.313	0.692
FL800	0.612	53.9	42.4	0.542	0.072	<0.01	1.39	0.304	0.046

Table C 3: Chemical composition of calcined F clay

F chemical composition (%)									
	Fe_2O_3	SiO_2	Al_2O_3	K_2O	CaO	MgO	TiO_2	Other	LOI
F600	2.35	58.0	13.5	1.992	10.7	3.10	0.586	0.2	9.19
F650	2.37	58.8	13.7	2.013	10.8	3.10	0.597	0.2	8.07
F700	2.44	60.8	14.1	2.084	11.1	3.22	0.617	0.2	5.10
F750	2.52	62.6	14.6	2.149	11.5	3.30	0.636	0.2	2.30
F800	2.55	63.2	14.7	2.178	11.6	3.33	0.636	0.2	1.54